Defect Chemistry and Proton Conductivity in Ba-based Perovskites

Thesis by

Jian Wu

In Partial Fulfillment of the Requirements

for the Degree of

Doctor of Philosophy

California Institute of Technology

Pasadena, California

2005

(Defended Oct 27, 2004)

Acknowledgements

The five years I've spent at Caltech have given me source of the most precious experiences in my life. I believe that I must be blessed to be a member of such a great group and make so many friends here.

I would like to acknowledge a number of people who were accompanying me through the whole journey. First and foremost, I am eternally grateful to my family for their forever support and love. You are always who I can count on, and you will always be.

I am especially grateful to my advisor, Professor Sossina Haile, for her guidance, understanding and insight over the years. I learned a lot from her, not only in science, but also in life. I would like to thank Dr. Ma Chi and Dr. Carol Garland for their help on electron microscopes. I would also like to thank a number of collaborators for their contribution to this work, including Dr. Saiful Islam, Dr. R.A. Davies from University of Surrey for their work on the atomistic simulation, and Dr. Sean Brennan, Dr. Sam Webb for their help on EXAFS analysis.

I am indebted to the group members, Dane Boysen, Calum Chisholm, Tetsuya Uda, Zongping Shao, Liping Li, Peter Babilo, Lisa Cowan, Wei Lai and Martin Smith-Martinez, who fight with me over the equipments and make the research enjoyable. My friends outside the group, Hua Fang, Jiao Lin, Huirong Ai, Peng Xu and Greg Cash, thank you for sharing the great moments in my life.

This work was supported by the Department of Energy, Office of Basic Energy Sciences.

Abstract

The site incorporation mechanism of M^{3+} dopants into $A^{2+}B^{4+}O_3$ perovskites controls the overall defect chemistry and thus their transport properties. For charge balance reasons, incorporation onto the A^{2+} site would require the creation of negatively charged point defects, such as cation vacancies, whereas incorporation onto the B^{4+} site is accompanied by the generation of positively charged defects, typically oxygen vacancies. Oxygen vacancy content, in turn, is relevant to proton conducting oxides in which protons are introduced via the dissolution of hydroxyl ions at vacant oxygen sites.

This work proposes that, on the basis of X-ray powder diffraction studies, electron microscopy, chemical analysis, thermal gravimetric analysis, AC impedance spectroscopy, extended X-ray fine structure (EXAFS) and atomistic simulation, that nominally B-site doped barium cerate can exhibit dopant partitioning partially as a consequence of barium evaporation at elevated temperatures. Such partitioning and the presence of significant dopant concentrations on the A-site negatively impact proton conductivity. As a consequence of the greater ability of larger cations to exist on the Ba site, the H_2O adsorption and proton conductivities of large-cation doped barium cerates are lower than those of small-cation doped analogs.

A series of dopants, La, Nd, Sm, Gd and Yb are adopted in doped $BaCeO_3$ with the composition $BaCe_{0.85}M_{0.15}O_{3-\delta}$. Yb doped $BaCeO_3$ yields the highest proton conductivity among all the doped samples. Compositional non-stoichiometry, which is closely tied to sample processing, is studied in a $Ba_xCe_{0.85}M_{0.15}O_{3\pm\delta}$ series. It is indicated that low temperature synthesis is beneficial to reduce barium evaporation at elevated temperatures and in turn increase the proton conductivity. The chemical stability of $BaCeO_3$ is investigated and Zr is used to stabilize $BaCeO_3$ in CO_2-rich atmosphere effectively. This result helps to commercialize doped $BaCeO_3$ as the electrolyte material for SOFCs.

Contents

List of Figures

List of Tables

Chapter 1 Introduction

The broad objective of this work is to develop a firm understanding of the correlation between the defect chemistry and the properties of Ba-based perovskite, especially rare earth doped $BaCeO_3$, so as to allow the engineering of these compounds with the desired properties for the application in devices. This work is particularly focused on proton transport and application of $BaCeO_3$ in fuel cells, hydrogen permeable membranes and hydrogen sensors.

This introduction will provide a brief overview of Ba-based perovskite structure, the defect chemistry mechanism, proton incorporation and transfer mechanism and chemical stability.

1.1 Introduction to perovskite [1]

The mineral "perovskite" was discovered and named by Gustav Rose in 1839 from samples found in the Ural Mountains, named after a Russian mineralogist, Count Lev Aleksevich von Perovski. The original compound found was calcium titanium oxide ($CaTiO_3$). The name later was used to describe a general group of oxides possessing similar structures with a general formula of ABO_3. In some cases even non-oxides with similar structure are labeled perovskite. Compared to other oxide families such as pyrochlore, perovskite-related compounds can be synthesized with an extremely wide variety of combinations of chemical elements due to several reasons: (1) the perovskite structure accommodates both large (A-site) and small (B-site) cations; (2) distortions of the ideal cubic structure provide further flexibility for incorporating cations of different sizes; (3) the structure is remarkably tolerant of vacancy formation and atomic-scale

intergrowths with other structural motifs. In the ABO_3 perovskite structure A-site can be either M^+ (Na, K, etc.), M^{2+} (Ca, Sr, Ba, etc.), or M^{3+} (La, Fe, etc.) and the B-site can be occupied by M^{5+} (Nb, W, etc.), M^{4+} (Ce, Ti, etc.), or M^{3+} (Mn, Fe, etc.). The resulting materials can be insulators (as most perovskites have high electrical resistivity), semiconductors, superconductors and ionic conductors. Perovskites find technical application in ceramics, refractories, and electronics, as well as possible hosts for nuclear waste. Table 1-1 lists the properties and applications of some commonly investigated perovskites.

Table 1-1 Properties and applications of some perovskites

property	application	compound	reference
optical property	Electrooptical modulator, laser host, switch, second harmonic generator	(Pb, La)(Zr, Ti)O_3, $YAlO_3$, $LiNbO_3$, $KNbO_3$	[2,3,4,5,6,7]
ferroelctric/piozoelectric	Piezoelectric transducer, P.T.C. thermistor, electrostrictive actuator	$BaTiO_3$, $Pb(Zr,Ti)O_3$, $Pb(Mg,Nb)O_3$	[8,9]
Magnetic property	Magnetic bubble memory, ferromagnet	$GdFeO_3$, $LaMnO_3$	[10,11]
electrical property			
dielectric	Multilayer capacitor, dielectric resonator, thin film resistor	$BaTiO_3$, $BaZrO_3$	[12]
ionic conducting	Solid electrolyte	$(La,Sr)(Ga,Mg)O_{3-\delta}$	[13]
proton conducting	SOFC electrolyte, hydrogen sensor	$BaCeO_3$, $SrCeO_3$, $SrZrO_3$, $(La,Sr)MnO_{3-\delta}$	[14,15]
mixed conducting	SOFC electrode	$BaPrO_3$, $LaCoO_3$	[16,17,18]
Super conducting	superconductor	$Ba(Pb,Bi)O_3$	[19,20,21]
catalytic property	catalyst	$LaFeO_3$, $La(Ce,Co)O_3$	[22,23]

1.1.1 Ideal Cubic Structure

The ideal close-packed perovskite structure is shown in Fig. 1-1, with space group PM-3M. It consists of infinite three-dimensional, corner-sharing BO_6 octahedra with a

dodecahedrally coordinated A-site in the centre of a cavity generated by eight surrounding octahedra.

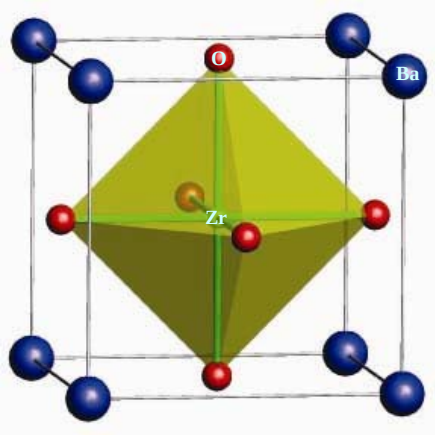

Fig 1-1 Schematic plot of ideally packed ABO_3 perovskite structure, with A=Ba, B=Zr

However, the ideal peroskite structure is rarely obtained at ambient temperature/pressure due to the strict constraints placed on the ionic sizes of A, B and O. The Goldschmidt tolerance factor, t, based on the geometrical packing of charge spheres was then introduced to describe the distortion of the perovskite structure from the ideal configuration.

1.1.2 Tolerance Factor

The Goldschmidt tolerance factor, t, based on the geometrical packing of charge spheres, is determined from ionic radii, r_A, r_B and r_O as following

$$t = \frac{(r_A + r_o)}{\sqrt{2}(r_B + r_o)} \qquad (1\text{-}1)$$

The ideally packed perovskite structure is simple cubic, as represented by $BaZrO_3$ with t = 1. However, a large number of perovskite structures are distorted to

orthorhombic, rhombohedral or tetragonal which can be approximated as cubic with t deviated from 1. In most cases, t varies between 0.75 and 1. Knight K.S.[24] proposed four distortion mechanisms in perovskite structures: (1) distortions of the BO_6 octahedra, (2) displacement of the B-site cation within the octahedron, (3) displacement of the A-site cation and (4) tilting of the octahedral relative to one another. The second and third mechanisms are characteristics of ferroelectric distortions in $BaTiO_3$. The fourth is typically observed when the A-cation is too small for the dodecahedral site, such as Ba in $BaCeO_3$.

The t factor of the same compound is reported to have different values depending on the author. This is due to different definition of the coordination number (CN) which yields different values of the ionic radii.

1.1.3 $BaCeO_3$ Structure

Cubic $BaCeO_3$ structure was first reported by Hoffmann A. in 1934[25]. In 1972 Jacobson *et al.* reported the orthorhombic phase of $BaCeO_3$[26], but not until 1980's had this material started to be investigated widely. Iwahara *et al.* first investigated protonic conductivity in doped $BaCeO_3$ and thereafter the corresponding application in solid oxide fuel cells (SOFCs)[14,27]. Subsequently, numerous studies have been carried out on the structure, transport property and chemical stability of doped $BaCeO_3$. It has become one of the promising electrolyte materials for proton conducting SOFCs.

The structure and phase transitions of $BaCeO_3$ have been investigated by conventional X-ray diffraction, neutron diffraction, infrared spectroscopy, Raman

spectroscopy etc. Table 1-2 lists phase transitions of $BaCeO_3$ from room temperature to high temperature based on the work of Knight *et al.*[24].

Table 1-2 Phase transitions of $BaCeO_3$ from 473 K to 1223 K

temperature (K)	**phase**	**space group**	**lattice parameter** a (Å)	b(Å)	c(Å)
473	orthorhombic	PMCN	8.79056(4)	6.25167(3)	6.22714(3)
573	orthorhombic	INCN	8.79532(4)	6.26224(3)	6.23342(3)
773	rhombohedral	F-32/N	8.84150(4)	α=90.156(1)°	
1223	cubic	PM-3M	4.44467(2)		

It has been proposed that the orthorhombic to orthorhombic and rhombohedral to cubic phase transitions are continuous while the orthorhombic to rhombohedral one is not. This sequence of phase transitions appears to be unique in $BaCeO_3$. The schematic structures are shown in Fig 1-2.

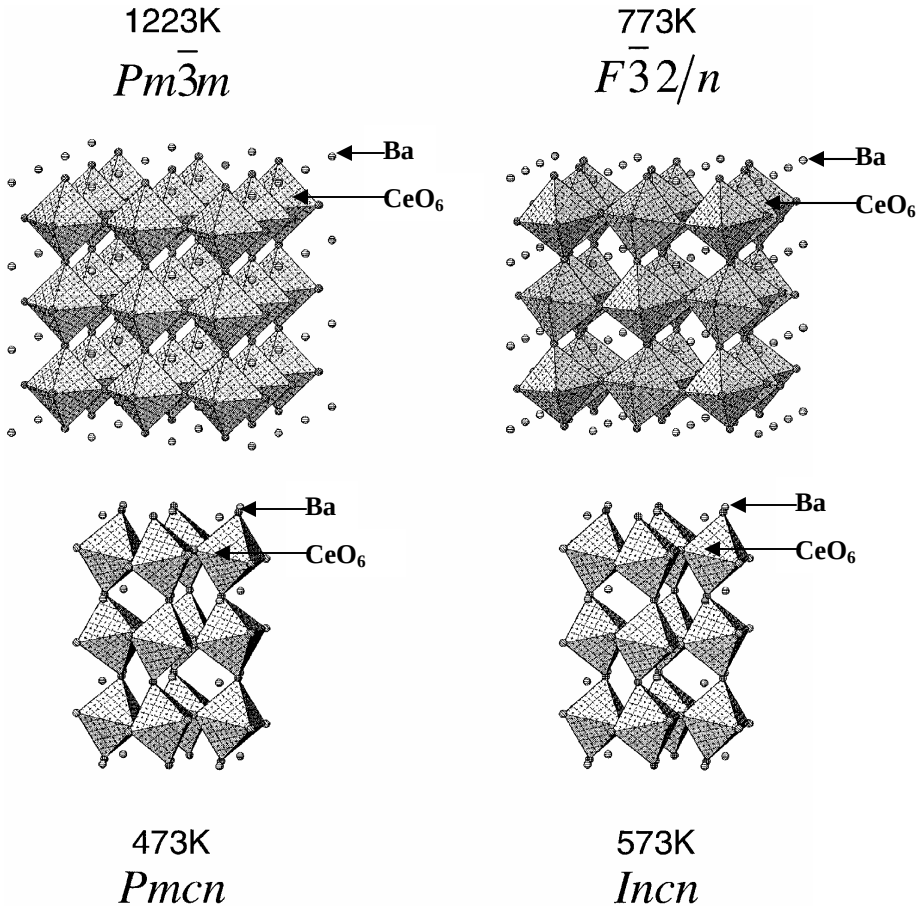

Fig. 1-2 Schematic plot of $BaCeO_3$ phase transition at different temperatures[24]

To date the published structural studies on $BaCeO_3$ show little evidence that doping introduces major perturbation to the parent structure. Therefore, the structural information is taken to be valid for doped $BaCeO_3$.

1.2 Proton Conductivity

Historically, the first conduction mechanism studied was electronic conductivity of metals and semiconductors. Subsequently, ionic conductors such as oxide ion, fluoride ion, silver, copper, lithium, sodium and potassium ion conductors were widely investigated and commercialized in industry. Compared with other ionic species, the

proton is unique due to its small size and the fact that it is a "naked" ion without an electron shell of its own. The proton resides within the electron shell of some anion with which it is associated. In the specific case of oxides, the oxygen ion radius is ~1.4 Å, whereas the O-H bond distance is only ~0.9 Å[28]. The extremely small size of protons makes it unlikely to jump from one crystallographic site to another all by itself. Meanwhile, the strong interaction between a proton and the electron cloud of the environment makes it rarely exists or transfers as a "bare" proton, instead, the motion is usually coupled with other phenomenon within a solid, such as molecular diffusion and phonons[29,30].

1.2.1 Defect Chemistry of Barium Cerate

Several publications have studied the defect chemistry and transport property of doped $BaCeO_3$, after Iwahara *et al.* first reported protonic conductivity in this material. It is well known that temperature and atmosphere greatly influence transport properties of most of the ionic conductors. However, under a certain temperature range and specific atmosphere, doped $BaCeO_3$ possesses significant protonic conductivity[14,31,32].

As investigated, the introduction of defects into the perovskite structure and their distribution in the structure are key factors that determine the protonic conductivity. Ideally, incorporation of trivalent dopants and subsequent incorporation of water/protons occur, respectively, as described in Kroger-Vink notation[33]

$$2Ce_{Ce}^{x} + O_o^{x} + M_2O_3 \rightarrow 2\,M'_{Ce} + V^{\bullet\bullet}_o + 2CeO_2 \qquad (1\text{-}2)$$

and

$$H_2O\ (gas) + V^{\bullet\bullet}_o + O_o^{x} \rightarrow 2OH_o^{\bullet} \qquad (1\text{-}3)$$

However, factors such as non-stoichiometry, atmosphere, dopant size, etc. complicate the defect reactions.

Firstly, the existence of Ba^{2+}-site substitution has been proposed by theoretical calculations for large dopants such as La and Sm[34]

$$2Ba_{Ba}^{x} + M_2O_3 + V^{\bullet\bullet}_{o} \rightarrow 2M^{\bullet}_{Ba} + O_o^{x} + 2BaO \quad (1\text{-}4)$$

This reaction consumes oxygen vacancy instead of creating new vacancies, thereafter lowers the protonic conductivity. Makovec *et al*.[35] proved the possibility of this reaction in the study of phase equilibrium in Nd_2O_3-$BaCeO_3$ system. Microanalysis of Nd-$BaCeO_3$ solid solutions indicated that the solutions could be represented by a general formula $Ba_{1-x}Nd_xCe_{1-y}Nd_yO_{3-(y-x)/2}(V^{\bullet\bullet}_{o})_{(y-x)/2}$ in which Nd is partitioned on both Ba and Ce site. The ratio between Nd incorporation at Ba-site and at Ce-site is a function of the starting composition, changing from 1 in the CeO_2-rich part of the BaO-CeO_2-Nd_2O_3 system, to ~0.1 in the BaO-rich part of the system. But to date very little research has been done to investigate the Ba^{2+}-site substitution with dopant other than Nd.

Secondly, non-stoichiometry is an inevitable problem closely tied with processing. Haile *et al.* [36] have proposed the possible defect reactions for non-stoichiometric cases. In materials containing excess Ba, three possible defect reactions can be considered to describe direct incorporation

$$BaO \rightarrow Ba^{\bullet\bullet}_{i} + O''_{i} \quad (1\text{-}5)$$

$$BaO \rightarrow Ba_{Ba} + O_O + V''''_{Ce} + 2\ V^{\bullet\bullet}_{o} \quad (1\text{-}6)$$

$$2BaO \rightarrow Ba_{Ba} + Ba''_{Ce} + 2\ O_O + V^{\bullet\bullet}_{o} \quad (1\text{-}7)$$

There are a number of consequences due to barium excess in undoped barium cerate, such as larger lattice constant, better sinterability and poorer stability in air, which can not be fully explained by the defect reaction proposed above.

As for materials with Ba deficiency, the possible defect reactions are

$$2Ba_{Ba}^{x} + M_2O_3 + V^{\bullet\bullet}_o \rightarrow 2M^{\bullet}_{Ba} + O_o^{x} + 2BaO \quad (1\text{-}4)$$

$$2Ba_{Ba} + 2O_O + M'_{Ce} + V^{\bullet\bullet}_o \rightarrow M^{\bullet}_{Ba} + 2BaO \quad (1\text{-}8)$$

$$2CeO_2 + M'_{Ce} + V^{\bullet\bullet}_o \rightarrow M^{\bullet}_{Ba} + 2Ce_{Ce} + 6O_O \quad (1\text{-}9)$$

In this case, a barium deficiency consumes oxygen vacancies, which is unfavorable for protonic conductivity. To date, the impact of barium deficiency on the properties of doped perovskites has not been examined systematically.

1.2.2 Proton Incorporation Mechanism

As mentioned above, when the doped perovskite oxide is exposed to water atmosphere the oxygen vacancies are replaced by hydroxyl groups by which means protons are incorporated into the perovskite structure. The defect chemistry reaction is described as

$$H_2O\ (gas) + V^{\bullet\bullet}_o + O_o^{x} \rightarrow 2OH_o^{\bullet} \quad (1\text{-}3)$$

The enthalpy of water incorporation (dissolution enthalpy), which determines the extent of protonation at a given temperature of a specific system is then calculated as

$$E_{H2O} = 2E_{OH} - E\ (V^{\bullet\bullet}_o) + E_{PT} \quad (1\text{-}3\text{-a})$$

Where E_{OH} is the energy associated with substitution of oxygen ion by the hydroxyl group, $E(V^{\bullet\bullet}_o)$ the energy of creating an oxygen vacancy, and E_{PT} the energy of the gas phase proton transfer reaction: $O^{2-} + H_2O \rightarrow 2OH^-$. Atomistic simulation

results illustrate negative dissolution enthalpy for $BaCeO_3$, $SrZrO_3$ and $CaZrO_3$, indicating dominating proton conductivity at low temperature in these materials, which is consistent with the experimental conclusions[28,34,37,38,39]. The dissolution enthalpy, E_{H2O}, varies with oxide systems and dopant levels. Atomistic simulation has indicated a change of E_{OH} with different dopant level and therefore suggested an energetic stabilization of the protonic defect with doping.

Whether or not there is any significant interaction between dopants and the incorporated proton is not clear yet. In spite of the debate held by Kreuer *et al*.[40] and Karmonic *et al.*[41], atomistic simulation predicts that the proton-dopant association may occur, which could be a major factor that limits the proton mobility at higher dopant levels.

1.2.3 Proton Transport Mechanism

The mechanism of proton transport has been categorized by different research groups with slight disagreement on the rules that are adopted to categorize, whereas the two principle mechanisms are well recognized despite the disagreement: the vehicle mechanism and the Grotthuss mechanism[31,32,42,43,44,45].

With the vehicle mechanism, the proton diffuses together with a "vehicle" such as H_3O^+. The rate which is relevant to the observed conductivity is the rate of vehicle diffusion Γ_D. This mechanism is mainly observed in compounds with loose bonded small molecules, especially acidic hydrates, such as Nafion®, HCl and $Sb_2O_3 \bullet nH_2O$. Fig. 1-3 (a) shows a schematic plot of how the vehicle mechamism works.

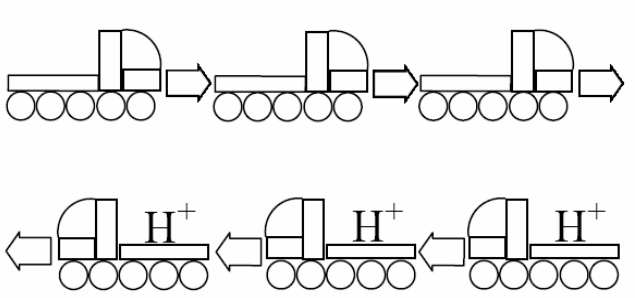

Fig. 1-3(a) Schematic diagram of vehicle mechanism for proton transfer[46]

With the Grotthuss mechanism, the proton diffuses through molecular orientation and proton displacement (sometimes it is called proton "hopping"). In this case, the relevant rates are the ones of proton transfer Γ_{trans} and the molecular reorientation $\Gamma_{reo.}$ The former is the limiting step for many proton conductors. This mechanism is observed in ice, solid acid salts (e.g., $CsHSO_4$) and perovskites (e.g., $BaCeO_3$, $BaZrO_3$) which are studied in detail in this work. A schematic plot is shown in Fig. 1-3 (b) here.

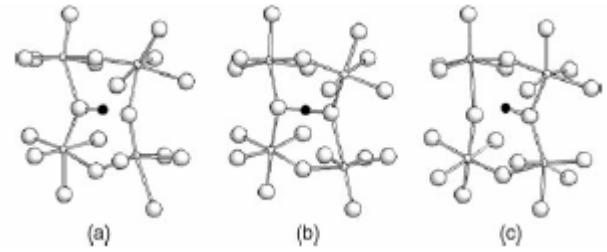

Fig. 1-3(b) Schematic diagram of Grotthuss mechanism for proton transfer in orthorhombic perovskite[28]

Quantum MD simulations reveal the details of Grotthuss mechanism in proton conducting perovksites[28,47]. The principal features of the proton transport process are rotational diffusion of the proton and proton transfer towards an adjacent oxygen ion. The rotational motion of the proton in the O-H group is rapid, which allows the reorientation of the proton towards the next oxygen ion before the transfer process. The transfer

process is then described by two states: the ground state in which the proton is bonded to a specific oxygen ion; and the barrier state in which the proton is equidistant between two adjacent oxygen ions, as shown in Fig. 1-4.

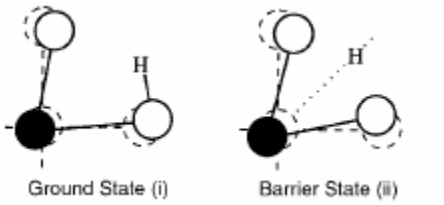

Fig. 1-4 Ground and barrier state configurations for proton transfer between adjacent oxygen ions. Solid lines represent relaxed lattice and dashed lines the perfect one[28]

The simulation results based on $LaAlO_3$, $BaZrO_3$, $BaCeO_3$, $CaZrO_3$ etc. indicate that the proton locally "softens" the lattice to allow the transient formation of hydrogen bonds and then the proton transfer between adjacent oxygen ions[34,37,39,48]. The energy difference between the ground state and the barrier state is less than 0.2 eV for most of the perovskites that are studied, which is much less than the observed activation energy of 0.4-0.7 eV for proton conductors. However, further investigation reveals the fact that the energy required for the adjacent oxygen ions to acquire an equivalent lattice environment to enter the barrier state is of the same magnitude of the activation energy. That is, there is an intermediate state between the ground and barrier states. This "relaxation" step makes the key contribution to the proton conductivity activation energy.

1.2.4 Isotope Effect[49,50,51,52,53]

In general, any physical property that depends directly or indirectly on the mass of the ions building up the lattice of a material may display an isotope effect: substituting an

element by one of its isotopes (e.g., $^{16}O<->^{18}O$) leads to a shift in the value of an observable. This shift is used to probe the physical property or kinetic process that are of interest.

Harold C. Urey discovered deuterium (heavy hydrogen) in 1931. Subsequently the isotope effect was developed as a tool to elucidate the hydrogen involved reaction mechanism. The isotope effect has become a major tool that confirms the protonic conductivity in solid oxide conductors. In this part a brief introduction to the isotope effect in proton conductors and the principal theories involved in understanding the effect is given.

Different theories have been developed to understand the mechanism of isotope effect, such as classical theory (ART), semi-classical theory, tunneling theory and escape theory.

The classical theory is adopted first to describe the isotope effect due to the influence of the pre-exponential term. As mentioned in section **1.2.3**, the proton (or deuteron) "hops" from one lattice site to another over a potential energy barrier, as a function of the configurational coordinate. For an ionic conductor, the conductivity has an Arrhenius form described by

$$\sigma = \frac{A}{T} e^{-\frac{E_a}{kT}} \tag{1-10}$$

where A is a pre-exponential term, T is the absolute temperature, k is Boltzman constant and E_a is the activation energy. More specifically, the pre-exponential term is described by

$$A \propto \Gamma_{trans} \propto \nu \propto \frac{1}{\sqrt{m}} \tag{1-11}$$

Where Γ_{trans} is the proton hopping rate, ν is an appropriate "attempt frequency" which, for a light atom, involves an effective mass that falls close to the mass of the hopping atom. In the case where ν is only the OH stretching frequency, a harmonic oscillator model is used, which yield the relationship $\nu \propto \frac{1}{\sqrt{m}}$ where m is the effective mass.

Therefore the conductivity will be written as

$$\sigma = \frac{A}{T} e^{-\frac{E_a}{kT}} \propto \frac{1}{\sqrt{m}} e^{\frac{-E_a}{kT}} \tag{1-12}$$

In the classical model, the activation energy is constant therefore the effective mass is the only parameter that affects the conductivity. The heavier mass of deuteron compared with hydrogen leads to a lower conductivity which contributes to the observable isotope effect.

However, the activation energy, E_a, has its contribution to the isotope effect. Semi-classical theory, which takes the zero-energy difference into consideration, is adopted here. In most cases, the activation energy is different for hydrogen and deuteron with $E_D > E_H$[54,55], as described in Fig. 1-5, which makes the difference in conductivity more observable.

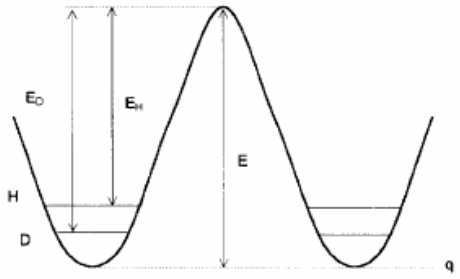

Fig. 1-5 Schematic plot of potential barrier of a proton/deuteron transfer reaction as a function of the configurational coordinate of the hopping atom[50]

If the proton is the dominating charge carrier, the isotope effect will be clearly observable, otherwise it can be concluded that the conductivity mechanism is not protonic.

1.2.5 Oxygen and Electronic Conductivity in $BaCeO_3$[56,57,58,59]

The transport property of perovskite oxides varies with dopant species, temperature and atmosphere. A brief discussion is presented in this section based on defect chemistry.

When trivalent dopants are incorporated into $BaCeO_3$ structure, oxygen vacancies are introduced

$$2Ce_{Ce}^{x} + O_o^{x} + M_2O_3 \rightarrow 2\,M'_{Ce} + V^{\bullet\bullet}{}_o + 2CeO_2 \qquad (1\text{-}2)$$

The oxygen vacancies thereafter react with oxygen to produce electron holes, in an oxygen rich atmosphere, or in a hydrogen/water rich atmosphere the oxygen vacancies react with hydrogen to produce protons

$$\frac{1}{2}O_2 + V_o^{\bullet\bullet} \xleftrightarrow{K_1} O_o^x + 2h^{\bullet} \qquad (1\text{-}13)$$

$$H_2O + V_O^{\bullet\bullet} + O_O^x \xleftrightarrow{K_2} 2OH_O^{\bullet} \qquad (1\text{-}3)$$

In this case, the effective charge carriers consist of oxygen vacancy, electron hole and proton, which lead to oxygen ion, electronic and protonic conductivity, respectively. Generally, the conductivity of mixed conductors is described as

$$\sigma_T = \sum \sigma_i = \sum q_i C_i B_i \qquad (1\text{-}14)$$

where σ_i is the conductivity component contributed by charge carrier species i, C_i is the concentration of the charge carrier, q_i is the charge and B_i is the mobility of charge carrier

species i. In most cases, the concentration C_i is the parameter that is modified by controlled atmosphere and chemical composition while the mobility B_i is usually a function of temperature only.

According to Eq. (1-13) and (1-3), the concentration of different charge carriers can be expressed as

$$p = K_1[V_O^{\bullet\bullet}]^{1/2} P_{O_2}^{1/4} \tag{1-15}$$

$$[H^{\bullet}] = K_2[V_O^{\bullet\bullet}]^{1/2} P_{H_2O}^{1/2} \tag{1-16}$$

where K_1 and K_2 are the equilibrium constants of Eq.(1-13) and (1-3), p, $[H^{\bullet}]$ and $[V_o^{\bullet\bullet}]$ are the concentration of electron holes, protons and oxygen vacancies, P_{O2} and P_{H2O} are the oxygen and water vapor partial pressures.

The generic electroneutrality condition is proposed for doped $BaCeO_3$ as

$$2[V_O^{\bullet\bullet}] + p + [H^{\bullet}] = [M_{Ce}^{'}] \tag{1-17}$$

where $[M_{Ce}^{'}]$ is the concentration of trivalent dopant on Ce-site.

Given specific oxygen, water partial pressure and determined dopant level, the concentration of a specific mobile species can be calculated from Eqs. (1-14) - (1-17). The calculation itself is complicated and will not be discussed here. Generally speaking, the electrical conductivity is not a major contribution to doped $BaCeO_3$, while high oxygen partial pressure enhances oxygen ion conductivity and high water partial pressure enhances the contribution of protonic conductivity.

The above discussion is based on the variation of the charge carrier concentration. As we mentioned in Eq.(1-14), temperature is essential to the mobility of mobile species, which influence the conductivity as well. In most cases, electron/hole requires the lowest activation energy while oxygen ion the highest. Electronic conductivity in doped $BaCeO_3$

is very small and usually can be ignored as protonic conductivity is significant at medium temperature (400-600°C). Oxygen ion conductivity becomes dominating at higher temperature when the electrolyte starts to lose incorporated protons.

1.3 Chemical Stability

In spite of the high proton conductivity, doped $BaCeO_3$ has not been commercialized to date due to its poor chemical stability under SOFC operation condition, that is, the CO_2-rich atmosphere[60,61].

The reaction of an ABO_3 perovskite with CO_2 is written as

$$ABO_3 + CO_2 \rightarrow ACO_3 + BO_2 \quad (1\text{-}18)$$

This reaction can be broke into two reactions

$$ABO_3 \rightarrow AO + BO_2 \quad (1\text{-}19)$$

$$AO + CO_2 \rightarrow ACO_3 \quad (1\text{-}20)$$

As for Ba-based perovskite, such as $BaCeO_3$, $BaZrO_3$, $BaTiO_3$, $BaPrO_3$, reaction (1-20) remains the same, therefore reaction (1-19) can be used to evaluate the thermodynamic stability of Ba-based perovskites under SOFC operation condition. Reaction (1-19) is rewritten as

$$AO + BO_2 \rightarrow ABO_3 \quad (1\text{-}19\text{-a})$$

to better describe the formation of a perovskite. The enthalpy of formation from the oxides can be calculated from the heats of solution which are determined experimentally by several groups. Navrotsky *et al*.[62] have shown that the heat of formation from oxides of perovskite compound vary in a nearly linear relation with the value of the Goldschmidt tolerance factor t. Fig 1-6 illustrates this relationship with Ba-based perovskite.

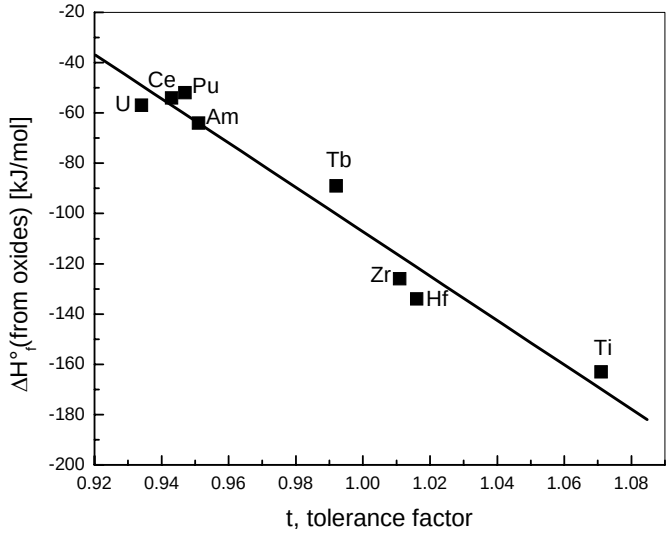

Fig. 1-6 Tolerance factor vs. formation enthalpy of Ba-based perovskite compounds, with B-site cation listed on the plot.

From Fig. 1-7 it is evident that $BaCeO_3$ exhibits relatively higher formation heat (~60-100KJ/mol), compared with $BaTiO_3$ and $BaZrO_3$. As a potential electrolyte material for SOFC, the chemical stability, especially the stability in a CO_2-rich atmosphere under medium high temperature becomes a major concern. Scholten MJ *et al*.[61] calculated that $BaCeO_3$ react with pure CO_2 below 1185°C, therefore to maintain stable behavior of a SOFC, the operating temperature should be high enough and the partial pressure of CO_2 low enough to avoid the decomposition of the cerate. Various approaches have been investigated to improve its chemical stability while not sacrificing too much of the protonic conductivity. This will be discussed in detail in the following chapters.

1.4 Problem Statement

In summary the problems and the approaches we are focusing on in the present work are:

1. Site incorporation selectivity and defect chemistry in doped barium cerate:

The experimental investigation is extended to a series of dopant species including La, Nd, Sm, Gd and Yb. Both indirect (XRD, Microprobe, Thermal analysis) and direct methods (EXAFS) are utilized to comprehensively study the question of site incorporation selectivity.

2. The relationship between compositional non-stoichiometry and site incorporation selectivity in barium cerate.

The influence of different synthesis routes, especially the evaporation of Ba at high temperature on the compositional non-stoichiometry is systematically studied by both experimental and atomistic simulation method.

3. The impact of dopant site incorporation selectivity and compositional non-stoichiometry on conductivity of barium cerate.

The relationship between defect chemistry and site incorporation selectivity is studied and thereafter the impact of site partition and non-stoichiometry on proton conductivity is revealed.

4. Improved chemical stability of barium cerate by introducing zirconium into the structure.

The chemical stability of the solid solution $Ba(Ce,Zr)O_3$ is investigated in CO_2-rich atmosphere, anticipating that Zr can stabilize barium cerate in CO2 with limited sacrifice on proton conductivity.

Chapter 2 Experimental Techniques

2.1 Introduction

In this chapter the synthesis and experimental techniques used throughout this research is discussed in detail. The discussion of the EXAFS method, also used in this thesis, is postponed until Chapter 4, a chapter that deals entirely with that method.

2.2 Synthesis

2.2.1 Solid State Reaction (SSR)

Materials examined in this work were synthesized by both solid state reaction (SSR) and chemical solution methods (MP). The latter were prepared in order to establish whether or not chemical homogeneity had a significant impact on the defect chemistry of the materials.

For example, the SSR route for $BaCe_{0.85}M_{0.15}O_{3-\delta}$ is as follows. Starting materials (from Alfa Aesar) of $BaCO_3$ (99.95%), CeO_2 (99.9%), M_2O_3 (99.9%) (M = La, Nd, Sm, Gd, Yb) were ball milled in acetone for 48 h and subsequently calcined in stagnant air at 1300˚C for 6 h. The calcined samples were lightly ground and a second calcination step was carried out at 1300˚C for another 6 h to ensure that a single perovskite phase was formed.

The nominal formation reaction is (e.g., $BaCe_{0.85}M_{0.15}O_{3-\delta}$)

$$BaCO_3 + (0.85)CeO_2 + (0.075)M_2O_3 \rightarrow BaCe_{0.85}M_{0.15}O_{3-\delta} + CO_2\uparrow \qquad (2\text{-}1)$$

As for the other compositions, the synthesis follows the same route, with different starting materials and variable molar ratio, respectively.

2.2.2 Modified Pechini Process (MP)

Pechini process is a chemical solution method named after its inventor, Maggio Pechini. It has been proved to be an effective method for synthesis of multicomponent oxide materials. Usually an aqueous solution of suitable oxides or salts is mixed with an alpha-hydroxycarboxylic acid such as citric acid and EG is added into the solution. At heating an esterification process runs in the system leading to formation of a stable gel in which the metal ions remain fixed. In modified Pechini process, ethylene diamine tetraacetic acid (EDTA) has been used to replace citric acid due to its strong chelating power. Schematically the esterification reaction is described as

$$R'OH + HO\text{-}\overset{\overset{O}{\|}}{C}\text{-}R \rightarrow R'\text{-}O\text{-}\overset{\overset{O}{\|}}{C}\text{-}R + H_2O$$

The homogeneity of the gel ensures at its subsequent burning crystallization of stoichiometric final product at relatively mild conditions.

In this study, the chemical solution synthesis of $Ba_xCe_{0.85}M_{0.15}O_3$ (M = Nd, Gd, Yb, x = 0.95-1.05) followed the modified Pechini (MP) process of Aragwal and Liu[63]. The precursors $Ba(NO_3)_2$, $Ce(NO_3)_3 \bullet 6H_2O$, $Nd(NO_3)_3 \bullet 6H_2O$, $Yb(NO_3)_3 \bullet 4.44H_2O$ and $Gd(NO_3)_3 \bullet 5.45H_2O$ (the water content in the Yb and Gd nitrates was determined by thermogravimetric analysis) were dissolved in water along with ethylenediaminetetraacetic acid (EDTA) and ethylene glycol (EG), which served as polymerization/complexation agents. The molar ratios EDTA/ΣMetal and EDTA/EG were fixed at 2 and 1/3, respectively. Evaporation of water and polymerization of the ethylene glycol occurred upon mild heating, and the resulting char was calcined at 1300°C for 10 h.

2.2.3 Pellet Fabrication

Green pellets (9 mm in diameter) were obtained by uniaxial pressing at 150 MPa and isostatic pressing at 270 MPa. High density pellets (≥ 94 % of theoretical) were obtained by sintering in stagnant air at 1550˚C for 4 h. Density was determined by simple measurements of pellet mass and dimensions after polishing the surfaces.

One set of sintered pellets, all of composition $BaCe_{0.85}Gd_{0.15}O_{3-\delta}$, were obtained by pressing the chemically synthesized powders using poly(vinyl alcohol) as a binder and then sintering at 1500, 1550, 1600, or 1650°C for 4 h. These samples were prepared in order to explicitly examine the influence of high temperature processing on defect chemistry (Chapter 3).

2.3 Common Characterization Methods

2.3.1 Powder X-ray Diffraction (PXRD)

Powder X-ray diffraction is an essential technique for phase identification and crystal structure refinement. PXRD data obtained in this work were collected in reflection mode at room temperature and under ambient conditions with a Siemens D-500 powder diffractometer using CuKα radiation (λ = 1.5418 Å) and an applied voltage and current of 45 kV and 40 mA, respectively. Both phase identification and lattice parameter refinement were performed. When applicable, Nickel powder (99.99%) served as an internal standard for peak position determination. For all samples, measurements were performed soon after synthesis in order to minimize any influence of water uptake. The lattice parameters were refined using the Rietica Rietveld program[64]. Use of a Rietveld program ensures that peak indexing was accurate, however, no attempt was made to

implement complete analysis of structural parameters (in particular, site occupancies) because of the similarity of the scattering lengths of the cations involved and the limited range (20-90° 2Θ) over which data could be collected.

2.3.2 Thermal Analysis

The behavior of compounds as a function of temperature was probed by thermal gravimetric analysis (TGA) and differential temperature analysis (DTA), in conjunction with off-gas mass spectroscopy. Thermal analysis was utilized for the characterization of proton incorporation, reaction with CO_2 and decomposition behavior of doped $BaCeO_3$ and $BaZrO_3$.

For the detection of proton incorporation, thermal gravimetric analysis (TGA, Netzsch STA 449) of H_2O saturated sintered pellets (saturated at 500˚C for 20 h, in flowing water-saturated argon atmosphere) was performed in flowing dry Ar at a heating rate of 20˚C/min over the temperature range from 100 to 1000˚C to assess H_2O incorporation ability. The exhaust gases released during the heating process were examined by mass spectroscopy (ThermoStar^{TM}).

For the determination of chemical stability, thermal gravimetric analysis (Perkin-Elmer TGA-7) and differential thermal analysis (Perkin-Elmer DTA-7) were utilized. The samples were examined in flowing CO_2 (flow rate 25±1 ml/min) at a heating rate of 20°C/min with a temperature range from 400° to 1440°C.

2.3.3 Scanning Electron Microscope and Energy Dispersive Spectroscopy

Scanning electron microscopy in conjunction with EDS was used to examine microstructural and chemical features of sintered samples. With its high spatial resolution, EDS was utilized to determine compositional differences between bulk and grain boundary regions of selected sintered pellets. Analysis was performed using a LEO 1550VP Field Emission SEM and INCA Energy 300 X-ray Energy Dispersive Spectrometer system. Samples for EDS analysis were mounted in an epoxy resin, cut, polished and coated with a conductive layer of carbon. Prior to carbon coating, samples were etched with concentrated HF for several minutes to reveal grain boundaries. The Oxford INCA EDS software employs the PAP (Pouchou and Pichoir) model for quantitative analysis[65] in which fundamental factors are used to correct for the effects of atomic number, absorption, and fluorescence to the measured intensity of the elements

2.3.4 Electron Microprobe Analysis

Electron microprobe analysis was used primarily for quantitative measurements of the average chemical compositions of sintered pellets. The data were collected using a JEOL JXA-733 microprobe with an applied voltage and current of 15 kV and 25 nA, respectively. All samples for this analysis were mounted in an epoxy resin, cut, polished and coated with a conductive layer of carbon. Characteristic X-ray emission intensities of the specific elements, as measured in the microprobe, were converted to chemical weight percents and molar ratios with the program CITZAF[66]. The Lβ1 line of Ce was collected to avoid interference with the Lβ emission of Ba. The compounds $CePO_4$, $GdPO_4$,

$NdPO_4$, $YbPO_4$ and $BaTiSi_3O_9$ served as standards for quantification of the X-ray intensities.

2.3.5 Fourier Transform Infrared Spectroscopy

FTIR and far-IR spectroscopy were performed on a Nicolet Magna 860 FTIR spectrometer in flowing nitrogen, in order to detect incorporated O-H group or the influence on the crystalline structure by the introduction of different dopants. Calcined powder samples were diluted in optically transparent KBr and pressed into pellets (sample: KBr mass ratio of 1:300). Various beam splitters and detectors were used to optimally cover the range from 4000 cm^{-1} to 100 cm^{-1}, from the far infrared to mid infrared range.

2.3.6 BET Surface Area Measurement

Powder surface area analysis was carried out by a nitrogen adsorption method using a Gemini 2360 surface area analyzer. Prior to measurement powder samples were degassed at 80°C in N_2 overnight.

Different methods can be applied to analyze the collected data to develop specific information, the multipoint Brunauer, Emmett and Teller (BET) method is used in this study to provide total surface area of the powder samples[67]. The BET equation is

$$\frac{1}{W[(P_0/P)-1} = \frac{1}{W_m C} + \frac{(C-1)}{W_m C}\frac{P}{P_0} \qquad (2\text{-}2)$$

where W is the weight of nitrogen adsorbed at a give relative pressure P/P_0 (p_0 is the vapor pressure of the pure condensed adsorbate), W_m the weight of gas to give monolayer coverage and C is a constant that is related to the heat of adsorption. Usually when P/P_0 is

between 0.05-0.30, there is a linear relationship between $1/W[(P_o/P)-1]$ and P/P_0. The slope and intercept of the plot $1/W[(P_o/P)-1]$ vs. P/P_0 are used to determine the quantity of nitrogen adsorbed in the monolayer and therefore calculate the surface area.

2.4 A.C. Impedance Spectroscopy[68,69,70]

The transport properties of sintered pellets were examined by AC impedance spectroscopy over a frequency range from 20 Hz to 1M Hz on an HP 4284 LCR (inductance-capacitance-resistance) meter. Platinum electrodes were sputter coated onto the opposing sides of polished pellets. Samples were equilibrated in water saturated Ar at 400°C for 2 h. The data were collected upon cooling at a rate of 0.5°C/min. The amplitude of the voltage was 1 V.

Alternating current (AC) impedance spectroscopy is widely used in studying the conductivity of ionic conductors. There are several advantages of using this technique: 1) The measurement can be implemented using arbitrary electrodes; 2) The resistance of grain boundaries and that of the grain interiors can be separated in many cases.

There are several models for an electrolyte under an applied voltage. The simplest one is a resistor and a constant phase element (which is simplified to be a capacitor here) in parallel, as shown in Fig 2-1 (a).

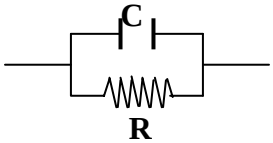

Fig. 2-1 (a) Circuit model of a resistor and a capacitor in parallel

For such a circuit, the response to an applied voltage,

$$V(t) = V_o e^{i\omega t} \tag{2-3}$$

will be a current in the resistor,

$$I_R = \frac{V_o e^{i\omega t}}{R} = \frac{V(t)}{R} \tag{2-4}$$

and a current in the capacitor

$$I_C = \frac{dQ(t)}{dt} = \frac{d(CV(t))}{dt} = C\left(\frac{dV_o e^{i\omega t}}{dt}\right) = i\omega CV_o e^{i\omega t} = i\omega CV(t) \tag{2-5}$$

The total current in the circuit is then

$$I_{total} = I_R + I_C = \frac{V(t)}{R} + i\omega CV(t) \tag{2-6}$$

Exactly like the conventional impedance, Z, the complex impedance is defined as the ratio between the voltage and current, which is here

$$Z = \frac{V(t)}{\frac{V(t)}{R} + i\omega CV(t)} = \frac{1}{\frac{1}{R} + i\omega C} \tag{2-7}$$

The impedance can be separated into its real, Z′, and imaginary, Z″, parts to give

$$Z = \frac{\frac{1}{R}}{\left(\frac{1}{R}\right)^2 + (\omega C)^2} - i\frac{\omega C}{\left(\frac{1}{R}\right)^2 + (\omega C)^2} = Z' - iZ'' \tag{2-8}$$

A plot of Z′ vs. -Z″ (as parametric functions of ω) will result in a semicircle of radius R/2 in the first quadrant, Fig 2-1 (b). The time constant of this simple circuit is defined as

$$\tau_o = RC = \frac{1}{\omega_o} \tag{2-9}$$

and corresponds to the characteristic relaxation time of the sample. Substituting ω_o from Eq. (2-9) into Eq. (2-8) gives Z′ = R/2, Z″ = R/2, so that the characteristic frequency lies at the peak of the semi-circle. A plot of Z′ vs. -Z″ is often called a Nyquist plot.

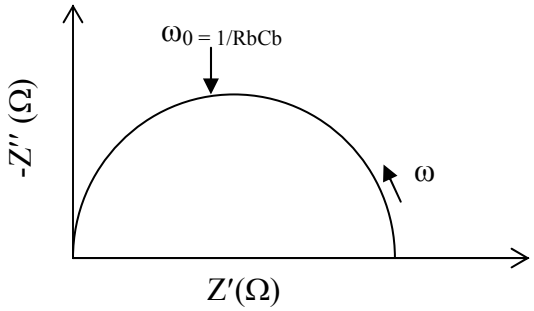

Fig. 2-1 (b) A Nyquist plot for a circuit of a resistor and a capacitor in parallel

In an ideal polycrystalline sample, the Nyquist plot exhibits an arc at high frequency, a second arc at lower frequencies, and a linear portion at the lowest frequencies, as shown in Fig 2-2 (a). The corresponding circuit model is shown in Fig 2-2(b). Two parallel RC circuits and a constant phase element are lumped together. The first circuit is assigned to represent the grain interior behavior, the second one the grain boundary behavior, while the third one is the electrode behavior.

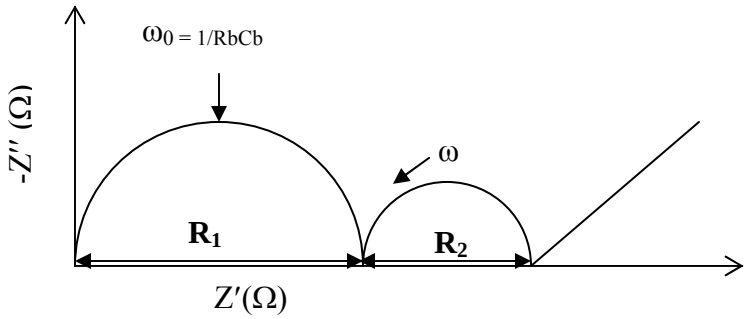

Fig. 2-2 (a) A typical Nyquist plot for a polycrystalline material. The real and imaginary components of impedance are plotted as parametric functions of frequency.

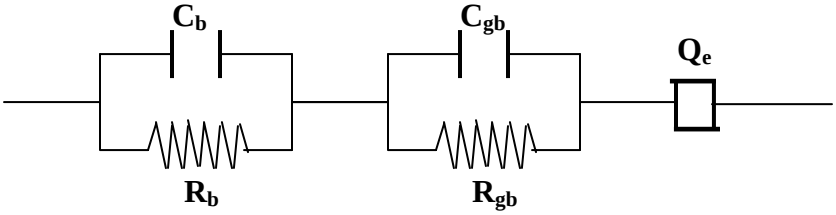

Fig. 2-2 (b) Equivalent circuit model of a polycrystalline material in which components in parallel have been lumped together

The measurement of the bulk conductivity is straightforward from the Nyquist plot, while the measurement of specific grain boundary conductivity requires knowledge of the grain size and grain boundary thickness. In order to determine the grain boundary conductivity without detailed micro-structural and electrical information, a "brick layer model" is adopted, as shown in Fig 2-3,

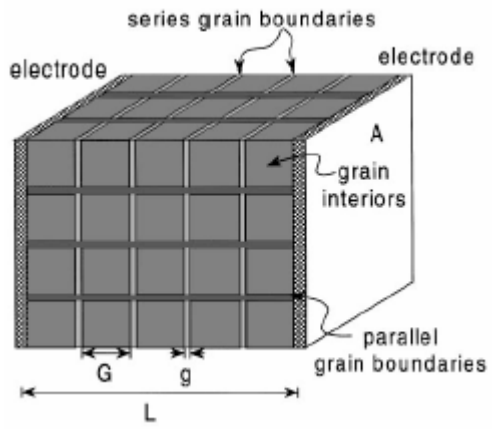

Fig. 2-3 "Brick Layer" model of a polycrystalline material. Grains are assumed to be cube-shaped, and grain boundaries to exist as flat layers between grains[70]

where L is the sample length, A is the sample cross sectional area, G is the edge length of the grains and g is the grain boundary thickness. The implication of the "brick layer model" and its application was discussed in detail in ref[70]. Here we list the conclusions that will be used in this study.

Define σ_{bulk} and σ_{gb} as the specific conductivity of the bulk and grain boundary, respectively. For the situation where $\sigma_{bulk} > \sigma_{gb}$ and $g << G$, the bulk conductivity is described as

$$\sigma_{bulk} = \frac{L}{A}\frac{1}{R_1} \tag{2-10}$$

while σ_{gb} can be obtained in terms of the ratio R_1 to R_2 and g/G

$$\sigma_{gb} = (\frac{g}{G})\frac{R_1}{R_2}\sigma_{bulk} \tag{2-11}$$

The parameter g/G is available from the dielectric constant of the bulk and grain boundary

$$\frac{g}{G} = \frac{C_1}{C_2} \tag{2-12}$$

where $C = 1/R\omega_0$, as described in Fig 2-2 (a). The grain boundary conductivity derived by this means is called “specific grain boundary conductivity.”

Chapter 3 Defect Chemistry of Barium Cerate by Indirect Methods

3.1 Introduction

In this chapter indirect methods, including powder X-ray diffraction, lattice parameter refinement and chemical analysis by electron microprobe are adopted to investigate the defect chemistry of doped non-stoichiometric barium cerate (dopant M = La, Nd, Sm, Gd, Yb). The dopant Nd, Gd and Yb are taken to be representative of the entire series and are examined in greater depth than the other two dopants.

It is shown that dopants intended for incorporation onto the B-site of ABO_3 perovskites can, in fact, be partitioned over both the A and B-sites. Two quantities are determined: (1) the solubility limit of the dopant onto the A-site, a thermodynamic quantity, and (2) the true stoichiometry of nominally $BaCe_{0.85}M_{0.15}O_{3-\delta}$ composition exposed to typical processing conditions, a kinetic quantity.

3.2 Single Phase Limit by XRD

The XRD powder diffraction patterns of the calcined $Ba_xCe_{0.85}M_{0.15}O_{3\pm\delta}$ (SSR, x = 0.85, 0.90, 0.95, 1.0, twice calcined) are shown in Fig 3-1. For La, Nd, Sm and Gd doped sample, single phase perovskite is obtained when the material is nominally stoichiometric. For Gd-doped samples, very small peaks due to fluorite phase with the composition of $(Ce,Gd)O_{2-\delta}$ are present when x = 0.95, for La and Nd doped samples the fluorite phase is present only for highly Ba deficient samples with x = 0.85 while for Sm-doped samples the fluorite phase is present when x = 0.90. For Yb doped samples, the fluorite phase is observed even in the nominally stoichiometric composition. Samples

synthesized by the MP route exhibited similar XRD patterns, which are not shown here. The only difference between the SSR and MP samples is that the nominally stoichiometric Yb doped $BaCeO_3$ exhibited a single perovskite phase, which is probably due to the different processing method, particularly, different calcination temperature. This is discussed in detail in the following sections.

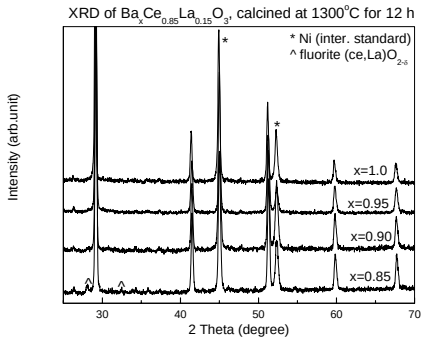

(a)

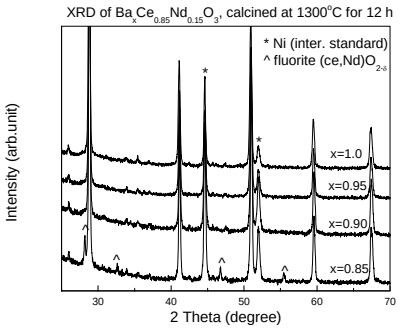

(b)

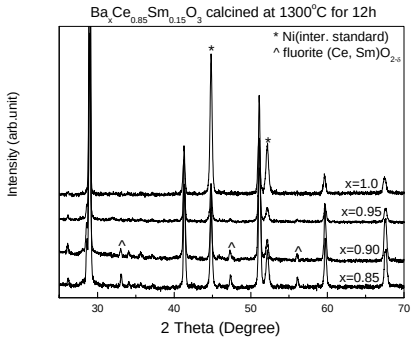

(c)

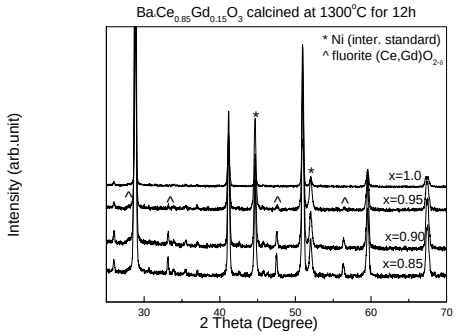

(d)

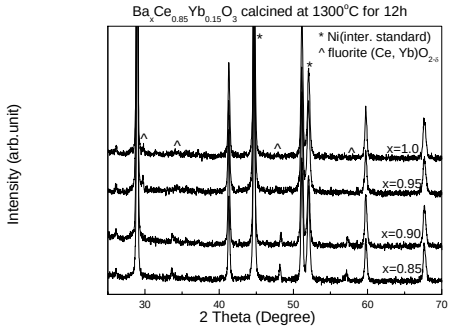

(e)

Fig. 3-1 XRD pattern for $Ba_xCe_{0.85}M_{0.15}O_{3-\delta}$ (x=0.85-1.0), samples: (a) La; (b) Nd; (c) Sm; (d) Gd; (e) Yb, synthesized by solid state reaction route, calcined at 1300°C/12 h.

To accurately determine the maximum Ba deficiency limit up to which the $(Ce,M)O_{2-\delta}$ fluorite phase precipitate was detected, additional Ba deficient samples were prepared with Nd and Gd dopants, with the composition of $Ba_xCe_{0.85}Nd_{0.15}O_3$ (SSR, x = 0.86, 0.87, 0.88) and $Ba_xCe_{0.85}Gd_{0.15}O_3$ (SSR, x = 0.96, 0.97). The corresponding XRD powder diffraction patterns are shown in Fig. 3-2. For Nd doped samples, the small peaks due to fluorite phase was visible when x = 0.88 and disappeared as x increased to 0.90. For Gd doped samples, very weak fluorite phase peaks was detectable when x = 0.95 while x = 0.96 showed a pure perovskite phase. Therefore the maximum Ba deficiency for Nd and Gd are x = 0.90 and 0.96, respectively.

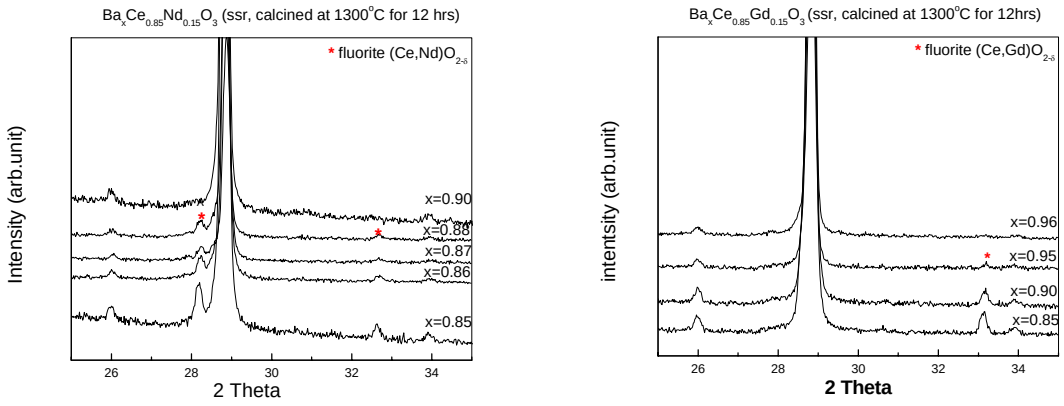

(a) (b)

Fig. 3-2 (a) XRD pattern for $Ba_xCe_{0.85}Nd_{0.15}O_{3-\delta}$ (x=0.85, 0.86, 0.87, 0.88, 0.90) synthesized by solid state reaction route, calcined at 1300°C/12 h.

Fig. 3-2 (b) XRD pattern for $Ba_xCe_{0.85}Gd_{0.15}O_{3-\delta}$ (x=0.85, 0.90, 0.95, 0.96) synthesized by solid state reaction route, calcined at 1300°C/12 h.

3.3 Cell Volume Variations

The cell volume as a function of Ba concentration, x, is presented in Fig 3-3, for both SSR and MP prepared samples, over a wide range of values of x. For compositions synthesized by the same route, there is a general trend in unit cell volume of La > Gd > Sm > Nd > Yb. In addition, there is a variation in cell volume as a function of Ba content, discussed later in this chapter. Sintered samples (data not shown for clarity) revealed a similar trend.

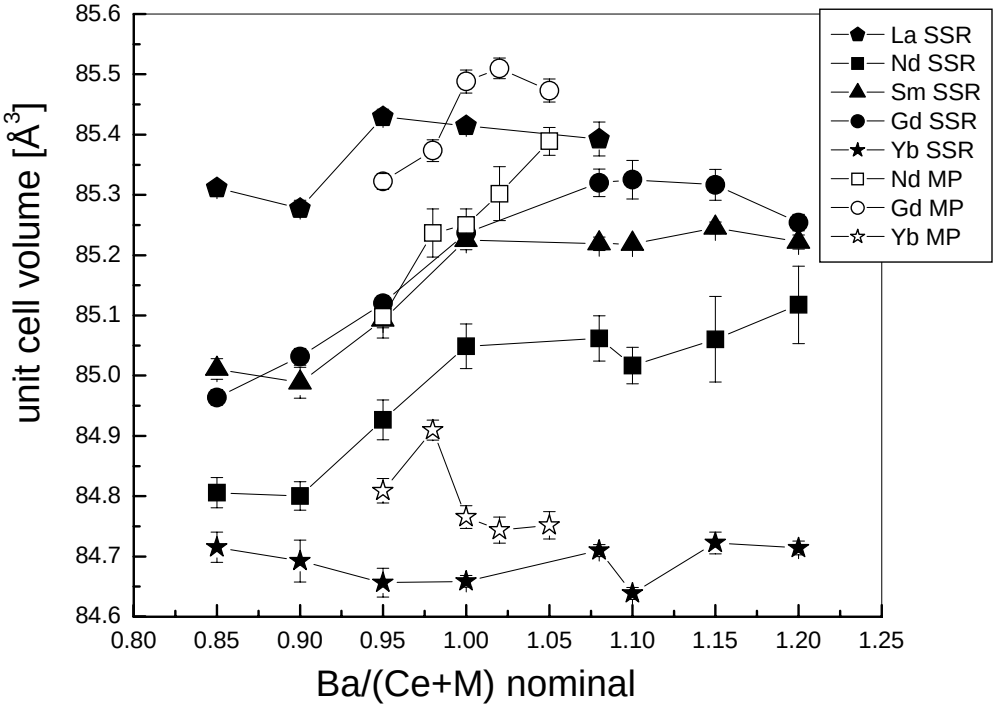

Fig. 3-3 Dependence of cell volume vs. Ba concentration in $Ba_xCe_{0.85}M_{0.15}O_3$ (x = 0.85-1.20, M = La, Nd, Sm, Gd, Yb)

The cell volume of the nominally stoichiometric samples vs. dopant radius is shown in Fig 3-4. From a simple consideration of ionic radii, one would expect the La-doped sample to have the greatest cell volume and Yb-doped the smallest, with the Nd, Sm and Gd-doped samples following a decreasing trend, respectively. However, it is evident that there is an abnormal cell volume drop on Nd-doped $BaCeO_3$, which leaves the Gd-doped sample a larger cell volume than the Nd-doped and the Sm-doped.

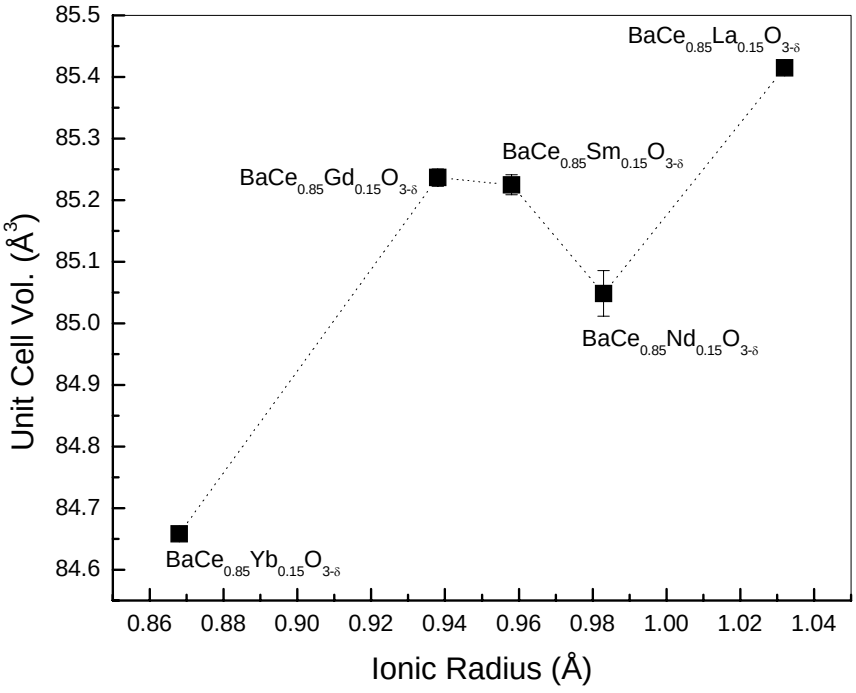

Fig. 3-4 Cell volume of nominal stoichiometric $BaCe_{0.85}M_{0.15}O_{3-\delta}$ (SSR, M = La, Nd, Sm, Gd, Yb) vs. dopant radius

The unexpected cell volume reversion between Gd-doped and Nd-doped samples, as well as the extremely close cell volume between Gd-doped and Sm-doped samples, is proposed to be a result of dopant incorporation onto the Ba^{2+}-site, as discussed below.

If one assumes that the trivalent dopant ion is incorporated only onto the cerium site, $BaCe_{0.85}M_{0.15}O_{3-\delta}$, the perovskite cell volume should be a monotonic function of dopant ionic radius, as listed in Table 3-1[71]. If, however, as proposed here, large ions such as La and Nd are at least partly incorporated onto the Ba site, the substitution of the large Ba ion by the smaller M^{3+} ion would be anticipated to yield a cell volume that is smaller than otherwise expected. In comparison to Gd and Yb, the large size of La and

Nd makes them more amenable to incorporation onto the A site and thus the effect will be greater for these elements.

Table 3-1 Ionic radii [71] of relevant elements involved in this study

	$R^{CN\ (12)}$ Å	$R^{CN\ (6)}$ Å
Ba^{2+}	1.61	
O^{2-}		1.40
Ce^{4+}		0.87
La^{3+}	1.36	1.032
Nd^{3+}	1.27	0.983
Sm^{3+}	1.24	0.958
Gd^{3+}		0.938
Yb^{3+}		0.868

Ideally, one would like to quantify the relationship between stoichiometry and lattice parameters, and use this relationship to directly determine the concentration of M cations on the A and B sites from the experimental values of the lattice parameters. However, the lattice parameters of a perovskite compound cannot be determined *a priori* from the ionic radii of the species involved because of the octahedral tilting that is well known to occur in this structure type. Despite this phenomenon, there is an almost ideally linear relationship between the volume per formula unit of known ($Ba^{2+}M^{4+}O_3$) perovskites and the sum of the volumes of the species comprising the formula unit, presented in Fig. 3-5 and Table 3-2.

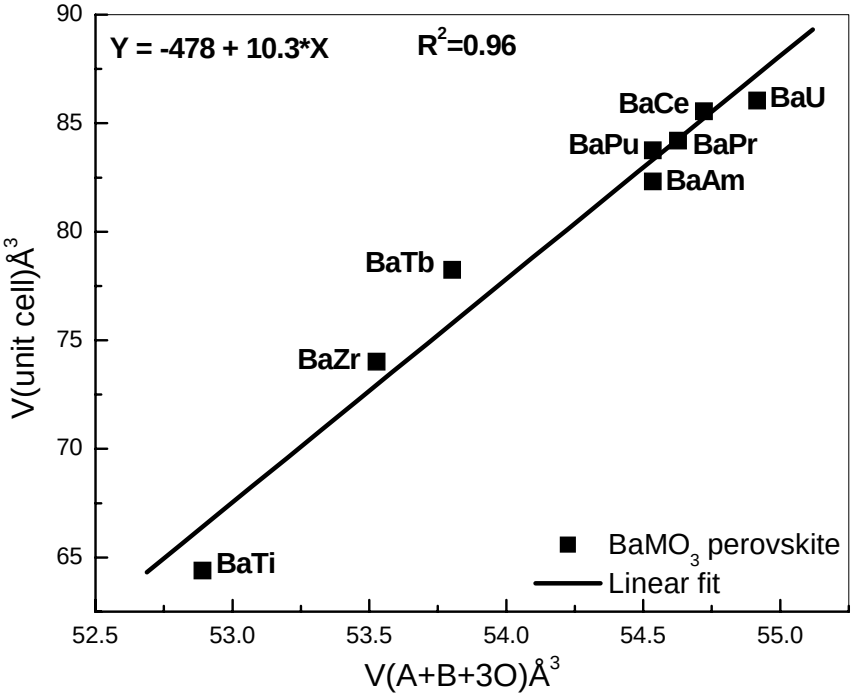

Fig. 3-5 Pseudo-cubic cell volume of barium based perovskites as a function of the sum of the ionic radii of the constituent species.

Table 3-2 Calculated and experimental unit cell volume of $Ba^{2+}M^{4+}O_{3-\delta}$ perovskite (pseudo-cubic structure)

comp.	Vol_B^{4+} (Å^3)	t factor*	Vol_{A+B+3O}(Å^3)	V_{ICSD}/unit(Å^3)	Ref. (ICSD#)
$BaTiO_3$	0.9276	1.0615	52.891	64.400	73646
$BaZrO_3$	1.563	1.0040	53.526	74.019	43136
$BaTbO_3$	1.839	0.9854	53.802	78.243	89028
$BaAmO_3$	2.572	0.9460	54.535	82.313	61317
$BaPuO_3$	2.664	0.9418	54.627	84.192	65033
$BaPrO_3$	2.572	0.9460	54.535	83.750	2753
$BaCeO_3$	2.758	0.9376	54.721	85.550	79625
$BaUO_3$	2.953	0.9294	54.916	86.040	84821

$$* \, t \, factor = \frac{(r_A + r_O)}{\sqrt{2}(r_B + r_O)}$$

The result indicates that the unusual cell volume behavior observed here for doped barium cerate cannot be readily explained by distortions of the unit cell (as consequence of octahedral tilting). The correlation implied by the data in Fig. 3-5 is

$$V_{cell} = -478(44) + 10.3(8) \times V_{sum} \ \text{Å}^3 \qquad (3\text{-}1)$$

Despite the large negative value of the constant term, under no conditions is the cell volume less than the sum of the ionic volumes of the species involved. The absolute numerical number of the error due to the fitting process is not small. However, the variation in cell volume between the various samples examined here and the overall deviation from the volume of undoped $BaCeO_3$ are small, and the error within this small range is thus considered negligible.

With the relationship (3-1), we can, ideally, utilize the measured cell volumes to determine the total volume of the species residing on the three sites of the perovskite cell. We first note, however, that this straight line correlation does not pass exactly through the data point for $BaCeO_3$, Fig. 3-5. Specifically, the experimental cell volume (per formula unit) is 85.550 Å^3, whereas it calculated at 85.240 Å^3 from Eq. (3-1). Accordingly, the relationship is modified by a correction factor to the form

$$V_{cell} = -479(44) + 10.3(8) \times V_{sum} \ \text{Å}^3 \qquad (3\text{-}2)$$

In order to apply this correlation to doped, possibly barium-deficient barium cerate, and determine the values of three unknowns, A-site occupancy, B-site occupancy, and anion site occupancy, from a single input parameter, we make the following assumptions/approximations: (1) both A and B sites are fully occupied (no cation vacancies), (2) M atom occupancy on the barium site will be sufficiently small so as to retain the validity of the correlation curve (derived only for barium based perovskites) to

the new composition and (3) anion vacancies, which result in order to maintain overall charge balance, have the same volume as the ions that would normally occupy those sites. The third approximation is considered reasonable in light of the radius assigned to an oxygen vacancy in perovskite structure ($r_{v_o^{\bullet\bullet}}$ = 1.4045 Å) by Mogensen *et al.*[72]. The first approximation results from the experimental observation that even slightly Ba deficient (undoped) barium cerate is unstable with respect to ceria precipitation[73], indicating that the concentration of A-site vacancies is extremely small, and from the large coulombic energy penalty expected from the absence of a tetravalent (B-site) ion from its normal site. Combined, these approximations imply that the occupation on the A and B sites can be respectively described as

$$A = \left(\frac{1-2y}{1-y}\right)Ba + \left(\frac{y}{1-y}\right)M \tag{3-3}$$

$$B = \left(\frac{0.85}{1-y}\right)Ce + \left(\frac{0.15-y}{1-y}\right)M \tag{3-4}$$

where 2y/(1-y) represents the fraction of Ba lost from the perovskite composition, and y/(1-y) the dopant occupancy on the A site. The parameter *y* is the amount of dopant on the A site before normalization for the adjusted stoichiometry of the perovskite.

The volumes associated with these species can then be estimated using the correlation relationship, Eq. (3-2), and defining the equivalent radii of the A and B-site cations as the weighted sums of the radii of the species that reside on those sites, while taking due care to employ the ionic radii appropriate for the 12-fold and 6-fold coordinates at these sites, respectively. Relevant ionic radii are summarized in Table 3-1. This analysis is applied to the nominally stoichiometric (SSR) samples and MP samples. The results, Table 3-3, presented for both calcined and sintered samples, provide a

measure of the extent to which the dopant incorporates on the A site in nominally stoichiometric compositions. The small cell volume of the Nd doped sample is now entirely reasonable, and indicates occupation of the A site by Nd at about the 2.5% level. La, as the largest dopant in this series, has a higher incorporation ratio on A-site than Nd does, however, the A-site shrinkage introduced by La is compensated by its large ionic radius compared with Nd, which leaves the La-doped sample the highest cell volume in spite of the high A-site incorporation ratio.

Table 3-3 Defect chemical parameters of stoichiometric $BaCe_{0.85}M_{0.15}O_{3-\delta}$ as derived from cell volume analysis. Number in parenthesis indicates uncertainty in the final digit(s).

Dopant	La	Nd	Sm	Gd	Yb
SSR V(exp.)Å^3 1300°C/12h	85.41(1)	85.05(4)	85.23(2)	85.24(1)	84.66(1)
[M] on A-site	0.034(2)	0.023(1)	0.016(2)	0.013(0)	0.008(0)
[M] on B-site	0.121(1)	0.130(1)	0.136(1)	0.139(0)	0.143(0)
δ	0.044(1)	0.053(1)	0.060(2)	0.063(0)	0.068(0)
Ba:(M+Ce)	0.934(2)	0.955(2)	0.968(3)	0.974(0)	0.984(0)
SSR V(exp.)Å^3 1550°C/4h		84.76(4)		85.05(3)	84.48(2)
[M] on A-site		0.026(1)		0.015(1)	0.010(0)
[M] on B-site		0.128(1)		0.137(0)	0.141(0)
δ		0.051(1)		0.061(0)	0.066(0)
Ba:(M+Ce)		0.949(2)		0.970(1)	0.980(0)
MP V(exp.)Å^3 1300°C/10h		85.25(3)		85.49(2)	84.77(2)
[M] on A-site		0.021(0)		0.011(0)	0.007(0)
[M] on B-site		0.132(0)		0.141(0)	0.144(0)
δ		0.055(0)		0.065(0)	0.068(0)
Ba:(M+Ce)		0.959(0)		0.978(0)	0.986(0)

As we mentioned earlier in Fig. 3-3, the variation in cell vomume with Ba content implies that there is some compositional range, Ba:(Ce+M), over which the perovskite phase exists, and that this range is dependent on the specific dopant. The observation of a composition independent lattice constant for Yb doped samples (with the exception of one apparently anomalous data point) is consistent with a perovskite phase of fixed stoichiometry, and almost no Yb on the A-site. This is consistent with the fact that ceria precipitates were observed for the Yb doped, barium deficient samples. In contrast, the Gd, Sm, Nd and, to some extent, the La-doped samples show measurable dependence of the cell volumes on stoichiometry, consistent with the presence of a single phase of variable composition. The increase in volume with increasing barium content is furthermore consistent with the increasing concentration of dopant on the B-site. The trends obtained from the two types of samples, solid state reaction synthesized and chemical route synthesized, are similar, but the absolute values of the cell volumes are measurably different. The different processing routes likely yield samples with different final barium contents. Similarly, the slight site incorporation difference between calcined and sintered samples listed in Table 3-3 may be attributable to the loss of Ba at high processing temperature.

3.4 Single Phase Limits by Chemical Analysis

Chemical analysis has two applications in this study: to identify phases for the probation of solubility limit of dopant on A-site and to measure experimental compositions compared to the nominal values.

Electron microprobe is used to confirm the single phase limit identified by XRD because of its high compositional resolution. Different phases are identified in terms of different brightness from the backscattered electron image. As an example, the backscattered electron image of the $Ba_{0.95}Ce_{0.85}Gd_{0.15}O_{3-\delta}$, $Ba_{1.0}Ce_{0.85}Gd_{0.15}O_{3-\delta}$, $Ba_{0.85}Ce_{0.85}Nd_{0.15}O_{3-\delta}$, $Ba_{1.0}Ce_{0.85}Nd_{0.15}O_{3-\delta}$ samples are shown in Fig. 3-6. Precipitates of a white fluorite phase of $(Ce,M)O_{2-\delta}$ are visible within the gray perovskite matrix in $Ba_{0.95}Ce_{0.85}Gd_{0.15}O_{3-\delta}$ and $Ba_{0.85}Ce_{0.85}Nd_{0.15}O_{3-\delta}$ while the nominally stoichiometric samples showed a homogeneous single phase.

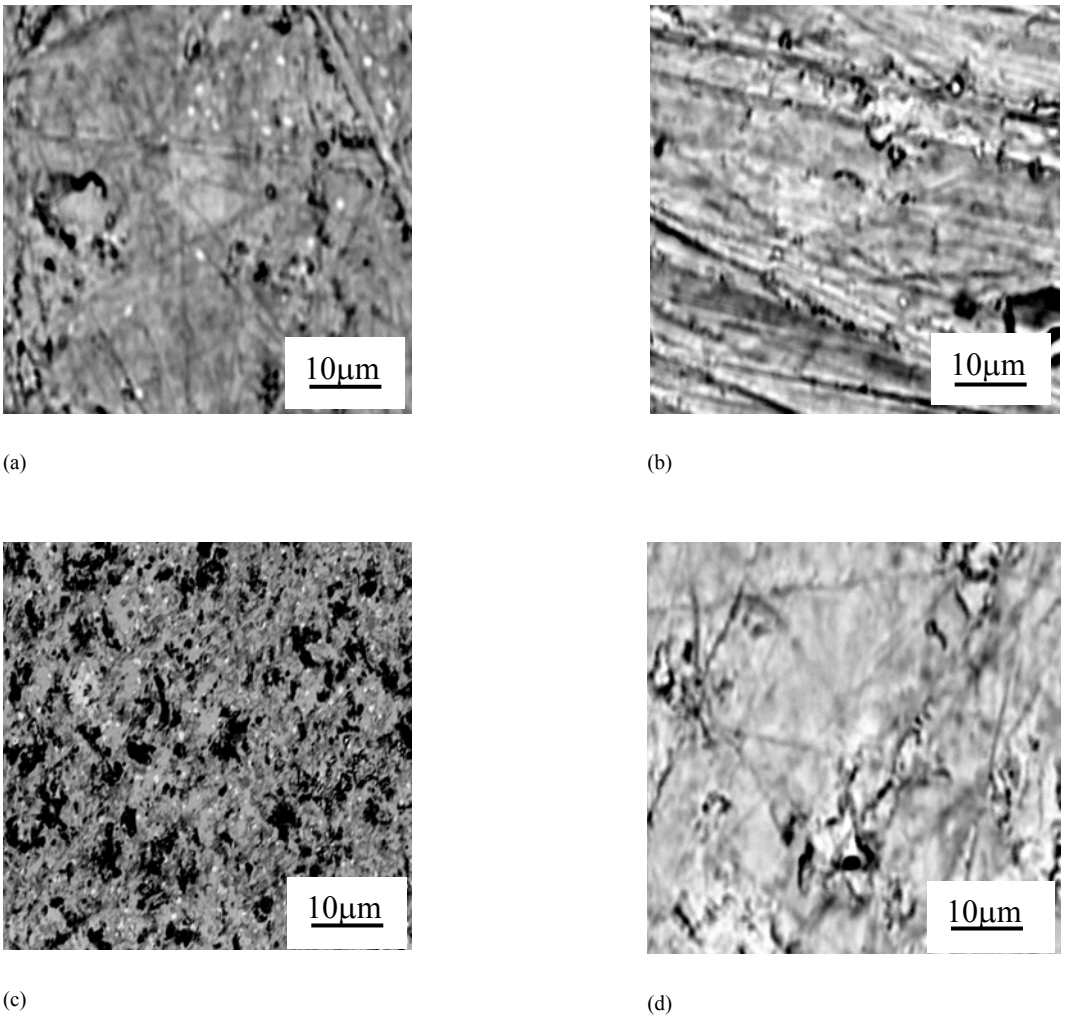

(a) (b)

(c) (d)

Fig. 3-6 Backscattered image of the sintered $Ba_xCe_{0.85}M_{0.15}O_{3-\delta}$ sample by electron microprobe (SSR, sintered at 1550°C/4 h) (a) $Ba_{0.95}Ce_{0.85}Gd_{0.15}O_{3-\delta}$; (b) $Ba_{1.0}Ce_{0.85}Gd_{0.15}O_{3-\delta}$; (c) $Ba_{0.85}Ce_{0.85}Nd_{0.15}O_{3-\delta}$; (d) $Ba_{1.0}Ce_{0.85}Nd_{0.15}O_{3-\delta}$

The experimentally measured compositions of the primary phase in sintered $Ba_xCe_{0.85}M_{0.15}O_3$ (M = Nd, Gd, Yb, x = 0.85-1.20) samples are shown in Fig. 3-7, here the measured Ba/(Ce+M) ratio is plotted as a function of the nominal value. For almost all of the samples, the experimental molar ratio of Ba/(Ce+M) falls below the nominal value. This tendency is especially pronounced for the nominally barium rich compositions. For example, a nominal stoichiometry of 20% Ba excess ($Ba_{1.2}Ce_{0.85}Nd_{0.15}O_{3+\delta}$) yields a measured value of at most 3.1% Ba excess, error included. Thus, it is clear that barium is lost from the bulk of the $Ba_xCe_{0.85}M_{0.15}O_3$ samples during the processing to obtain dense pellets.

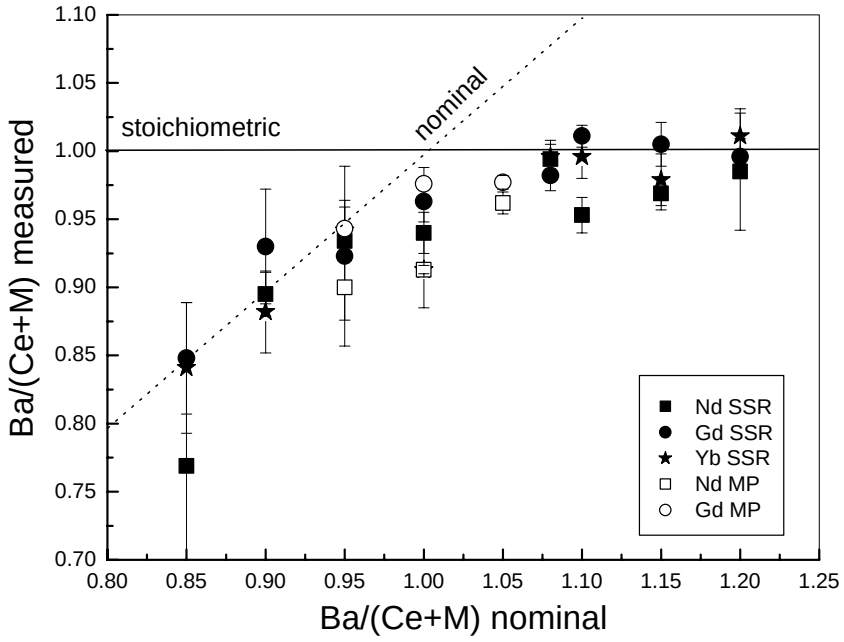

Fig. 3-7 Chemical composition of sintered $Ba_xCe_{0.85}M_{0.15}O_{3-\delta}$ (M = Nd, Gd, Yb, SSR and MP samples sintered at 1550°C/4 h), as measured by electron probe microanalysis. In cases where a minor secondary phase was observed, composition reported is that of the major phase.

Loss of Ba from the bulk region of $Ba_xCe_{0.85}M_{0.15}O_3$ can presumably occur either by barium accumulation in the grain boundary regions as an amorphous phase, undetectable via conventional X-ray powder diffraction, or by evaporation of BaO at high temperature. A comparison of the EDS spectra from grain boundary and bulk regions of $Ba_{1.2}Ce_{0.85}Nd_{0.15}O_{3+\delta}$ is presented in Fig 3-8. Even in the absence of a methodology for quantifying these data, it is evident from the ratios of the characteristic peak intensities that the grain boundary region contains a much higher molar ratio of Ba/Ce than does the bulk. Thus, it appears that compositions with substantial barium excess can accomodate high Ba concentrations in their grain boundary regions. It should also be noted that Al and Si are present in the grain boundary regions and this is likely due to contamination from glassware and ceramic crucibles, etc., used in the synthesis.

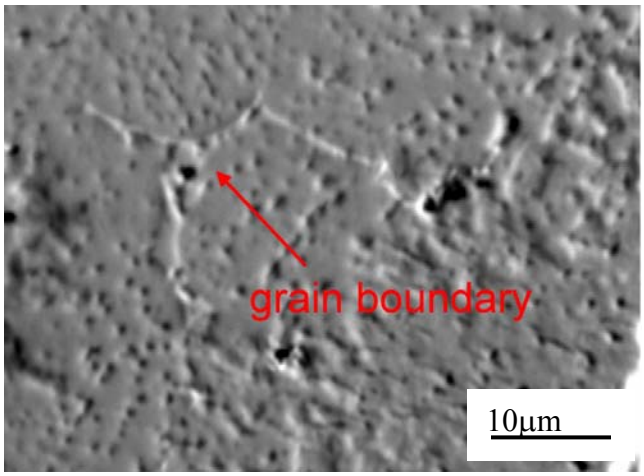

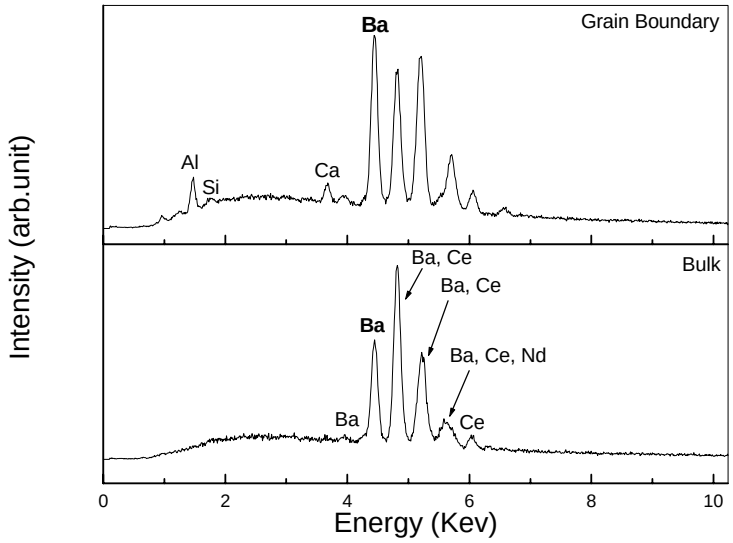

Fig. 3-8 (a) SEM image of etched $Ba_{1.2}Ce_{0.85}Nd_{0.15}O_3$, (b) EDS spectra obtained from the grain boundary (upper) and bulk (lower) regions of sintered, etched $Ba_{1.2}Ce_{0.85}Nd_{0.15}O_{3+\delta}$ (SSR, sintered at 1550°C/4 h, etched with concentrated HF).

Examination of the cross section of a sintered, nominally stoichiometric sample, $BaCe_{0.85}Gd_{0.15}O_{3-\delta}$ (SSR), confirmed that loss of BaO via evaporation occurs (in addition to BaO segregation). The backscattered electron image of this sample is shown in Fig. 3-9, and the corresponding chemical analysis presented in Fig. 3-10. A porous, $(Ce,Gd)O_{2-\delta}$ rich layer, around 20 μm in thickness, is evident on the surface of the pellet exposed to air during sintering. In contrast, the bulk is dense and chemically homogeneous. The relative content of Ba increases with the increasing distance from the surface to the bulk, until at around 100 μm the chemical composition becomes equal to that of the bulk. These sets of experiments demonstrate that BaO deficiencies occur by a combination of BaO accumulation in the grain boundary regions and BaO evaporation.

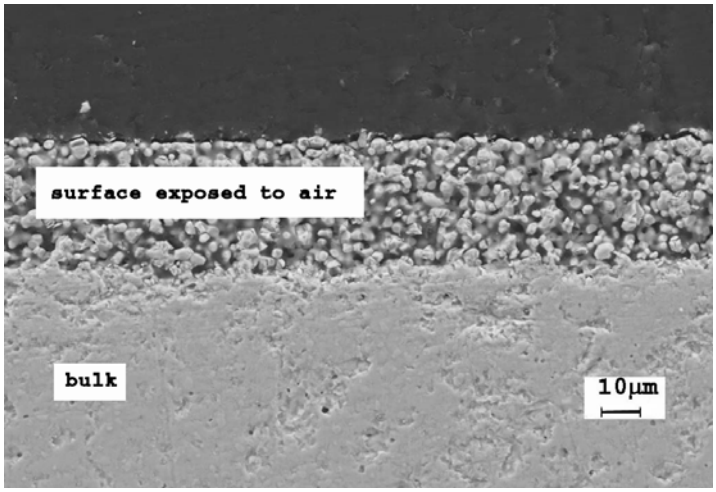

Fig. 3-9 Backscattered scanning electron microscopy image of the cross section of sintered $BaCe_{0.85}Gd_{0.15}O_{3-\delta}$ (SSR, sintered at 1550°C/4 h)

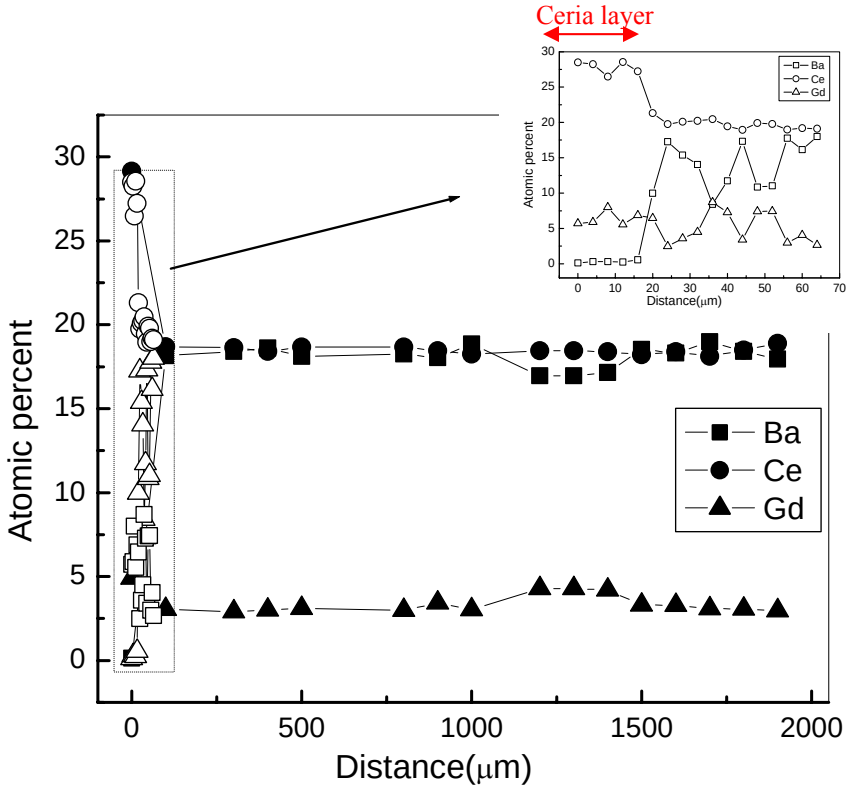

Fig. 3-10 Chemical composition as a function of distance from the surface, obtained from a cross section of sintered $BaCe_{0.85}Gd_{0.15}O_{3-\delta}$ (SSR, sintered at 1550°C/4 h); data collected by WDS (microprobe) methods.

In section 3.3 it is shown that even nominally stoichiometric barium cerate (of nominal composition $BaCe_{1-x}M_xO_{3-\delta}$) can have the dopant ion present on the A site. The maximum concentration of trivalent dopant ion that can be incorporated onto the perovskite A site can be determined from the compositions at which the ceria phase appears as a precipitate, if one again assumes that both A and B sites in the perovskite are fully occupied. Because of significant diffraction peak overlap between the perovskite and fluorite phases, the microprobe chemical analysis, Fig. 3-7, provides greater sensitivity to the presence of ceria precipitates than the X-ray powder diffraction measurements. The compositions, x^*, at which ceria was first observed are summarized in Table 3-4, where x is defined as the compositional ratio, [Ba]/([Ce] + [M]). Samples with x less than or equal to this critical value contained detectable amounts of ceria. Using Eqs. (3-3) and (3-4), we note that x is simply $1-2y$, and the maximum dopant concentration on the A site, y/(1-y), is also given as $y/(x+y)$. The results obtained from this analysis are provided in Table 3-4. The results obtained from X-ray single phase limit are shown as comparison. Little, if any Yb can be incorporated onto the perovskite A site, whereas as much as 50% of the Nd dopant can do so. The result obtained here for the Nd doped sample is in excellent agreement with that reported by Makovec *et al*. in their careful phase equilibria study of $BaCeO_3$-Nd_2O_3[35]. Again, the small but measurable differences between samples prepared by different routes indicate the sensitivity of defect chemistry to processing. The existence of the fluorite phase in the nominally stoichiometric Yb-doped sample (SSR) is likely due to the evaporation of BaO at high sintering temperature, resulting in a final composition which is slightly Ba deficient.

Table 3-4 Defect chemistry of doped barium cerate as determined by electron microprobe chemical and X-ray analysis, indicating the maximum solubility of dopant on A-site.

Dopant	*x** (a)	Max. y	y/(*x*+y)	Perovskite Composition
Nd (SSR)	0.85	0.075	8.1%	$(Ba_{0.919}Nd_{0.081})(Ce_{0.919}Nd_{0.081})O_3$
Gd (SSR)	0.95	0.025	2.6%	$(Ba_{0.974}Gd_{0.026})(Ce_{0.872}Gd_{0.128})O_{2.949}$
Yb (SSR)	1.0	0	0	$Ba(Ce_{0.85}Yb_{0.15})O_{2.925}$
Nd (MP)	--	--	--	--
Gd (MP)	0.95	0.025	2.6%	$(Ba_{0.974}Gd_{0.026})(Ce_{0.872}Gd_{0.128})O_{2.949}$
Yb (MP)	0.98	0.01	1.0%	$(Ba_{0.990}Yb_{0.010})(Ce_{0.859}Yb_{0.141})O_{2.935}$
Nd (SSR, XRD)	0.88	0.06	6.4%	$(Ba_{0.936}Nd_{0.064})(Ce_{0.904}Nd_{0.096})O_{2.984}$
Gd (SSR, XRD)	0.95	0.025	2.6%	$(Ba_{0.974}Gd_{0.026})(Ce_{0.872}Gd_{0.128})O_{2.949}$
Yb (SSR, XRD)	1.0	0	0	$Ba(Ce_{0.85}Yb_{0.15})O_{2.925}$

The microprobe chemical analysis does suggest that even nominally stoichiometric compositions are deficient in barium, Fig. 3-7. The actual stoichiometry of the nominally stoichiometric $BaCe_{0.85}M_{0.15}O_{3-\delta}$ (M=Nd, Gd, Yb) is then examined by microprobe as: $(Ba_{0.955}Nd_{0.045})(Ce_{0.889}Nd_{0.111})O_{2.967}$, $(Ba_{0.988}Gd_{0.012})(Ce_{0.860}Gd_{0.140})O_{2.936}$ and $(Ba_{0.998}Yb_{0.002})(Ce_{0.852}Yb_{0.148})O_{2.927}$, respectively. This agrees well with the results derived from cell volume analysis, in Table 3-3.

3.5 Conclusion

The defect chemistry, and, in particular, the dopant site incorporation preference in the perovskite $Ba_xCe_{0.85}M_{0.15}O_3$ (M=La, Nd, Sm, Gd, Yb) has been investigated. Within the entire Ba concentration range (x = 0.85-1.20), every sample examined exhibits Ba deficiency relative to the nominal composition. Chemical analysis clearly shows that BaO evaporates from the surface of sintered pellets, and also indicates the possible existence of an amorphous Ba rich phase at grain boundaries. The inversion of the cell volumes between the Gd-doped and Nd-doped samples can be explained by the more

extensive incorporation of Nd^{3+} ions onto the Ba^{2+}-site. XRD and microprobe analysis support these conclusions and yield a semi-quantitative measure of the concentration of dopant species on the A-site in nominally stoichiometric $BaCe_{0.85}M_{0.15}O_{3-\delta}$. The actual stoichiometry of the nominally stoichiometric compositions given by microprobe analysis is: $(Ba_{0.955}Nd_{0.045})(Ce_{0.889}Nd_{0.111})O_{2.967,}$ $(Ba_{0.988}Gd_{0.012})(Ce_{0.860}Gd_{0.140})O_{2.936}$ and $(Ba_{0.998}Yb_{0.002})(Ce_{0.852}Yb_{0.148})O_{2.927}$. The compositional limits for the maximum Ba^{2+}-site incorporation, as determined experimentally by microprobe analysis for the three dopant ions examined are given as: $(Ba_{0.919}Nd_{0.081})(Ce_{0.919}Nd_{0.081})O_3$, $(Ba_{0.974}Gd_{0.026})(Ce_{0.872}Gd_{0.128})O_{2.875}$ and $Ba(Ce_{0.85}Yb_{0.15})O_{2.925}$.

Chapter 4 Defect Chemistry of Barium Cerate by Extended X-ray Absorption Fine Structure (EXAFS) Method

4.1 Introduction

In this chapter extended X-ray absorption fine structure (EXAFS) method is adopted as a direct method to probe the defect chemistry of $BaCe_{0.85}Gd_{0.15}O_{3-\delta}$ and $BaCe_{0.85}Yb_{0.15}O_{3-\delta}$ synthesized by the modified Pechini process described in Chapter 2.

4.2 Introduction to EXAFS [74]

EXAFS refers to the oscillatory variation of the X-ray absorption as a function of photon energy beyond the absorption edge. Fig 4-1 exhibits a schematic EXAFS representation of an absorption edge of the absorbing atom.

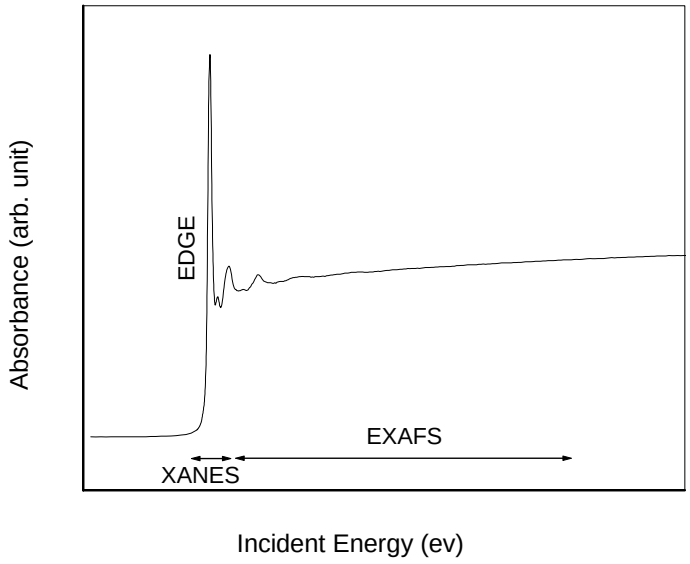

Fig. 4-1 Schematic EXAFS representation of an absorption edge of the absorbing atom

In an X-ray transmission experiment, the absorption coefficient μ is calculated by

$$\mu x = \ln(I_0 / I) \tag{4-1}$$

where I_0 and I are the intensities of the incident and transmitted beams and x is the sample thickness. The extended X-ray absorption spectroscopy measures the X-ray absorption coefficient μ as a function of photon energy E above the threshold of an absorption edge.

As for calculation, EXAFS can be defined as the function $\chi(E)$ by

$$\chi(E) = \mu(E) - \mu_0(E) \Big/ \mu_0(E) \tag{4-2}$$

where μ(E) is the experimental absorption coefficient and μ_0(E) is the atomic contribution to the absorption coefficient which is proportional to the number to atoms per unit volume. The difference [μ(E) - μ_0(E)] represents the EXAFS oscillations with the background subtracted. Via division by μ_0(E), the EXAFS oscillation χ(E) is normalized to a per atom basis. In order to obtain structure information, χ(E) is converted to χ(k) where k is the photon wave vector using the relationship

$$k = \sqrt{\frac{2m}{h^2}(E - E_0)} \tag{4-3}$$

m is the mass of the electron, h is Planck's constant, E is the kinetic energy of the photoelectron and E_0 is the energy of the photoelectron at k=0.

4.3 EXAFS Experiments

Extended X-ray absorption measurements were performed on $BaCe_{0.85}Gd_{0.15}O_{3-\delta}$ and $BaCe_{0.85}Yb_{0.15}O_{3-\delta}$ synthesized by the modified Pechini process described in Chapter 2.1. Experiments were carried out on beam line 2-3 at the Stanford Synchrotron

Radiation Laboratory (SSRL) at both liquid Helium and room temperatures. The instrument setup is illustrated in Fig. 4-2

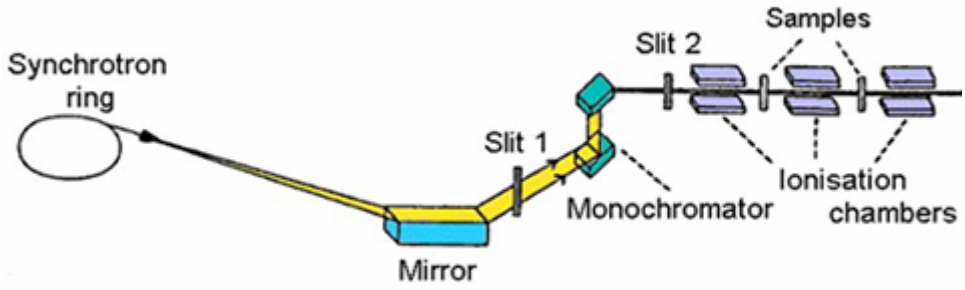

Fig. 4-2 (a) Schematic view of the EXAFS experimental setup

Fig. 4-2 (b) Photo of the EXAFS experimental setup chamber

The powders were diluted in BN powder at a 50/50 ratio. A Si (111) double crystal monochromator was used to tune the incident X-ray beam to the desired energies. X-ray absorption spectra were collected over the photoemission ranges of core Gd L_{III} (7242.8 eV) and Yb L_{III} (8943.6 eV) edges in fluorescence. The data were fitted over the

reciprocal space range (k-range) 3 to 11 $Å^{-1}$ and the real space range (R-range) 1 to 4 Å. Sixpack [75] and Feff[76] were used for data analysis.

4.4 Problem Statement and Approach

The two cation sites in ABO_3 perovskites exhibit different coordination numbers, with the A^{2+}-site being 12-fold coordinated and the B^{4+}-site being 6-fold coordinated. Consequently, the EXAFS spectra from dopants on one or the other of these two sites will differ, enabling the establishment of the dopant location in the structure. Indeed, EXAFS has already proved to be a useful tool for locating Yb and Nd in $CaZrO_3$ and some other perovskites.[48,77,78]

In their analysis of $CaZrO_3$, Davies *et al*. [48] assumed single site selectivity, that is, that the dopant was either entirely incorporated onto the A site or entirely onto the B site. In the case of $BaCeO_3$, there is ample evidence that dopants can partition over the two sites and partially occupy both positions, complicating analysis of the EXAFS data. In the approach here, we model the data for the two extremes of single site selectivity, and proportionately superimpose these two cases to fit the experimental data and describe the physical situation.

Before we proceed with the experiment, X-ray absorption edge energies of relative elements are checked, as listed in Table 4-1. It is difficult to run EXAFS on Nd doped samples due to the signal overlapping problem therefore only Gd and Yb doped samples were measured later.

Table 4-1 X-ray absorption edge energies of relative elements

Element	L1 edge (eV)	L2 edge (eV)	L3 edge (eV)
Ba	5988.8	5623.6	5247.0
Ce	6548.8	6164.2	5723.4
Nd	7126.0	6721.5	6207.9
Gd	8375.6	7930.3	7242.8
Yb	10486.4	9978.2	8943.6

Because the structure of undoped $BaCeO_3$ has been well investigated over a wide temperature range, it is straightforward to establish the nearest neighbors to the central absorbing atom, for both of the A^{2+} and the B^{4+} sites, as well as the distances to those neighbors. The data are summarized in Tables 4-2 and 4-3, using Ba and Ce as the central atom, respectively, and assuming the structure of $BaCeO_3$ reported by Knight *et al.*[24] (orthorhombic with a = 6.23573(3), b = 6.21611(4), c = 8.77694(5) Å). These data serve as the input for the two extremes of single site selectivity.

Table 4-2 Nearest neighbor distances about the Ba atom located at 0.001, 0.023, 0.250 in $BaCeO_3$ and their atomic coordinates, after Knight *et al.* [79]

Atom	Distance (Å)	x (frac. coor.)	y (frac. coor.)	z (frac. coor.)
O1	3.3603	0.071	-0.513	0.250
O1	2.9171	0.071	0.487	0.250
O1	3.5739	-0.571	-0.013	0.250
O1	2.6783	0.429	-0.013	0.250
O2	2.9695	-0.274	0.278	0.041
O2	3.5948	0.274	-0.278	0.541
O2	3.1658	0.226	0.222	-0.041
O2	2.7727	-0.226	-0.222	0.459
O2	3.5948	0.274	-0.278	-0.041
O2	2.9695	-0.274	0.278	0.459
O2	2.7727	-0.226	-0.222	0.041
O2	3.1658	0.226	0.222	0.541
Ce	3.9222	0	-0.500	0
Ce	3.6887	0	0.500	0
Ce	3.9222	0	-0.500	0.500
Ce	3.6887	0.00	0.500	0.500
Ce	3.8204	-0.500	0	0
Ce	3.8102	0.500	0	0
Ce	3.8204	-0.500	0	0.500
Ce	3.8102	0.500	0	0.500

Table 4-3 Nearest neighbor distances about the Ce atom located at 0.0, 0.5, 0.0, in $BaCeO_3$ and their atomic coordinates, after Knight *et al.* [79]

Atom	Distance (Å)	x (frac. coor.)	y (frac. coor.)	z (frac. coor.)
O1	2.2399	0.071	0.487	0.250
O1	2.2399	-0.071	0.513	-0.250
O2	2.2256	-0.274	0.278	0.041
O2	2.2587	0.226	0.222	-0.041
O2	2.2256	0.274	0.722	-0.041
O2	2.2587	-0.226	0.778	0.041
Ba	3.6887	0.001	0.023	0.250
Ba	3.9222	0.001	1.023	0.250
Ba	3.9222	-0.001	-0.023	-0.250
Ba	3.6887	-0.001	0.977	-0.250
Ba	3.8102	-0.499	0.477	-0.250
Ba	3.8204	0.501	0.477	-0.250
Ba	3.8204	-0.501	0.523	0.250
Ba	3.8102	0.499	0.523	0.250

To address the question of site partition probabilities, we introduce the fitting parameter *frac*. This parameter represents the amount of dopant incorporated onto the

B^{4+}-site, by atomic percentage, whereas *1-frac* is used to represent the amount that is incorporated onto A^{2+}-site. It is evident that the numerical range of *frac* is[80]. Using this formalism, the total EXAFS amplitude is described as[74]

$$\chi(k) = (1 - frac)\sum_i N_i S_l(k) F_i(k) e^{-2\sigma_i^2 k^2} e^{-2r_i/\lambda_i(k)} \frac{\sin(2kr_i + \phi_{il}(k))}{kr_i^2} + frac\sum_j N_j S_l(k) F_j(k) e^{-2\sigma_j^2 k^2} e^{-2r_j/\lambda_j(k)} \frac{\sin(2kr_j + \phi_{jl}(k))}{kr_j^2} \quad (4\text{-}4)$$

where N_i is the atom number of the i^{th} shell, $S_l(k)$ is the amplitude reduction factor due to many body effects at the central atom denoted by *l* which is linked to be the same to every path in our study, F_i is the backscattering amplitude from the ith type of atom, σ_i is the Debye-Waller factor representing the thermal vibration and static disorder, r_i is the distance between the absorber and the ith shell atoms, Φ_{il} is the total phase shift experienced by the photoelectron, λ_i is the electron mean free path and the term $e^{-2ri/\lambda i}$ is due to inelastic losses in the scattering process. Because of the low symmetry of the distorted orthorhombic perovskite structure, there are no more than two atoms (and in some case only one atom) per shell.

The analysis of EXAFS data generally involves background removal, normalization and μ_0 correction, conversion of energy, E, to wave vector, *k*, application of a weighting scheme, Fourier transformation of the data and, finally, model refinement to fit the processed data. Analysis in the present study focuses on the deduction of the parameter *frac*, which is accomplished in the final stage of model refinement. In addition, the M(Ba-site)-O, M(Ce-site)-O, M(Ce-site)-Ba, M(Ba-site)-Ce distances, the linked Debye-Waller (thermal displacement) factors and the parameter E_0 (used in the conversion from energy to wave vector) have been fitted as well.

4.5 Results and Discussion

EXAFS spectra typically refer to the range 40-1000 eV beyond the absorption edge. Above the absorption edge, weak oscillations are observed which arise from the constructive and destructive interference between the outgoing photoelectron wave from the core absorbing atom and the backscattered photoelectron wave from the near neighbors of the absorbing atom, as shown in Fig 4-3.

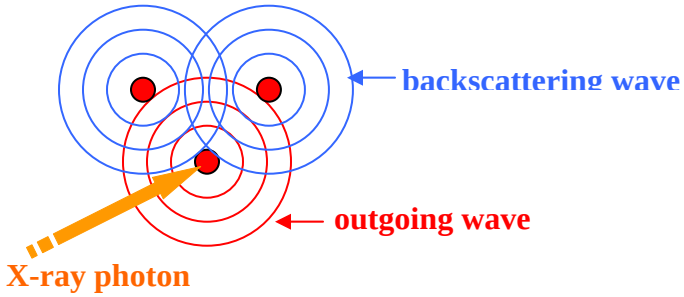

Fig. 4-3 Schematic explanation of the interaction between backscattering wave and outgoing wave

Fourier transformation of the oscillatory spectra yields a radial distribution function in real space which gives the local environmental information of the absorbing atom. Therefore EXAFS can be used as a molecular probe to analyze the distance from the absorber to near neighbors, the coordination number of the absorber and in some cases the type of the backscatters. This method can be used in both crystalline and amorphous solids as long as the absorber is surrounded by other atoms.

The oscillatory EXAFS spectra of Gd L_{III} and Yb L_{III} edges with the corresponding Fourier transforms are shown in Figs. 4-4 to 4-7. The first two present the 10 K and 300 K spectra, respectively, for Gd and the latter two the spectra for Yb. In all cases, the experimental data are compared with the best fit.

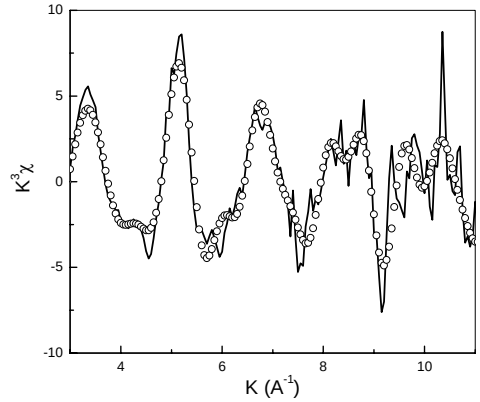

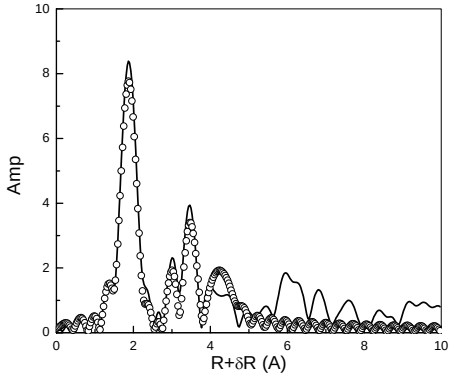

Fig 4-4 Gd L_{III} edge EXAFS for $BaCe_{0.85}Gd_{0.15}O_{3-\delta}$ measured at 10 K: experimental data (solid line), best fit data (open circles)

Fig 4-4 (a) the normalized EXAFS spectrum (k^3 weighted)

Fig 4-4 (b) the Fourier transform without the phase shift.

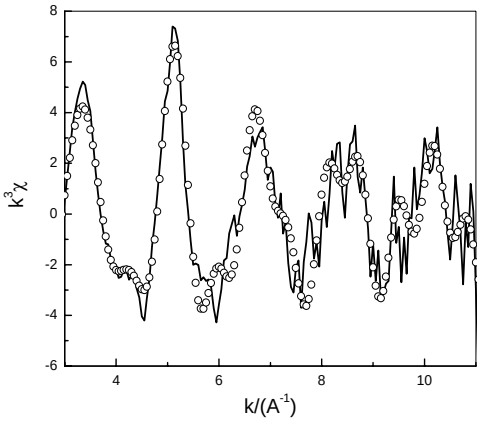

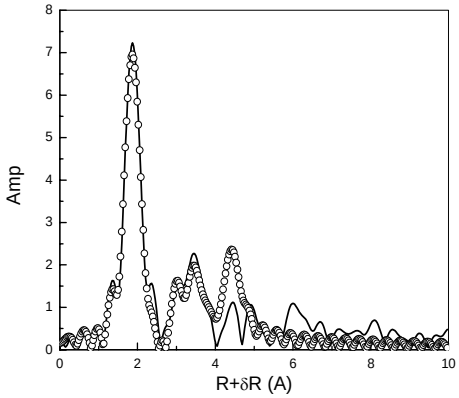

Fig 4-5 Gd L_{III} edge EXAFS for $BaCe_{0.85}Gd_{0.15}O_{3-\delta}$ measured at 300 K: experimental data (solid line), best fit data (open circles)

Fig 4-5 (a) the normalized EXAFS spectrum (k^3 weighted)

Fig 4-5 (b) the Fourier transform without the phase shift.

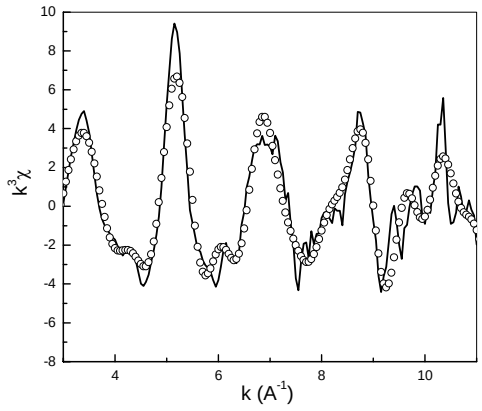

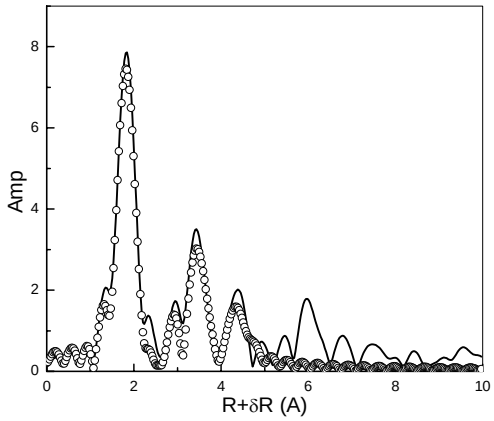

Fig 4-6 Yb L_{III} edge EXAFS for $BaCe_{0.85}Yb_{0.15}O_{3-\delta}$ measured at 10 K: experimental data (solid line), best fit data (open circles)

Fig 4-6 (a) the normalized EXAFS spectrum (k^3 weighted)

Fig 4-6 (b) the Fourier transform without the phase shift

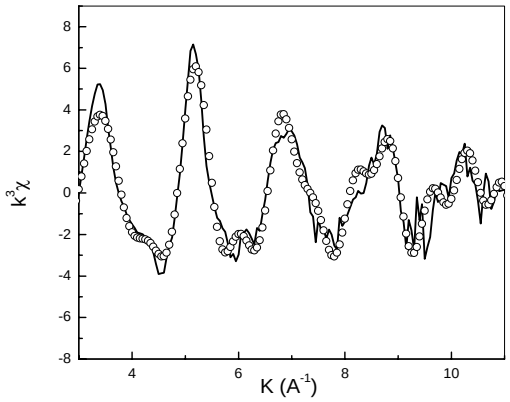

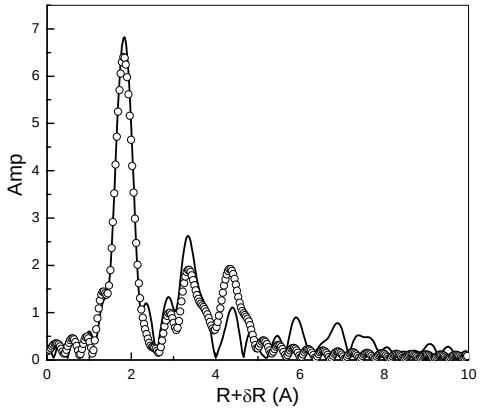

Fig 4-7 Yb L_{III} edge EXAFS for $BaCe_{0.85}Yb_{0.15}O_{3-\delta}$ measured at 300 K: experimental data (solid line), best fit data (open circles)

Fig 4-7 (a) the normalized EXAFS spectrum (k^3 weighted)

Fig 4-7 (b) the Fourier transform without the phase shift.

The structural parameters and refinement statistics obtained from the fitting procedure are summarized in Tables 4-4 and 4-5 for Gd and Yb, respectively. The refinement proceeded smoothly, yielding final residuals in the range 0.022 – 0.041, and χ^2 values in the range 1.7 - 25.

Table 4-4 Model refinement statistics and best-fit structural parameters for the Gd L_{III} edge EXAFS in $BaCe_{0.85}Gd_{0.15}O_{3-\delta}$

Shell (Gd on B^{4+}-site)	Atom type	Multi-plicity	Temp. (10 K)		Temp. (300 K)	
			R(Å)	σ^2(Å^2)	R(Å)	σ^2(Å^2)
1	O	2	2.298(7)	0.003(1)	2.298(8)	0.004(1)
2	O	2	2.298(7)	0.003(1)	2.298(8)	0.004(1)
3	O	2	2.298(7)	0.003(1)	2.298(8)	0.004(1)
Ave. Gd-O dist.			2.298		2.298	
4	Ba	2	3.834(10)	0.006(1)	3.860(11)	0.006(1)
5	Ba	2	3.834(10)	0.006(1)	3.860(11)	0.006(1)
6	Ba	2	3.992(3)	0.006(1)	4.004(7)	0.006(1)
7	Ba	2	3.992(3)	0.006(1)	4.004(7)	0.006(1)
Ave. Gd-Ba dist.			3.913		3.932	
Shell (Gd on A^{2+}-site)	Atom type	Multi-plicity	R(Å)	σ^2(Å^2)	R(Å)	σ^2(Å^2)
8	O	1	2.463(11)	0.001(1)	2.465(11)	0.001(1)
9	O	2	2.463(11)	0.001(1)	2.465(11)	0.001(1)
10	O	2	2.467(2)	0.001(1)	2.467(10)	0.001(1)
11	O	1	2.467(2)	0.001(1)	2.467(10)	0.001(1)
12	O	2	2.467(2)	0.001(1)	2.467(10)	0.001(1)
13	O	1	2.467(2)	0.001(1)	2.467(10)	0.001(1)
14	O	2	2.470(3)	0.001(1)	2.470(4)	0.001(1)
15	O	1	2.470(3)	0.001(1)	2.470(4)	0.001(1)
Ave. Gd-O dist.			2.467		2.467	
16	Ce	2	3.752(12)	0.001(1)	3.757(14)	0.002(1)
17	Ce	2	3.752(12)	0.001(1)	3.757(14)	0.002(1)
18	Ce	2	3.752(12)	0.001(1)	3.757(14)	0.002(1)
19	Ce	2	3.752(12)	0.001(1)	3.757(14)	0.002(1)
Ave. Gd-Ce dist.			3.752		3.757	
Frac			0.869(10)		0.866(9)	

k range	(3,11)	(3,11)
Chi^2	1.71	2.89
R factor	0.0223	0.022

Table 4-5 Model refinement statistics and best-fit structural parameters for the Gd L_{III} edge EXAFS in $BaCe_{0.85}Gd_{0.15}O_{3-\delta}$

Shell (Yb on B^{4+}-site)	Atom type	Multi-plicity	Temp. (10K)		Temp. (300K)	
			R(Å)	σ^2(Å^2)	R(Å)	σ^2(Å^2)
1	O	2	2.239(4)	0.005(1)	2.242(5)	0.007(1)
2	O	2	2.239(4)	0.005(1)	2.242(5)	0.007(1)
3	O	2	2.239(4)	0.005(1)	2.242(5)	0.007(1)
Ave. Yb-O dist.			2.239		2.242	
4	Ba	2	3.708(5)	0.006(1)	3.734(4)	0.008(2)
5	Ba	2	3.708(5)	0.006(1)	3.734(4)	0.008(2)
6	Ba	2	3.853(6)	0.006(1)	3.890(5)	0.008(2)
7	Ba	2	3.853(6)	0.006(1)	3.890(5)	0.008(2)
Ave.Yb-Ba dist.			3.781		3.812	
Shell (Yb on A^{2+}-site)	Atom type	Multi-plicity	R(Å)	σ^2(Å^2)	R(Å)	σ^2(Å^2)
8	O	1	2.414(8)	0.002(1)	2.416(8)	0.003(1)
9	O	2	2.414(8)	0.002(1)	2.416(8)	0.003(1)
10	O	2	2.414(8)	0.002(1)	2.416(8)	0.003(1)
11	O	1	2.414(8)	0.002(1)	2.416(8)	0.003(1)
12	O	2	2.417(8)	0.002(1)	2.420(7)	0.003(1)
13	O	1	2.417(8)	0.002(1)	2.420(7)	0.003(1)
14	O	2	2.417(8)	0.002(1)	2.420(7)	0.003(1)
15	O	1	2.417(8)	0.002(1)	2.420(7)	0.003(1)
Ave. Yb-O dist.			2.416		2.418	
16	Ce	2	3.678(8)	0.002(1)	3.679(8)	0.008(2)
17	Ce	2	3.678(8)	0.002(1)	3.679(8)	0.008(2)
18	Ce	2	3.678(8)	0.002(1)	3.679(8)	0.008(2)
19	Ce	2	3.678(8)	0.002(1)	3.679(8)	0.008(2)
Ave.Yb-Ce dist.			3.678		3.679	
Frac			0.964(8)		0.953(12)	
k range			(3,11)		(3,11)	

Chi^2	25.48	20.26
R factor	0.0311	0.0413

The defect chemical parameters and overall stoichiometries implied by the fitted models are summarized in Table 4-6, where they are also compared with the results of the X-ray powder diffraction analysis and electron microprobe chemical analysis from Chapter 3. It should be noted that because increased BaO loss and dopant incorporation onto the barium site are expected with high temperature processing[73,36], the microprobe results, obtained from sintered pellets, are not directly comparable to the EXAFS and diffraction results, obtained from calcined powders. Rather, a similarity in general trends with dopant species is expected.

Table 4-6 Defect chemical parameters and stoichiometry of nominally $BaCe_{0.85}M_{0.15}O_{3-\delta}$ materials (M = Gd, Yb) as derived from EXAFS and compared with the results of X-ray diffraction analysis and microprobe analysis.

Dopant	Gd		Yb	
	10 K	300 K	10 K	300 K
[M] on A-site	0.020(2)	0.021(1)	0.005(1)	0.007(2)
[M] on B-site	0.133(2)	0.133(1)	0.145(1)	0.144(2)
δ	0.056(2)	0.056(1)	0.070(1)	0.068(2)
Ba:(M+Ce)	0.961(3)	0.960(2)	0.989(2)	0.986(4)
Composition by EXAFS at 300K	$(Ba_{0.980}Gd_{0.020})(Ce_{0.867}Gd_{0.133})O_{2.944}$		$(Ba_{0.993}Yb_{0.007})(Ce_{0.856}Yb_{0.144})O_{2.932}$	
Ba:(M+Ce) by XRD[a]	0.978(0)		0.986(0)	
Composition by XRD[a]	$(Ba_{0.989}Gd_{0.011})(Ce_{0.859}Gd_{0.141})O_{2.935}$		$(Ba_{0.993}Yb_{0.007})(Ce_{0.856}Yb_{0.144})O_{2.932}$	
Ba:(M+Ce) by microprobe analysis[a]	0.976(12)		0.996(12)	
Composition by Microprobe analysis[a]	$(Ba_{0.988}Gd_{0.012})(Ce_{0.860}Gd_{0.140})O_{2.936}$		$(Ba_{0.998}Yb_{0.002})(Ce_{0.852}Yb_{0.148})O_{2.927}$	

[a]: cited from Chapter 3.

The results of Tables 4-4 to 4-6 reveal several important points. Most significant is that measurable dopant site partitioning indeed occurs, with the *frac* parameter differing from a value of 1 by several standard deviations for both composition. Furthermore, as anticipated and consistent with previous studies, the extent of Yb incorporation onto the A site (~ 4%) is less than Gd incorporation onto that site (~ 13%). From the analysis of the cell volumes in Chapter 3, the extent of Yb, Gd and Nd incorporation onto the Ba site was inferred to be 4.6, 7.2, and 14%, respectively, the first two values being in reasonable agreement with the present EXAFS results. Similarly qualitative, though not quantitative, agreement is found with the results of the electron microprobe chemical analysis. The chemical analysis measurements showed Ba:(Ce+M) molar ratios of 0.996, 0.976 and 0.913 for Yb, Gd, and Nd, respectively, whereas the ratios implied by the EXAFS results for the first two dopant species are 0.989 and 0.961, respectively (at 10 K). Although the EXAFS Nd experiments could not be performed, one can extrapolate from these results and conclude that Nd incorporation onto the Ba site would be greater than the 13% measured here for Gd, and the Ba:(Ce+M) ratio lower than 0.961. As a consequence of the dopant partitioning, the concentration of oxygen vacancies is reduced, as inferred from the EXAFS analysis, from the desired value of 7.5 mol% of the oxygen sites [= ½ the dopant concentration] to ~ 7% for Yb and ~ 5.5% for Gd.

A second important observation is that, upon doping, the structure of barium cerate undergoes local distortions. That is, the distances from the central dopant atom to the nearest neighbors differ from the comparable distances in undoped barium cerate. This distortion results directly from the size “mismatch” between Ba, Ce and the dopants.

Furthermore, because the difference in ionic radii is relatively small between Ce and the dopants, the distortion about the B site is substantially less than that about the A site. The mean Ce-O distance in undoped barium cerate is 2.241(4) Å, whereas Gd-O and Yb-O distances for the dopants on the cerium site are 2.298(4) and 2.239(5) Å, respectively. In contrast, the comparable mean A-O distances are 3.13(30), 2.467(2) and 2.418(3) Å for Ba, Gd and Yb, respectively. It is noteworthy that introduction of Yb onto the Ce site, in fact, produces almost no local changes in average bond distances. This, combined with the fact that the extent of Yb incorporation on the Ba site is small, indicates that the observed decrease in cell volume upon Yb doping, Fig. 3-4, is primarily attributable to oxygen vacancies which presumably have a smaller effective ionic radius than occupied oxygen sites [72]. These kinds of detailed observations demonstrate the strength of the EXAFS method over conventional X-ray powder diffraction for the study of defect chemistry. The powder diffraction pattern reveals the average structure, which changes only slightly upon dopant introduction. In contrast, the EXAFS spectrum is highly sensitive to the local structure through distinct changes in the sharp features of the radial distribution function.

A final result to note from the data of Figs. 4-4 to 4-7 and Tables 4-4 and 4-5 is the significantly lower thermal disorder in the samples examined at 10 K than at room temperature. In particular, the spectra in Figs. 4-4 and 4-6 are sharper than those of Figs 4-5 and 4-7. The derived Debye-Waller factors, σ^2, being slightly smaller for the 10 K refinements, reflect this difference in disorder. The other parameters, however, are comparable for the two temperatures, suggesting no unusual effects on cooling (Tables 4-4, 4-5).

4.6 Conclusion

The dopant site incorporation preference in perovskites of nominal stoichiometry $BaCe_{0.85}M_{0.15}O_{3-\delta}$ (M = Nd, Gd, Yb) has been investigated in depth. By fitting a weighted average of two separate structures, one with the dopant on the A site and the second with the dopant on the B site, EXAFS data, collected for the dopants Gd and Yb, have been accurately modeled. The analysis shows that 4.6% of the Yb and 13.6% of the Gd intended for incorporation onto the Ce site, in nominally stoichiometric $BaCe_{0.85}M_{0.15}O_{3-\delta}$, resides on the Ba site. As a consequence, the concentration of oxygen vacancies is reduced from the ideal value of 7.5 mol% of the oxygen sites [= ½ the dopant concentration] to ~ 7% for Yb and ~ 5.6% for Gd. Accordingly, dopants of larger ionic radii, which exhibit a greater extent of dopant incorporation onto the A^{2+} site, exhibit lower proton uptake and conductivity upon exposure to humid atmospheres than dopants with smaller ionic radii. In addition, although Yb resides primarily on the Ce site and no measurable local structural distortions in $BaCeO_3$ were observed upon introduction of this dopant, the overall cell volume of the perovskite decreased noticeably. This is attributed to the smaller effective ionic radii of oxygen vacancies than physically present oxygen ions.

Chapter 5 Defect Chemistry of Barium Cerate by Computational Methods

5.1 Introduction

In this chapter, static lattice computational methods are adopted to directly investigate the defect chemistry of barium cerate on the atomic scale and, in particular, the possible influence of cation non-stoichiometry on dopant site occupancy. Static lattice simulation methods have been successfully employed to investigate the defect properties of a range of perovskite-type proton and oxide-ion conductors[81,34,82,83]. Here, the particular trivalent dopant ions, Yb, Y, Gd, Nd and La, are examined.

5.2 Methodology and Problem Statement

Static lattice simulations are based on the specification of a potential model which describes the potential energy of the system as a function of the atomic co-ordinates and allows the modeling of both perfect and defective lattices. Only a brief account of these widely used techniques (embodied within the GULP code[82]) will be presented, as comprehensive reviews are given elsewhere[83].

The Born model representation, commonly used for ternary oxides, is employed here, with the energy partitioned into long-range Coulombic and short-range pair (and three-body) potentials. A simple analytical function of the Buckingham form

$$V_{ij}(r_{ij}) = A_{ij}\exp(-r_{ij}/\rho_{ij}) - C_{ij}/r_{ij}^{6} \qquad (5\text{-}1)$$

is used to describe the two-body, short-range interactions within the crystal, where V_{ij} is the potential energy between any two atoms i and j, A_{ij}, ρ_{ij} and C_{ij} are the parameters

describing the potential between those atoms, and r_{ij} is the distance between them. Values of these parameters for the elements relevant to this work are listed in Table 5-1.

Table 5-1 Interatomic potential parameters

M…O	A(eV)	ρ(Å)	C(eV Å^6)	Y(e)	k(eV Å^{-2})	U_L(eV)	Ref
O^{2-}	22764.3	0.1490	27.89*	-2.077*	27.29*	…	[84]
Ba^{2+}	931.7	0.3949	0.0	1.46	14.78	-31.33*	[85]
Ce^{4+}	1986.83	0.3511	20.40*	7.7	291.75	-105.31*	[86]
La^{3+}	1545.21	0.3590	0.0	-0.25	145.00	-129.06	[84]
Nd^{3+}	1379.9	0.3601	0.0	3.0	99999	-129.22	[87]
Gd^{3+}	1336.8	0.3551	0.0	3.0	99999	-132.16	[87]
Y^{3+}	1345.1	0.3491	0.0	3.0	99999	-134.74	[87]
Yb^{3+}	1309.6	0.3462	0.0	3.0	99999	-136.76	[87]

A, ρ, and C are parameters assigned to the cation-oxide anion interaction, Eq, (5-1), Y is the shell charge and k is the harmonic force constant, where Y and k are used in the shell model of ionic polarizability. U_L refers to the lattice energy of the oxide. Entries marked with an * are updated relative to ref. [34]

As charged defects will polarize other ions in the lattice, ionic polarizability must be incorporated into the potential model. This is achieved via the shell model, which describes such effects by treating each ion in terms of a core (representing the nucleus and core electrons) connected *via* a harmonic spring to a shell (representing the valence electrons). The shell model has been shown to simulate effectively both dielectric and elastic properties of ceramic oxides, by including the vital coupling between the short-range repulsive forces and ionic polarization.[88,89]

Lattice relaxation around a charged defect causes extensive perturbation of the surrounding lattice. Defect modeling of such effects is performed here using the two-

region Mott-Littleton approach, which partitions the crystal lattice into two spherical regions. Ions in the central inner region (typically containing more than 250 ions) surrounding the defect are relaxed explicitly. In contrast, the remainder of the crystal (> 2000 ions), where the defect forces are relatively weak, is treated by more approximate quasi-continuum methods. In this way, local relaxation is effectively modeled, and the crystal is not treated simply as a rigid lattice.

While mean field theory, in which point defects are treated via a correction to the potential energy terms of particular atoms to generate an 'average' species, has been successful for treating defects in related systems[37] and even for the examination of other aspects of $BaCeO_3$[34], this approach was found to be unsuitable here for a variety of reasons. Instead, a supercell approach has been implemented, with specific atom sites within the expanded cell (of overall symmetry P1) serving as the locations of particular point defects. The supercell method presents its own set of challenges in that multiple defect configurations must be examined in order to identify that with the lowest energy. For example, for BaO deficiency with one cation vacancy on the barium site and one anion vacancy, the proximities of these two defects must be considered: as nearest neighbors, as next nearest neighbors, *etc*. To achieve a meaningful result within a finite time period, the strategy pursued here involved identification of the lowest energy configurations using relatively small supercells (2×2×2) and transferring these most probable configurations to progressively larger supercells. Final calculations were performed on 3×4×4 and 3×3×5 supercells. Introduction of two dopant ions within these supercells leads to dopant concentrations of ~ 4%, which are typical of experimental values.

The specific question that this work aims to answer is as follows: Given a nominal stoichiometry for a doped barium cerate perovskite, can the actual stoichiometry differ as a result of barium oxide evaporation (or accumulation in grain boundary regions) and dopant redistribution? The question can be formulated quantitatively in terms of the reaction

$$Ba(Ce_{1-x}M_x)O_{3-\delta} \rightarrow (Ba_{1-y}M_y)(Ce_{1-x}M_z)O_{3-\delta'} + yBaO \qquad (5\text{-}2)$$

Is this reaction energetically favored and to what extent do the thermodynamics depend on the particular dopant species?

In considering the stoichiometry of the barium deficient composition, it is apparent that the degree of dopant incorporation onto the A-site determines the sign of the charge compensating defect. For $y < z$, negatively charged M'_{Ce} defects outnumber positively charged $M^{\bullet}_{Ba}$ defects, and oxygen vacancies are thus expected to the primary type of compensating defect. For $y > z$, A-site vacancies (with negative charge) can be anticipated as the primary charge compensating defect. In either case, B-site vacancies are not anticipated, thus $z = x$ after appropriate normalization of the overall stoichiometry. Calculation of the energetics of the complex perovskite, $(Ba_{1-y}M_y)(Ce_{1-z}M_z)O_{3-\delta'}$, presents computational challenges because of the multiple local configurations that must be considered in order to identify that which corresponds to the lowest energy. A simpler but equally valuable approach is to, instead, consider the energetics of the two extreme cases with the dopant entirely on one site or the other, and then calculate the energy of the reaction

$$Ba(Ce_{1-x}M_x)O_{3-\delta} \rightarrow [1-x](Ba_{1-y}M_{\frac{2}{3}y}V_{\frac{1}{3}y})CeO_3 + zBaO \qquad (5\text{-}3)$$

where V is a Ba vacancy, y = 3x/2(1-x) and z = [1-(1-x)(1-y)], from the lattice energies of the three compounds, $Ba(Ce_{1-x}M_x)O_{3-\delta}$, $(Ba_{1-y}M_{y/2}V_{y/2})CeO_3$, and BaO.

In the ideal case, arbitrary values for x, y and z can be examined. In a supercell of finite size, however, the stoichiometric variables are not continuous but rather have discrete values. Use of two different sized supercells addresses this limitation. Specifically, full Ce-site occupancy by the dopant is evaluated here using a 3×4×4 supercell of composition $Ba_{48}(Ce_{46}M_2)O_{143}$ [= $Ba(Ce_{0.958}M_{0.042})O_{2.993}$] whereas full Ba-site occupancy is evaluated using a 3×3×5 supercell of composition $(Ba_{42}M_2V_1)Ce_{43}O_{135}$ [= $(Ba_{0.933}\ M_{0.044})CeO_3$]. The specific reaction in this case then becomes

$$Ba_{48}(M_2Ce_{46})O_{143} \rightarrow 46/45(Ba_{42}M_2V)Ce_{45}O_{135} + (5+1/15)\ BaO \qquad (5\text{-}4)$$

and the total energy is calculated according to

$$\Delta E = 1.022E[(Ba_{42}M_2)CeO_3] + 5.067E[(BaO)] - E[Ba_{48}(M_2Ce_{46})O_{143}] \qquad (5\text{-}5)$$

Note that due to compositional round-off errors, reaction (5-4) is not precisely mass balanced with respect to M_2O_3, however, this is a small error in light of other uncertainties in the calculation.

To facilitate comparisons with previous studies[34] we have also performed calculations in which the energetics of dopant substitution is calculated. The dopant cations are incorporated in the lattice at either the Ce^{4+} or Ba^{2+} sites written explicitly as

$$BaCeO_3 + xM_2O_3 \rightarrow Ba(Ce_{1-2x}M_{2x})O_{3-x} + 2xCeO_2, \text{ and} \qquad (5\text{-}6)$$

$$BaCeO_3 + xM_2O_3 \rightarrow (Ba_{1-3x}M_{2x}V_x)CeO_3 + 3xBaO, \qquad (5\text{-}7)$$

respectively. The energies of these 'solution' reactions are evaluated from the calculated lattice energies of the undoped and doped perovskite (using 3×4×4 supercells and one formula unit M_2O_3 per 48 formula units $BaCeO_3$), and from the literature lattice energies of the binary oxides, U_L of Table 5-1. Analysis of the difference between the solution energies of these reactions, ΔE = E(Ba-site) – E(Ce-site), provides a measure of the relative preference of the dopant for the Ce site over the Ba site and eliminates the influence of the lattice energies of the dopant metal oxides, which can overwhelm all other terms in the reaction.

In an earlier study by Glockner *et al.*[34], studies of the defect chemistry of barium cerate were carried out using the mean field approach in conjunction with static lattice simulations. Three key results of that work are relevant to the present study: (1) The energetics of the cubic and orthorhombic forms of $BaCeO_3$ are almost identical; (2) for all dopants examined from Yb^{3+} to La^{3+}, incorporation onto the Ce site was found to be more favorable than onto the Ba site, but with the energy difference decreasing with increasing ionic radius; and (3) in undoped $BaCeO_3$, barium and oxygen vacancy pairs, created according to reaction (5-8) are the most energetically favorable intrinsic defects,

$$Ba^{x}_{Ba} + O^{x}_{o} \rightarrow V_{Ba}^{''} + V_{o}^{\bullet\bullet} + BaO \qquad (5\text{-}8)$$

although the total energy for even this reaction (6.4 eV) was found to be relatively high. This last result is consistent with the observation of A-site vacancies in perovskites such as $BaTiO_3$[90,91] and the loss of barium oxide from barium cerate based materials at elevated temperatures. In the case of undoped barium cerate, however, compositions with just 1% deficiency (i.e. $Ba_{0.99}CeO_3$) result in two phase mixtures of the perovskite and ceria[92,36]. This suggests that any slight barium deficiency that is sustained in the undoped

structure occurs at levels that cannot be easily detected experimentally, in accord with the computational result of a rather high defect reaction energy. Here, in addition to evaluation of reaction (5-3) by the supercell approach, extensive computations on BaO deficient stoichiometries have been performed in order to assess the likelihood of barium loss via the reaction

$$BaCeO_3 \rightarrow Ba_{1-x}CeO_{3-x} + xBaO \qquad (5\text{-}9)$$

particularly in the presence of dopant ions. In the physical reality, BaO is likely to be removed in vapor form, however, calculations here were carried out assuming crystalline BaO, for which the lattice energy could be evaluated.

5.3 Results and Discussion

5.3.1 Structural Modeling and Intrinsic Defects of $BaCeO_3$

Before carrying out defect calculations, the unit cell dimensions and ion positions of the cubic phase (PM-3M, a = 4.445 Å) were equilibrated under constant pressure at 0 K conditions using a 1×1×1 cell. The unit cell parameters change only slightly on relaxation of the structure. The differences in the observed and calculated lattice parameters and bond distances, Table 5-2, are within 0.4% for cubic $BaCeO_3$, indicating that the potentials reproduce the perovskite structure, although selected parameters are slightly updated from ref [34]. Essentially identical structural results were obtained from the supercell calculations (in which, by definition, the structure was not constrained to be cubic). The energetics of intrinsic defect formation in (undoped) $BaCeO_3$ obtained from

the 1×1×1 cell were, furthermore, within 5% of the earlier results[34] and are not reproduced here.

Table 5-2 Calculated structural parameters of cubic $BaCeO_3$ as determined from a conventional 1 × 1 × 1 cell calculation and compared to experimental values.

Property	Calculated	Experimental[24]
Lattice parameter a(Å)	4.427(2)	4.44467(2)
Bond distances (Å)		
Ba-O	3.130(5)	3.143
Ce-O	2.213(6)	2.223
Lattice energy (eV)	-136.68	--

5.3.2 Dopant Incorporation

Before analyzing the defect chemistry of doped barium cerate, the consistency between the conventional 1×1×1 cell calculations and those of the supercells was checked by comparing lattice energies and Ba-O vacancy pair formation energies. The results, Table 5-3, show quantitative agreement in terms of lattice energies of stoichiometric compositions. In contrast, the supercell calculations (which are in good agreement with each other at reaction energy of ~ 5.4 eV) indicate defect creation energies which are somewhat lower than the conventional calculation using isolated point defects (~ 6.4 eV).

Table 5-3 Normalized lattice energy of stoichiometric and barium oxide deficient barium cerate in 3×4×4 and 3×3×5 supercells, and compared to the values for the 1×1×1 cell calcuation

Cell		Composition	Lattice energy / unit cell (eV)	Reaction energy[a] (eV)
$BaCeO_3$	1×1×1	$BaCeO_3$	-136.68	6.38
$Ba_{48}Ce_{48}O_{144}$	3×4×4	$BaCeO_3$	-136.68	} 5.33
$Ba_{47}Ce_{48}O_{143}$	3×4×4	$Ba_{0.979}CeO_{2.979}$	-135.91	
$Ba_{45}Ce_{45}O_{135}$	3×3×5	$BaCeO_3$	-136.68	} 5.54
$Ba_{44}Ce_{45}O_{134}$	3×3×5	$Ba_{0.978}CeO_{2.978}$	-135.86	

[a] for the formation of Ba and O vacancy pairs [see text, Eq. (5-9)].

The difference likely reflects the influence of defect interactions. Such interactions are present in the supercell calculations but not the conventional calculations, which represent the dilute limit of isolated defects in an infinite crystal. If such an interpretation is correct, it further implies that barium cerate exhibits slightly non-ideal solution behavior, with the chemical potential of defects being a function of defect concentration. Because of the uncertainties generally associated with lattice energy calculations, we focus on relative trends with respect to dopant type rather than the absolute energy values.

The energetics of Ba-O vacancy pair formation in the presence of dopant elements (on the B-site) are presented in Table 5-4. Although there is no particular trend with ionic radius, it is apparent that the presence of B-site dopants raises the energetic penalty for the formation of these defects (from ~ 5.3 eV for a 3x4x4 cell to 6.0-6.7 eV). This result may be related to the non-ideal solution behavior noted above, in which defect energy increases as to concentration of defects (in this case oxygen vacancies) increases.

Table 5-4 Reaction energy for the creation of Ba and O vacancy pairs [text Eq. (5-9)] as calculated using 3×4×4 supercells

Dopant	Reaction energy[a] (eV)
none	5.33
La	5.98
Nd	6.47
Gd	6.69
Y	6.38
Yb	6.44

[a] for the formation of Ba and O vacancy pairs (Table 5-3).

The results of the dopant incorporation calculations are provided in Tables 5-5 and 5-6 and Figures 5-1 and 5-2. Specifically, the data in Table 5-5 and Figure 5-1 represent the results of the calculations based on reaction (5-4), whereas Table 5-6 and Figure 5-2 display the results in terms of reactions (5-6) and (5-7). The sign convention of Figure 5-2 is such that a positive value indicates preference for the Ce-site.

Table 5-5 Lattice energies of Ba-site and Ce-site doped barium cerate and the energy for the reaction[a].

Cell	3×3×5	3×4×4		
Formula	$(Ba_{42}M_2)Ce_{45}O_{135}$	$Ba_{48}(M_2Ce_{46})O_{143}$	Reaction energy[a,b]	
composition	$(Ba_{0.933}M_{0.044})CeO_3$	$Ba(M_{0.042}Ce_{0.958})O_{2.993}$	ΔE (eV)	
dopant	eV / formula unit	eV / formula unit	reaction	form. unit
La	-137.29	-134.85	-1.1973	-0.025
Nd	-137.31	-134.91	0.5404	-0.011
Gd	-137.36	-134.97	1.6858	0.035
Y	-137.39	-135.02	2.4740	0.052
Yb	-137.43	-135.06	2.7351	0.057

[a] For the reaction: $Ba_{48}(M_2Ce_{46})O_{143} \rightarrow 46/45(Ba_{42}M_2V)Ce_{45}O_{135} + (5+1/15)BaO$
[b] Total energy is as calculated directly
$\Delta E = 1.022E[(Ba_{42}M_2)CeO_3] + 5.067E[(BaO)] - E[Ba_{48}(M_2Ce_{46})O_{143}]$
Energy per formula unit is normalized with respect to the starting material, $Ba_{48}(M_2Ce_{46})O_{143}$, by division by 48.

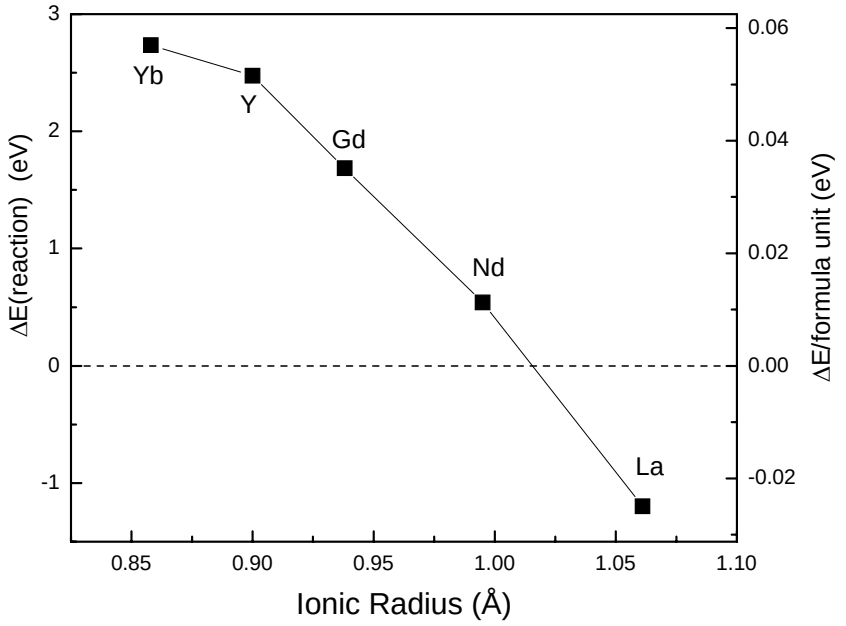

Fig. 5-1 Energy of the reaction describing BaO loss and simultaneous transfer of trivalent dopant from Ce to the Ba site (reaction (5-4) in the text)

Table 5-6 Dopant solution energies in $BaCeO_3$ as determined from of 3×4×4 supercells and compared to earlier results obtained using the mean field approximation.

Dopant	Ionic R (Å)	Ce site (eV)/per dopant atom		Ba site (eV)/per dopant atom		ΔE [E(Ba-site)-E(Ce-site)] (eV)/per dopant atom	
		supercell, rxn (11)	mean field[34]	supercell, rxn (12)	mean field[34]	supercell, rxn	mean field[34]
La	1.061	3.075	4.4	3.315	4.8	0.24	0.4
Nd	0.995	1.775	2.1	2.78	3.2	1.005	1.1
Gd	0.938	1.635	1.9	3.295	3.8	1.66	1.9
Y	0.900	1.81	1.9	3.875	4.3	2.065	2.4
Yb	0.858	1.795	2.0	4.31	4.7	2.515	2.7

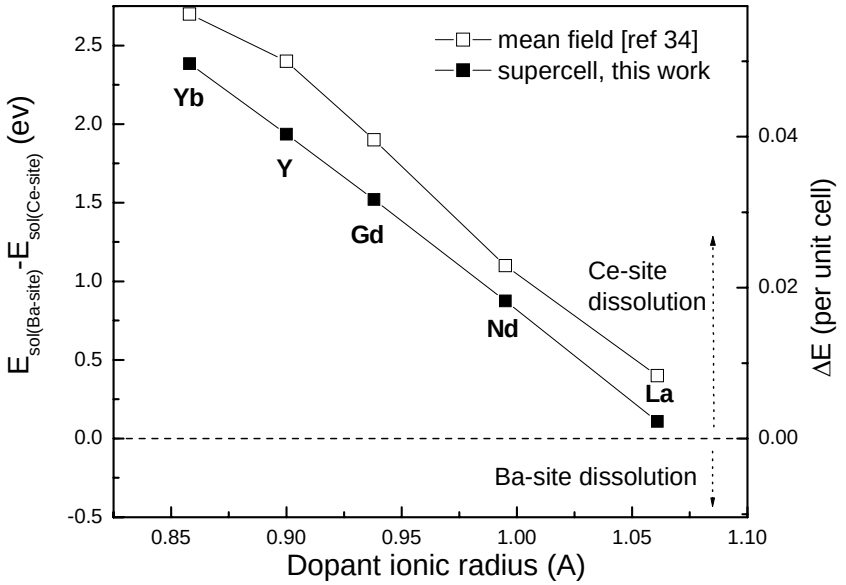

Fig. 5-2 Solution energy of selected dopants into $BaCeO_3$

Examination of Figure 5-1 reveals that reaction (5-4), barium loss accompanied by simultaneous transfer of the dopant from the Ce to the Ba-site, is energetically unfavorable for small dopants, Yb, Y and Gd, and becomes favorable as the dopant ionic radius increases to La. The ionic radius dependence of the reaction energy is quite strong, spanning 4 eV for a dopant radius change of ~ 0.2 Å. Although quantitative agreement with experimental data is not to be expected from these calculations, it is noteworthy that the crossover point from positive to negative energy occurs at approximately Nd, a dopant for which measurable Ba-site occupation was observed experimentally.

These results, along with the data in Table 5-4, further confirm that the site occupancy or dopant partitioning of trivalent dopants will be especially sensitive to the

experimental processing conditions. In particular, loss of barium at high temperatures from (B-site) doped compositions produces relatively high energy Ba-O vacancy pairs and renders Ba-site occupancy by large dopants favorable. This would reduce the concentration of oxygen vacancies which, in turn, would lead to lower proton uptake and to a decrease in proton conductivity. Indeed, although a different interpretation was proposed, Kreuer *et al.*[93] reported a dramatic decrease in the conductivity of 10% Ba-deficient barium cerate doped with La upon prolonged exposure to high temperature. In more recent work, Shima and Haile showed proton uptake in Gd-doped barium cerate to decrease monotonically as the barium deficiency increased[73]. Similar phenomena were observed in Nd-doped barium cerate, which will be discussed in Chapter 6.

Representation of the results in terms of reactions (5-6) and (5-7) in Figure 5-2, yields a similar ionic radius dependence as Figure 5-1, but with an overall apparent preference of all dopants examined, including even La, for the Ce site. As evident from Figure 5-2, the results obtained here by the supercell method are similar to those obtained earlier using the mean field approach[34], but generally show a smaller energetic difference between incorporation on the two sites. As stated above, because of the uncertainties in the lattice energies, the relative trends in the solution energies are more meaningful than their absolute values and the discrepancies between the two calculations may not be significant. However, the difference between the two approaches embodied in Figures. 5-1 and 5-2 warrants some discussion. Physically, what is represented in Figure 5-2 is the relative likelihood of initially stoichiometric barium cerate exsolving BaO or CeO_2 in order to accommodate isolated dopants on the Ba or Ce site at high dilution, respectively. Thus, the much larger lattice energy of CeO_2 over that of BaO, Table 5-1, encourages

dopant dissolution on the Ce site accompanied by BaO exsolution, even for La, which otherwise has a preference for the Ba site.

5.4 Conclusion

Static lattice simulation techniques have been used to probe the defect chemistry of the proton conductor barium cerate. The simulations suggest that, on energetic grounds, the site-occupancy of dopants is linked to barium loss. Furthermore, while Ba-O vacancy pairs remain the most favorable intrinsic defect types, the energy of such defects increases upon introduction of B-site dopants. Thus, dopant redistribution over the A and B sites is energetically favorable over vacancy pair formation and the dopant partitioning or site-occupancy of trivalent dopants will be sensitive to the precise Ba/Ce ratio, and hence to the experimental processing conditions. The reaction energy for barium loss accompanied by simultaneous transfer of the dopant from the Ce to the Ba site, is unfavorable for small dopants, Yb, Y and Gd, and becomes favorable as the dopant ionic radius increases to La. The results for Nd point to “amphoteric” behavior with significant dopant partitioning over both Ba and Ce sites. The results are consistent with the experimental compositional limits for A-site incorporation, which increases with increasing dopant ion radius.

Chapter 6 Proton Incorporation and Conductivity in Barium Cerate

6.1 Introduction

In the previous chapters, the defect chemistry of doped barium cerate has been investigated by direct and indirect experimental methods, as well as computational approaches. In this chapter, we'll discuss how the defect chemistry determines the electronic properties of doped barium cerate. In particular, results are presented for a series of Nd-doped compositions with varied Ba content, and a series of nominally stoichiometric compositions with different dopants (M= Nd, Gd, Yb).

6.2 Water Incorporation Analysis

As discussed in the previous chapters, proton incorporation in $BaCeO_3$ has been generally recognized to occur by two steps

$$2Ce_{Ce}^{x} + O_o^{x} + M_2O_3 \rightarrow 2M'_{Ce} + V^{\bullet\bullet}_o + 2CeO_2 \qquad (6\text{-}1)$$

$$H_2O\ (gas) + V^{\bullet\bullet}_o + O_o^{x} \rightarrow 2OH^{\bullet}_o \qquad (6\text{-}2)$$

where M is the trivalent dopant species. In the first step, introduction of M^{3+} ions on the Ce^{4+}-site creates oxygen vacancies within the perovskite structure. However, incorporation of the trivalent dopant on Ba-site consumes oxygen vacancies instead of creating them

$$2Ba_{Ba}^{x} + M_2O_3 + V^{\bullet\bullet}_o \rightarrow 2M^{\bullet}_{Ba} + O_o^{x} + 2BaO \qquad (6\text{-}3)$$

Therefore, dopant incorporation onto the A-site will reduce the proton uptake and proton conductivity in doped barium cerate relative to the ideally B-site doped material, an affect that results from the reduction of the concentration of oxygen vacancies. This

affect should be evident from TGA analysis of water uptake. The results of the thermal gravimetric analysis of H_2O-saturated $BaCe_{0.85}Yb_{0.15}O_3$ are presented in Fig. 6-1 along with the H_2O signal detected by mass spectroscopy. These data are representative of the three stoichiometric samples examined ($BaCe_{0.85}M_{0.15}O_{3-\delta}$, M=Nd, Gd, Yb, SSR samples).

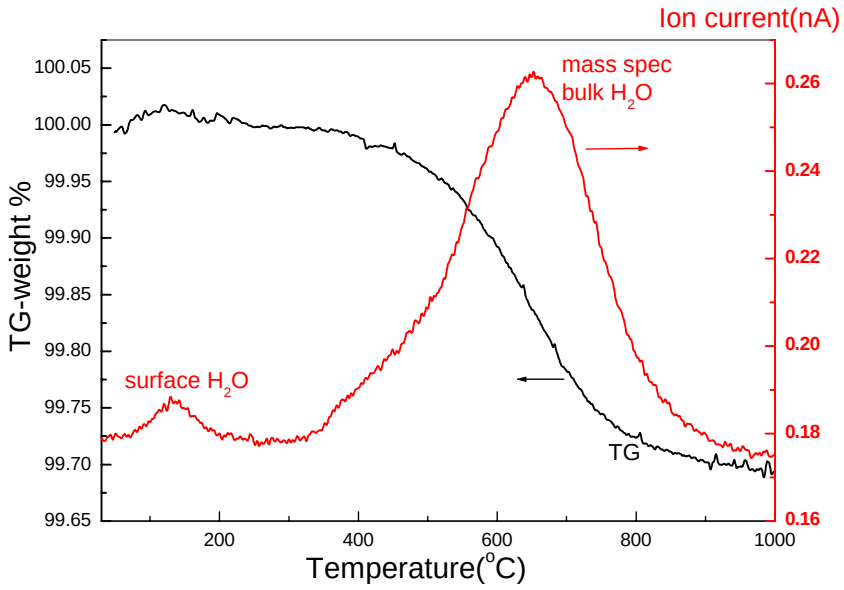

Fig. 6-1 TGA and mass spectroscopy curves for $BaCe_{0.85}Yb_{0.15}O_{3-\delta}$ obtained under dry argon at 20°C/min after saturation in an H_2O-containing atmosphere at 500°C for 20 h

Weight loss occurred in two steps, with the first one completed below 200°C and the second starting around 330°C and peaking at 650°C. Monitoring of the CO and CO_2 mass spectroscopy signals showed that these species were not responsible for any of the observed weight changes, and both weight loss events are taken to be entirely due to water. The first is assigned to the evaporation of surface adsorbed (primarily physisorbed) water, and the second to the loss of water from the bulk of the perovskite material[94,95](chemisorbed water). In principle, water uptake in M^{3+}-doped $BaCeO_3$,

according to reactions (6-1) and (6-2), is independent of the dopant species. It was observed here, however, that the bulk water content increased in the sequence Nd, Gd, Yb. The experimentally determined water contents in doped, nominally stoichiometric barium cerate, as derived from the TGA measurements of SSR samples, are listed in Table 6-1. These values are compared to: (1) what one would expect from a defect chemical model in which only B site doping occurs, Eq. (6-1), and all oxygen vacancies are filled with hydroxyl groups upon hydration, Eq. (6-2); (2) what one would expect from the perovskite composition derived from the cell volume analysis, Table 3-3 and (3) what one would expect from the experimentally measured perovskite composition by microprobe analysis from Chapter 3.

Table 6-1 H_2O content relative to various models as measured by thermal gravimetric analysis in nominally stoichiometric $BaCe_{0.85}M_{0.15}O_{3-\delta}$ (SSR samples)

Dopant (M)	*δm_0%(theo.)	δm% (TGA)	*δm_1%	*δm_2%
Nd	0.42	0.16	0.28	0.18
Gd	0.41	0.28	0.34	0.33
Yb	0.40	0.31	0.36	0.39

*δm_0%(theo.) is the expected weight loss assuming dopants are entirely incorporated onto the B-site and all oxygen vacancies are filled with hydroxyl groups;
δm_1% is the expected weight loss assuming the defect chemistry inferred from the cell volume analysis of the sintered samples and further assuming that all oxygen vacancies are filled with hydroxyl groups;
δm_2% the expected weight loss assuming the defect chemistry inferred from the electron probe chemical and analysis and further assuming that all oxygen vacancies are filled with hydroxyl groups.

As discussed in Chapter 3, a perovskite with dopant partitioning on A and B sites can be described by Eqs. (6-4) and (6-5), respectively,

$$A = \left(\frac{1-2y}{1-y}\right)Ba + \left(\frac{y}{1-y}\right)M \tag{6-4}$$

$$B = \left(\frac{0.85}{1-y}\right)Ce + \left(\frac{0.15-y}{1-y}\right)M \tag{6-5}$$

where 2y/(1-y) represents the fraction of Ba lost from the perovskite composition, and y/(1-y) the dopant occupancy on the A site. The parameter *y* is the amount of dopant on the A site before normalization for the adjusted stoichiometry of the perovskite.

The oxygen non-stoichiometry, δ, of $ABO_{3-\delta}$, is then given by

$$\delta = \frac{0.075 - y}{1 - y} \tag{6-6}$$

and this is precisely the oxygen vacancy concentration. In contrast, for doped barium cerate in which all of the trivalent dopant species reside on the B site, the vacancy concentration is simply $[V_o^{\bullet\bullet}] = 0.075$ for a 15% dopant concentration. Thus, because dopant partitioning reduces the concentration of oxygen vacancies, it can be anticipated to result in water uptake that is lower than in the ideal case, which has been proved in Table 6-1. Here, we define the ideal case as one in which, after humidification, all oxygen vacancies are occupied by hydroxyl groups, although such a limit may not be thermodynamically favorable

In all cases, Table 6-1, water uptake is significantly lower than the ideal. Furthermore, the discrepancy between the ideal and actual values increases with increasing dopant ion size, in agreement with the proposed dopant incorporation model. Most importantly, a difference in proton concentration in the hydrated samples would be expected to manifest itself as a difference in proton conductivities, which will be discussed in the following sections.

6.2 Conductivity of Non-stoichiometric $Ba_xCe_{0.85}Nd_{0.15}O_{3-\delta}$

As discussed in Chapter 1, the isotope effect is most commonly used to detect the protonic conductivity of an ionic conductor. The conductivity of $BaCe_{0.85}Nd_{0.15}O_{3-\delta}$ is shown in Fig 6-2.

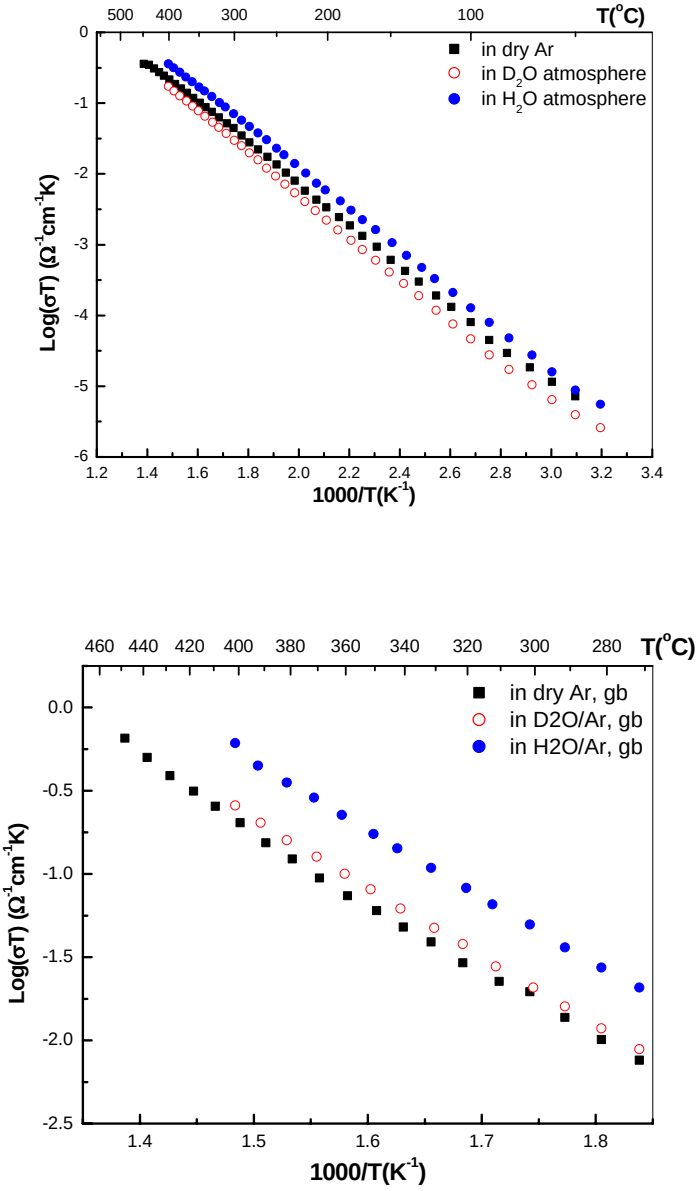

Fig. 6-2 Isotope effect of $BaCe_{0.85}Nd_{0.15}O_3$ (a) bulk conductivity (b) normalized grain boundary conductivity

It is evident that $BaCe_{0.85}Nd_{0.15}O_{3-\delta}$ exhibits protonic conductivity, in both grain interior and specific grain boundaries. The activation energy E_a and pre-exponential factor, A, are shown in Table 6-2 for $BaCe_{0.85}Nd_{0.15}O_{3-\delta}$.

Table 6-2 Activation energies and pre-exponential terms describing the grain interior and grain boundary conductivity of $BaCe_{0.85}Nd_{0.15}O_{3-\delta}$ measured in dry, H_2O and D_2O saturated Ar

Atmosphere	dry	H_2O	D_2O
E_{a_bulk} (eV)	0.57	0.57	0.58
$Log(A)_{bulk}$ ($\Omega^{-1}cm^{-1}K$)	3.581	3.839	3.547
E_{a_gb} (eV)	0.81	0.80	0.82
$Log(A)_{gb}$ ($\Omega^{-1}cm^{-1}K$)	5.357	5.727	5.518

The results indicate several points: (1) Overall, both the activation energy and the pre-exponential terms are significantly higher in grain boundaries than in grain interior. A similar trend was observed in Gd-doped barium cerate in literature.[70] It was proposed that a greater concentration of water are dissolved into the grain boundary regions upon exposure to H_2O than into the bulk due to higher defect concentration on grain boundaries, which yields higher pre-exponential term. Meanwhile, the oxygen ions and protons that form hydroxyl groups are more tightly bound together in the grain boundary regions than in the bulk, which results in higher activation energy. (2) The grain boundaries exhibit a greater responsiveness of isotope effect than the bulk, due to the contribution of higher density of structural defects on grain boundaries. (3) The ratio of pre-exponential factor for bulk, $A_H / A_D = 1.34$, is not exactly 1.41, which is yielded by the classical isotope model. However, this ratio is significantly higher than that was observed in Gd-doped $BaCeO_3$, which yielded a ratio ~1 in all cases. This result is also different from what Nowick has observed in previous study[52]. (4) The difference in activation

energy between H and D predicted by quantum mechanical theory, was observed experimentally here, with $E_D > E_H$.

Conductivity of a series of nominally Ba deficient $Ba_xCe_{0.85}Nd_{0.15}O_3$ (x = 0.85, 0.90, 0.95, 1.0) are shown in Fig 6-3.

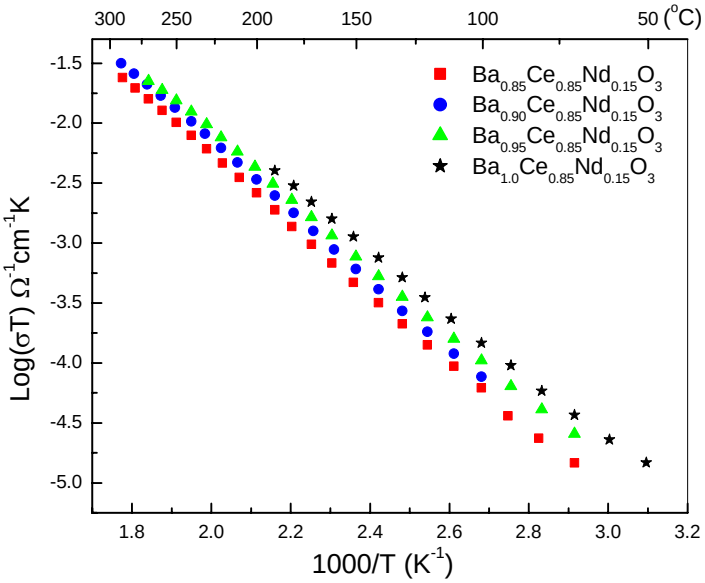

Fig. 6-3 Bulk conductivity of nominally Ba deficient $Ba_xCe_{0.85}Nd_{0.15}O_3$ (x = 0.85, 0.90, 0.95, 1.0) in water saturated N_2 atmosphere

From the results presented in Fig 6-3, it is evident that barium deficiency has a major impact on the conductivity of Nd doped $BaCeO_3$. The conductivity of the Ba = 1.0 sample is half an order magnitude greater than that of the Ba = 0.85. The same trend was observed in Gd doped $BaCeO_3$ as well[73]. The activation energy and pre-exponential terms are provided in Table 6-3.

Table 6-3 Activation energies and pre-exponential terms describing the grain interior conductivity of $Ba_xCe_{0.85}Nd_{0.15}O_{3-\delta}$ measured in flowing H_2O-saturated Ar

X	E_a (eV)	LogA ($\Omega^{-1}cm^{-1}K$)	LogA'($\Omega^{-1}cm^{-1}K$)
0.85	0.56(5)	3.40(8)	3.36(2)
0.90	0.57(5)	3.66(4)	3.47(8)
0.95	0.56(0)	3.56(9)	3.58(6)
1.0	0.54(6)	3.54(3)	3.72(9)

E_a: activation energy for proton hopping
A: pre-exponential term
A': normalized pre-exponential term obtained using a fixed average activation energy E_a'=0.56eV

Both the activation energy and the pre-exponential term vary as the Ba concentration varies, yet the differences in the conductivity arise primarily from differences in the pre-exponential term rather than the activation energy. That is, the proton conduction mechanism is essentially the same in the series. Therefore the concentration of the protons, which is determined by the amount of oxygen vacancies in the structure, influences the conductivity of different samples.

More specifically, the decrease in proton conductivity with increasing barium deficiency can be readily explained by the dopant partitioning phenomenon already confirmed for Nd by microprobe analysis. In particular if one assumes that the concentration of vacancies on the Ba site is negligible, the stoichiometries of the four samples are as given in Table 6-4

Table 6-4 Normalized stoichiometry of $Ba_xCe_{0.85}Nd_{0.15}O_{3-\delta}$ based on the A-site incorporation model

x	Normalized composition	δ
0.85	$(Ba_{0.919}Nd_{0.081})(Ce_{0.919}Nd_{0.081})O_3$	0
0.90	$(Ba_{0.947}Nd_{0.053})(Ce_{0.895}Nd_{0.105})O_{2.974}$	0.026
0.95	$(Ba_{0.974}Nd_{0.026})(Ce_{0.872}Nd_{0.128})O_{2.949}$	0.051
1.0	$BaCe_{0.85}Nd_{0.15}O_{2.925}$	0.075

The relationship between the normalized pre-exponential term and the oxygen vacancy concentration is illustrated in Fig. 6-4, which indicates an approximately linear

fit of A' vs. δ. This agrees well with the definition of the pre-exponential term, which is proportional to the density of charge carriers.

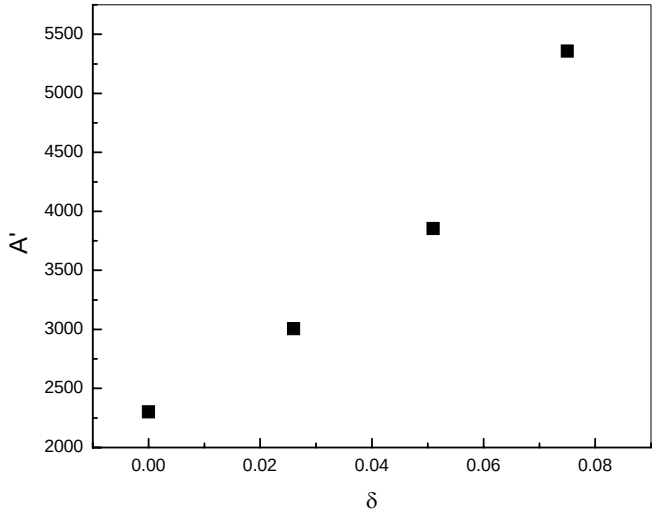

Fig. 6-4 Normalized pre-exponential term A' vs. oxygen vacancy concentration in $Ba_xCe_{0.85}Nd_{0.15}O_{3-\delta}$ (x=0.85, 0.90, 0.95, 1.0)

6.4 Proton Conductivity of $BaCe_{0.85}M_{0.15}O_{3-\delta}$ (M = Nd, Gd, Yb)

The temperature dependence of the bulk conductivity of $BaCe_{0.85}M_{0.15}O_3$ (M = Nd, Gd, Yb) in flowing water saturated Ar is shown in Fig 6-5.

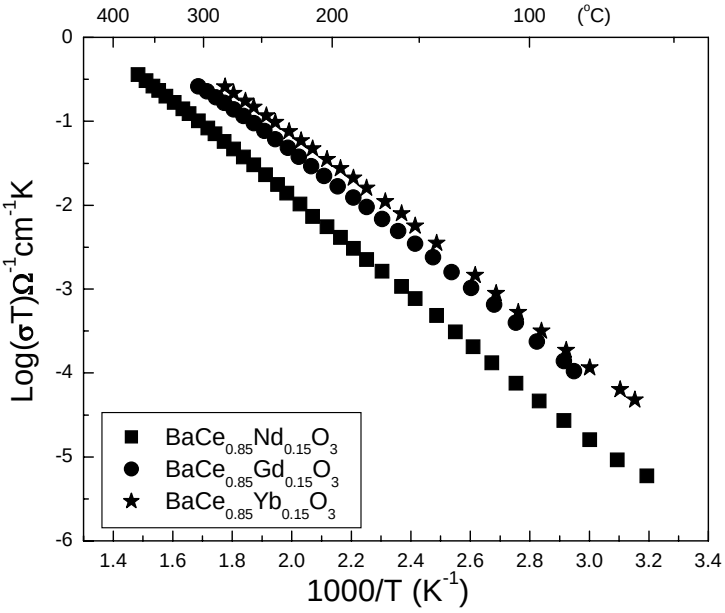

Fig. 6-5 Conductivity of $BaCe_{0.85}M_{0.15}O_{3-\delta}$ (M = Nd, Gd, Yb, SSR) under flowing, H_2O-saturated Ar

The results are summarized in Table 6-5, along with the water content in hydrated samples obtained by TGA. It is evident that the Yb-doped sample exhibits the highest water content as well as conductivity in wet Ar and the Nd-doped sample the lowest. The activation energy E_a is found to fall between 0.5 eV to 0.6 eV for all three samples, typical for proton conducting oxides [94]and suggestive of similar proton transport mechanisms.

Table 6-5 Electrical properties of nominally stoichiometric $BaCe_{0.85}M_{0.15}O_{3-\delta}$ (SSR samples, M=Nd, Gd, Yb)

Dopant (M)	Temp. range (°C)	E_a (eV)	A ($\Omega^{-1}cm^{-1}K$)	*δm% (TGA)
Nd	80-300	0.57	8469.29	0.16
Gd	80-300	0.53	12334.52	0.28
Yb	80-280	0.54	27126.95	0.31

* Water content in hydrated $BaCe_{0.85}M_{0.15}O_{3-\delta}$ obtained by TGA from Table 6-1

As we mentioned in the previous section, a difference in proton concentration in the hydrated samples would be expected to manifest itself as a difference in proton conductivity. This has been experimentally proved here. It appears then that the high conductivity Yb-doped barium cerium is at least in part due to its optimal defect chemistry, although other factors such as lattice strain upon doping and defect association are likely to also contribute to differences in conductivities for different dopant species.

6.5 Conclusion

The defect chemistry, and, in particular, the dopant site incorporation preference in the perovskite $Ba_xCe_{0.85}M_{0.15}O_3$ (M=Nd, Gd, Yb) which has been investigated in the previous chapters is confirmed in this chapter. As a consequence of the greater ability of larger cations to exist on the Ba site, the H_2O adsorption and proton conductivities of large-cation doped barium cerates are lower than those of small cation doped analogs. This conclusion set up the rules to select the appropriate dopants for $BaCeO_3$ used as electrolyte materials in SOFCs. More broadly, a material like $BaZrO_3$, in which there is a greater difference in ionic radii of the A and B-site cations, is more likely to exhibit the desired defect chemistry. Also, one should avoid high temperature processing, and, of course, avoid even slightly volatile species if possible. Meanwhile, the processing

atmosphere is important, for example, Ba-hydroxide is more volatile than Ba-oxide, which makes hydrated atmosphere unfavorable for $BaCeO_3$ processing.

Chapter 7 Zr Stabilized $BaCeO_3$: Structural Stability and Proton Conductivity

7.1 Introduction

Poor chemical stability of $BaCeO_3$ in CO_2 rich atmosphere has been a major issue that hinders its application as electrolyte in fuel cells, despite the promising properties of this material. Barium cerate reacts with CO_2 by decomposition into a mixture of $BaCO_3$ and CeO_2. This decomposition greatly limits its applicability in typical, CO_2-rich fuel cell environments. Therefore the approaches that can improve the structural stability of $BaCeO_3$ without sacrificing too much of the high proton conductivity are essential to the commercialization of barium cerate. Usually, stabilization takes place either with a physical route such as optimize grain distribution, or with a chemical route such as adding modifiers. There are limited studies on the stabilization of $BaCeO_3$ from which substitution of Zr^{4+} at Ce^{4+} sites after a formation reaction at 1500°C was proved to be effective[96]. However, the high processing temperature introduces barium non-stoichiometry problem due to the barium loss during sintering, which has been proved in the previous study. Therefore low temperature processing becomes a key point to solve this problem.

Compared with traditional solid state reaction synthesis, chemical synthesis methods such as Pechini route has been proved to be efficient in producing single-phase oxide materials with good chemical homogeneity and stoichiometry at relatively low temperatures[63,97]. An increase in chemical homogeneity is proposed to enhance chemical stability by diminishing the possibly “weak” points in a system. Hence the chemical

synthesis can decrease processing temperature, and may also improve the chemical stability by increasing homogeneity. Here the modified Pechini process described in Chapter 2 was adopted to synthesize $BaCe_{0.9-x}Zr_xGd_{0.1}O_{3-\delta}$. The chemical stability in CO_2 and the proton conductivity of $BaCe_{0.9-x}Zr_xGd_{0.1}O_{3-\delta}$ were explored in this chapter.

7.2 Experimental

$BaCe_{0.9-x}Zr_xGd_{0.1}O_3$ (x=0.0-0.4) was prepared by the modified Pechini route[63], which has been discussed in the previous chapters. The precursors were $Ba(NO_3)_2$, $Ce(NO_3)_3 \bullet 6H_2O$, $ZrO(NO_3)_2 \bullet 1.96H_2O$, and $Gd(NO_3)_3 \bullet 5.447H_2O$ (the amount of water was determined by thermogravimetric analysis). The derived char was calcined at 600°C, 800°C, 1000°C, 1200°C, and 1300°C separately for 10 h for phase formation. Following the calcination, all powders were hand milled and sieved to a particle size less than 53 microns for densification and further characterization. Green pellets (3 mm in diameter) were obtained by isostatic pressing at 150 MPa. Dense pellets were obtained after sintering in air at 1380°C, 1430°C and 1550°C for 4 h. Densities were determined by simple measurements of pellet dimensions after polishing the surfaces. To determine whether or not the processing route plays an important role in properties, another batch of samples were synthesized by traditional solid state reaction route as comparison.

The chemical stability of the samples was determined by thermal gravimetric analysis (Perkin-Elmer TGA-7) and differential thermal analysis (Perkin-Elmer DTA-7) in flowing CO_2 (25±1 ml/min) at a heating rate of 20°C/min over the temperature range of 400°C to 1440°C. The reactions with CO_2 were further deduced by XRD analysis on

the surface of the sintered samples which had been kept in a tube furnace under flowing CO_2 (25ml/min) at 600°C for 4 days.

7.3 Results and Discussion

7.3.1 Structural Characteristics of $BaCe_{0.9-x}Zr_xGd_{0.1}O_3$ (x=0-0.4)

Fig. 7-1 shows the XRD patterns of a typical sample $BaCe_{0.9}Gd_{0.1}O_{3-\delta}$ calcined at various temperatures. Below 600°C, no trace of perovskite phase was formed, whereas calcination at temperatures above 800°C led to a progressive crystallization of the perovskite phase, accompanied by the drastic decrease in the relative content of $BaCO_3$. Single-phase perovskite was obtained at 1000°C with the XRD data coincident with those of orthorhombic $BaCeO_3$[79]. Similar crystallization behaviors were found for the other compositions. In contrast, by solid state reactions, the single-phase counterparts usually crystallize at a temperature above 1300°C[73,96].

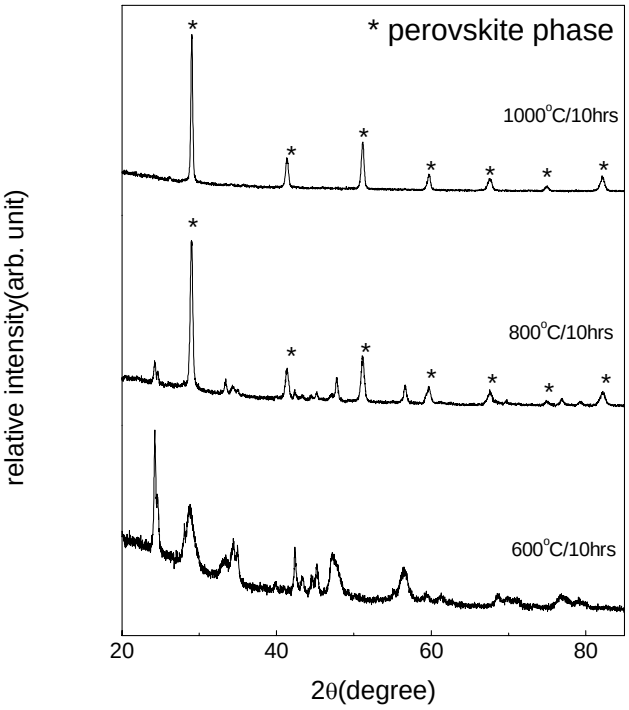

Fig. 7-1 X-ray diffraction patterns of $BaCe_{0.9}Gd_{0.1}O_3$ synthesized by modified Pechini process, calcined at different temperatures: 600°C, 800°C and 1000°C for 10 h

The XRD powder diffraction patterns of the whole $BaCe_{0.9-x}Zr_xGd_{0.1}O_3$ (x=0-0.4) series after calcinations at 1300°C are shown in Fig. 7-2.

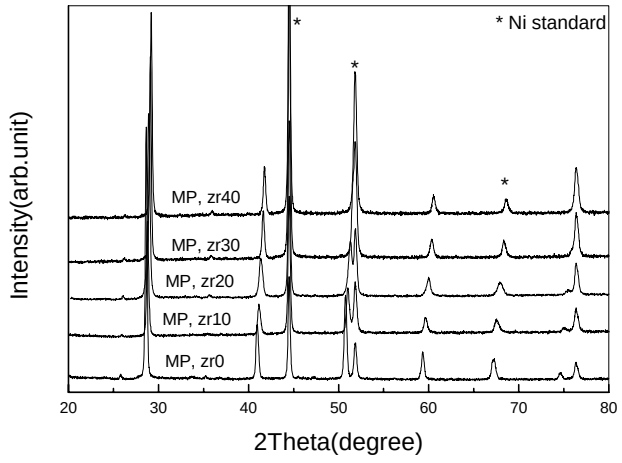

Fig. 7-2 X-ray diffraction patterns of $BaCe_{0.9-x}Zr_xGd_{0.1}O_3$ (x=0-0.4) synthesized by modified Pechini process, calcined at 1300°C

Fig. 7-3 shows the dependence of the cell volume on the substitution amount of Zr in $BaCe_{0.9-x}Zr_xGd_{0.1}O_{3-\delta}$ (x = 0.0-0.4, MP). The cell volume decreased almost linearly with the increment of Zr content, which could be rationalized in terms of the ionic radius, i.e., R^{IV} = 0.72 Å for Zr^{4+} and 0.87 Å for Ce^{4+}.[71]

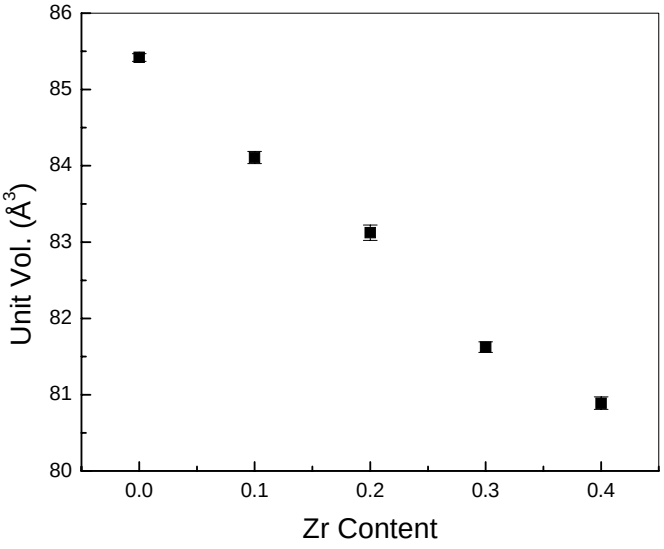

Fig. 7-3 Dependence of cell volume (per formula unit) of $BaCe_{0.9-x}Zr_xGd_{0.1}O_3$ (x=0-0.4) on Zr concentration, x

The substitution of Zr ions into the $BaCeO_3$ lattice could be further indicated by infrared spectra. Fig. 7-4(a) shows the IR spectra of the $BaCe_{0.9-x}Zr_xGd_{0.9}O_{3-\delta}$ (x=0-0.4, MP) series, with emphasis on the M-O stretching bands spreading from 400 cm^{-1} to 600 cm^{-1}.

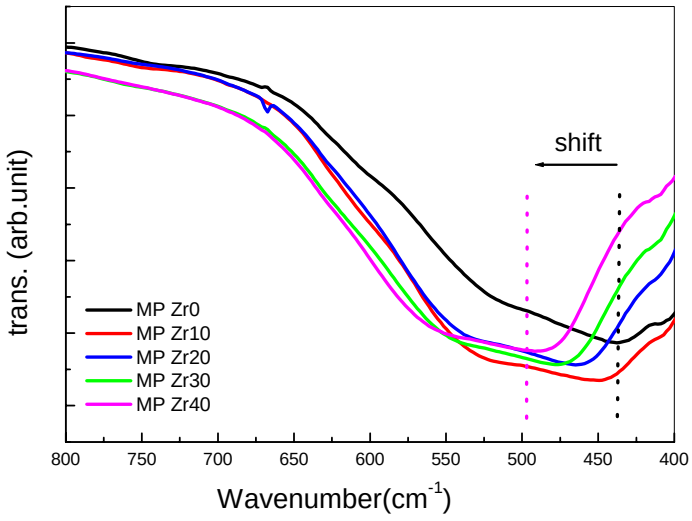

Fig. 7-4(a) FTIR spectra of $BaCe_{0.9-x}Zr_xGd_{0.1}O_3$ (x=0-0.4, MP samples)

It is evident that the absorption peak shifts to the higher energy end as the content of Zr increases, to an extent as much as 50 cm^{-1}. This tendency is expected from a harmonic oscillator model that has been adopted to simulate the two-body stretching mode.

$$\varpi_0 = \sqrt{k/\mu} \qquad (7\text{-}1)$$

where ω_0 is the characteristic frequency, k is Young's modulus and μ is the effective mass of the oscillator. The effective mass of (Ce,Zr)-O oscillator shrinks as Zr ions substitute Ce ions, due to the lighter atomic weight of Zr, which results in a higher characteristic frequency. Fig. 7-4(b) shows the relationship between the characteristic frequency and the content of Zr content, x. Due to the limited points of data, a quantitative analysis is not accessible. However, it is evident that the characteristic frequency increases with the increasing Zr content.

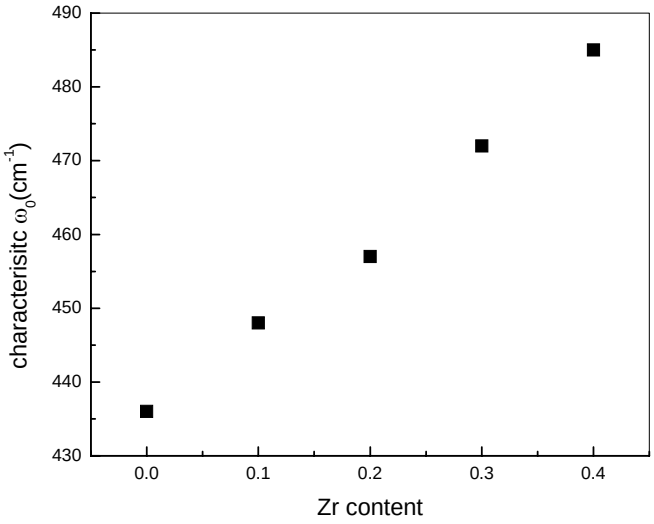

Fig. 7-4(b) FTIR characteristic frequency of M-O stretching in $BaCe_{0.9-x}Zr_xGd_{0.9}O_3$ (x=0-0.4, MP) vs. content of Zr

7.3.2 Chemical Analysis and Sintering Property of $BaCe_{0.9-}xZrxGd_{0.1}O_3$

Electron microprobe analysis indicated that the chemical homogeneity differs through different synthesis routes, as shown in Fig. 7-5 and Fig. 7-6. Here the absolute average chemical composition is not specified because only the green, porous pellets, not sintered, dense pellets were measured. The self absorbing of electrons and characteristic X-rays are not neglectable in this case.

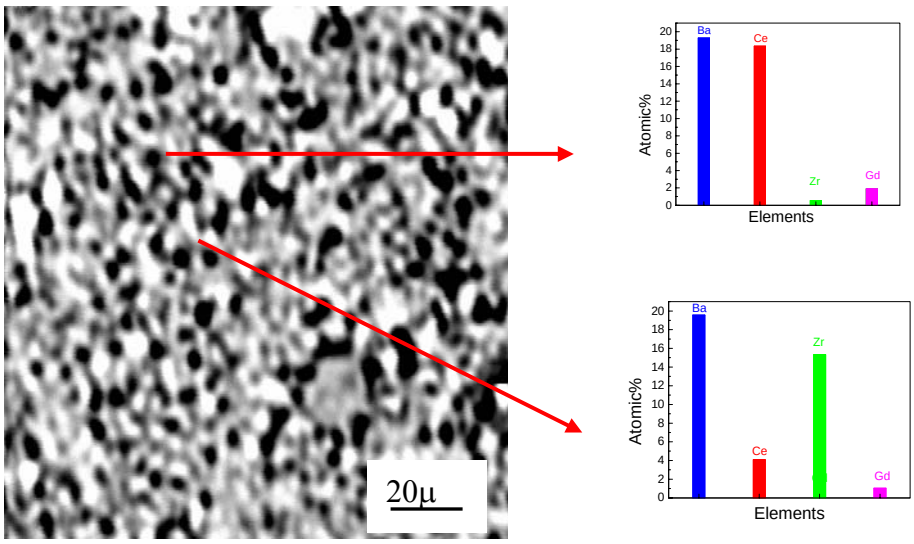

Fig. 7-5 Electron microprobe analysis on $BaCe_{0.7}Zr_{0.2}Gd_{0.1}O_3$ (SSR sample, 1300°C/16 h)

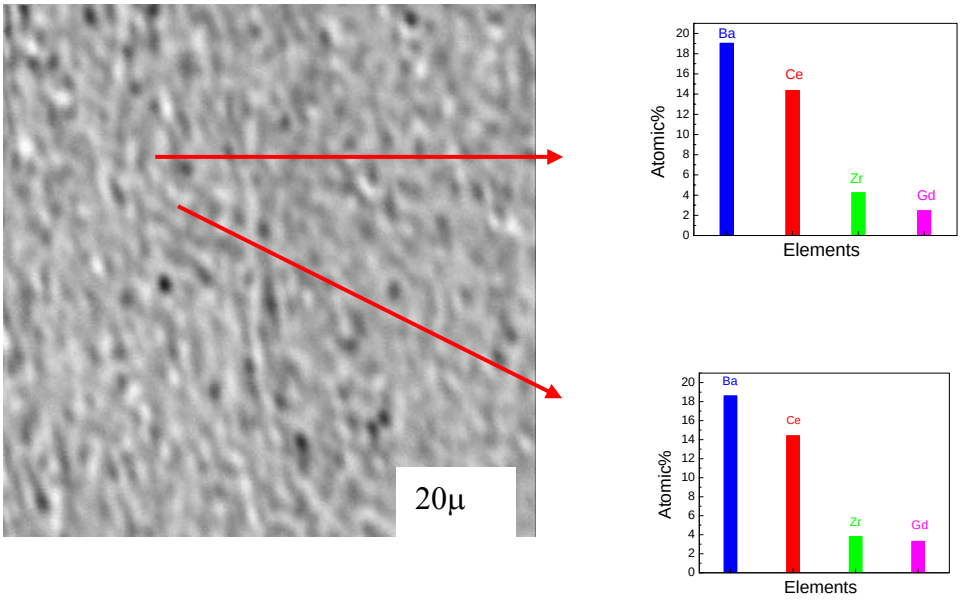

Fig. 7-6 Electron microprobe analysis on $BaCe_{0.7}Zr_{0.2}Gd_{0.1}O_3$ (MP sample, 1300°C/10 h)

Two typical samples ($BaCe_{0.7}Zr_{0.2}Gd_{0.1}O_3$, synthesized by SSR and MP route, respectively) were checked. For the SSR sample, the backscattered image shows a

mixture of white and gray spots. Focused spot analysis indicated that the white areas are more Ce rich while the gray areas are more Zr rich as the average composition is still close to stoichiometry. As for the MP sample, both the back scattered image and the spot analysis indicated a homogeneous, stoichiometric single phase. For the whole series, it is held true that the composition of the MP samples was rather uniform from point to point, whereas that of the SSR samples exhibited large variations. Hence the MP process does improve the homogeneity of the samples.

For Zr substituted $BaCeO_3$, high temperature (≥ 1550°C) sintering is necessary to get dense pellets[96]. Under this condition, BaO evaporation and thereafter the cation non-stoichiometric problems are inevitable. How to effectively lower the sintering temperature is a key factor that can solve these problems. Usually the sintering property is determined by the properties of calcined powder, such as the average particle size, size distribution, surface area, binder, etc. Chemical synthesis is capable of producing fine particles with high surface area, which helps lower the sintering temperature. Table 7-1 lists the surface area of calcined powers synthesized by different routes.

Table 7-1 surface area of $BaCe_{0.9-x}Zr_xGd_{0.1}O_3$ (x=0-0.4) synthesized by different routes

Composition	SSR (m^2/g) 1300°C/16 h	MP (m^2/g) 1000°C/10 h
x= 0	0.9506	3.1096
x= 0.1	1.2665	3.0964
x= 0.2	1.3836	4.1129
x= 0.3	0.8389	3.5438
x= 0.4	1.0847	5.3091

It is evident that the surface area of samples synthesized by modified Pechini process is several times larger than that of the solid state reaction route. Further experiments proved that samples prepared by MP process sinter well at a temperature as

low as 1380°C, which is 200°C lower than the traditional sintering temperature. The relative densities of the pellet samples sintered at 1380°C, 1430°C and 1550°C are listed in Table 7-2, where relative sample density increased with the increment of sintering temperature and reached above 96% of theoretical value.

Table 7-2 Relative density of the $BaCe_{0.9-x}Zr_xGd_{0.1}O_3$ (x=0-0.4, MP) obtained at different temperatures

	$\rho_{1380°C}$	$\rho_{1430°C}$	$\rho_{1550°C}$
x=0.0	0.97	0.97	0.97
x=0.1	0.93	0.95	0.97
x=0.2	0.92	0.95	0.96
x=0.3	0.85	0.92	0.96
x=0.4	0.84	0.92	0.96

7.3.3 Chemical Stabilities of $BaCe_{0.9-x}Zr_xd_{0.1}O_{3-\delta}$

The chemical stabilities of $BaCe_{0.9-x}Zr_xd_{0.1}O_{3-\delta}$ were measured by TGA and DTA in flowing CO_2. Fig 7-7 illustrates a typical TGA-DTA trace of calcined $BaCe_{0.9}Gd_{0.1}O_3$ in flowing CO_2.

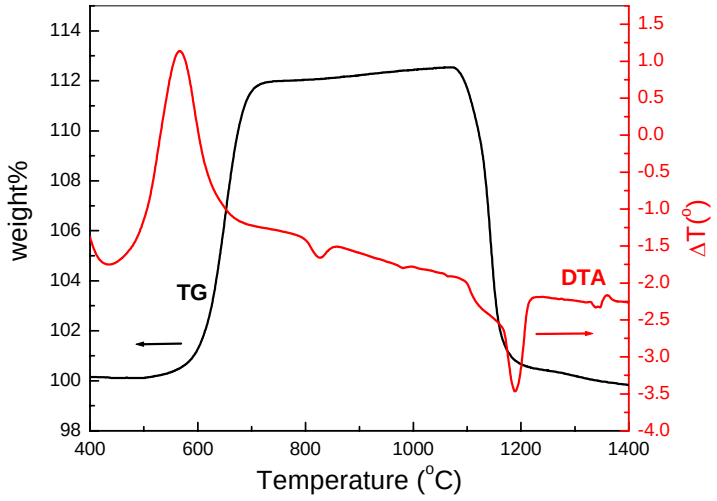

Fig. 7-7 TGA-DTA traces of $BaCe_{0.9}Gd_{0.1}O_3$ in flowing CO_2

There is a sharp weight gain starting from 500°C accompanied by an exothermic peak in DTA, indicating that reaction with CO_2 had occurred, as described by

$$BaCeO_3 + CO_2 \rightarrow BaCO_3 + CeO_2 \qquad (7\text{-}2)$$

The small endothermic peak observed at 810°C is probably due to the $BaCO_3$ phase transformation from the orthorhombic to rhombohedral[98]. The sharp weight loss around 1100°C, accompanied by an endothermic peak in DTA represents the decomposition reaction of $BaCO_3$ to BaO. On cooling (not shown), weight gain occurred and was again accompanied by an exothermic peak, due to the formation of $BaCO_3$ from BaO and CO_2.

Fig. 7-8 shows the TGA traces of the whole $BaCe_{0.9-x}Zr_xGd0.1O_{3-\delta}$ series (MP) in CO_2.

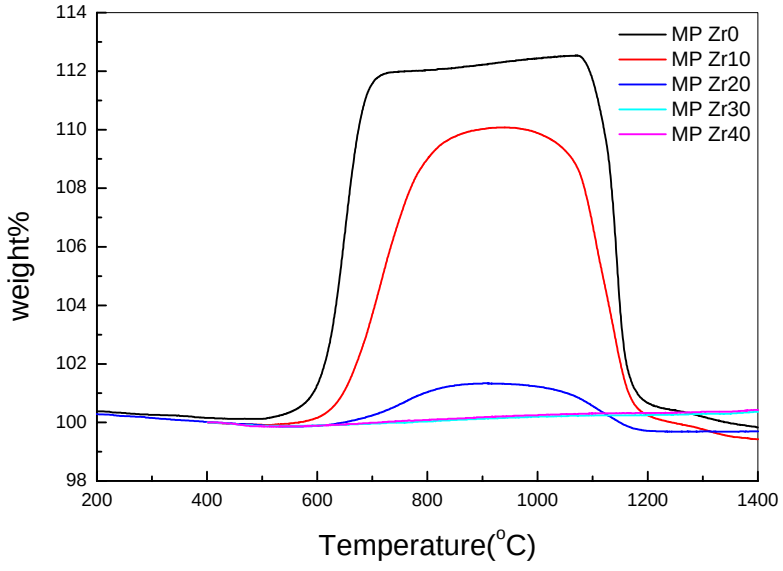

Fig. 7-8 TGA traces of $BaCe_{0.9-x}Zr_xGd_{0.1}O_3$ (x=0-0.4, MP samples) in flowing CO_2

It is evident that, with increasing Zr content, the reactivity with CO_2 decrease as reflected in the total weight gain. When the substitution content is larger than x=0.30, the samples did not show any weight gain up to 1400°C, indicating no reaction between the samples and CO_2.

To well identify the chemical stabilities of the sintered samples, sintered pellets were exposed to flowing CO_2 for 48 h followed by XRD measurement on the surface. XRD patterns of two representative samples $BaCe_{0.9-x}Zr_xGd_{0.1}O_3$ (x=0.1 and 0.4, MP) is shown in Fig. 7-9, for x=0.1, the XRD pattern showed clearly traces of $BaCO_3$, while for x=0.4, no impurities such as $BaCO_3$ or CeO_2 were observed. This is in good agreement with the TG-DTA analysis of powder samples. Due to experimental limitation, the CO_2 treatment on sintered pellets synthesized by SSR method is not available as a comparison.

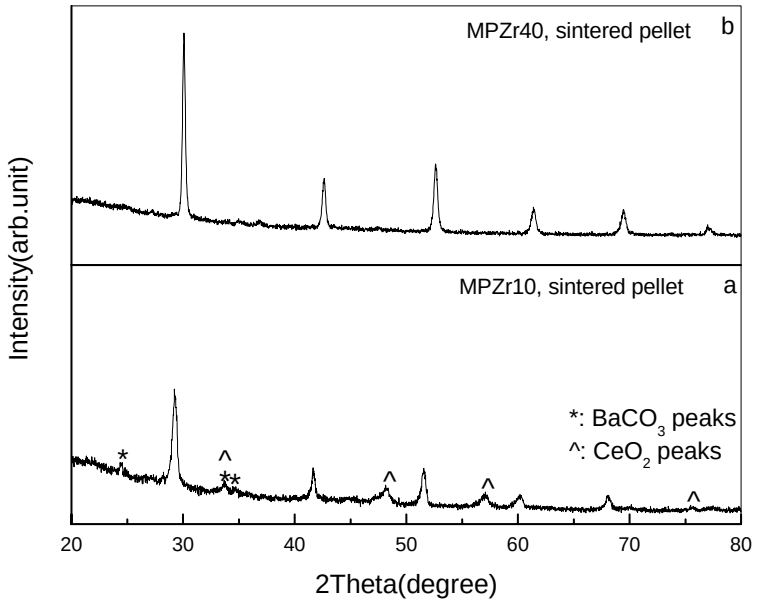

Fig. 7-9 X-ray diffraction patterns of $BaCe_{0.9-x}Zr_xGd_{0.1}O_3$ (pellets sintered at 1550°/4 h) after exposing to a flowing CO_2 atmosphere for a prolonged period, value of x as indicated

7.3.4 Conductivity of $BaCe_{1-x}Zr_xGd_{0.1}O_3$

The mechanism of AC impedance measurement was discussed in Chapter 2. The electrical properties of $BaCe_{0.9-x}Zr_xGd_{0.1}O_3$ (x=0-0.4) were listed in Table 7-3.

Table 7-3 Electrical properties measured for $BaCe_{0.9-x}Zr_xGd_{0.1}O_3$ (x=0-0.4) in H_2O saturated argon

	MP		SSR	
	E_{σ},bulk (eV)	$LogA_{bulk}$ ($\Omega^{-1}cm^{-1}K$)	E_{σ},bulk (eV)	$LogA_{bulk}$ ($\Omega^{-1}cm^{-1}K$)
x=0.0	0.49	3.72	0.51	3.72
x=0.1	0.56	3.97	0.56	3.96
x=0.2	0.56	3.92	0.57	3.77
x=0.3	0.59	3.29	--	--
x=0.4	0.63	3.82	--	--

As discussed in the previous chapters, proton conductivity in perovskite is determined by the concentration of oxygen vacancies in the perovskite structure. Oxygen vacancies are introduced by Gd dopants and in this case the concentration of Gd is fixed at 10%. Due to the iso-valence substitution of Zr^{4+} at Ce^{4+} sites, the oxygen vacancy concentration will not be disturbed by the substitution of Zr. Therefore the conductivity of the $BaCe_{0.9-x}Zr_xGd_{0.1}O_3$ series would be approximately the same if there were no other factors that contributed to the conductivity. However, the bulk conductivity of $BaCe_{0.9-x}Zr_xGd_{0.1}O_3$, shown in Fig. 7-10, illustrated clearly a dependence on the content of Zr. The normalized grain boundary conductivity shown in Fig. 7-11 illustrated a similar trend as well. In both cases, the samples synthesized by MP route yield a slightly higher conductivity than those synthesized by SSR route, except the $BaCe_{0.8}Zr_{0.1}Gd_{0.1}O_3$ samples, which yield almost the same conductivity in both cases.

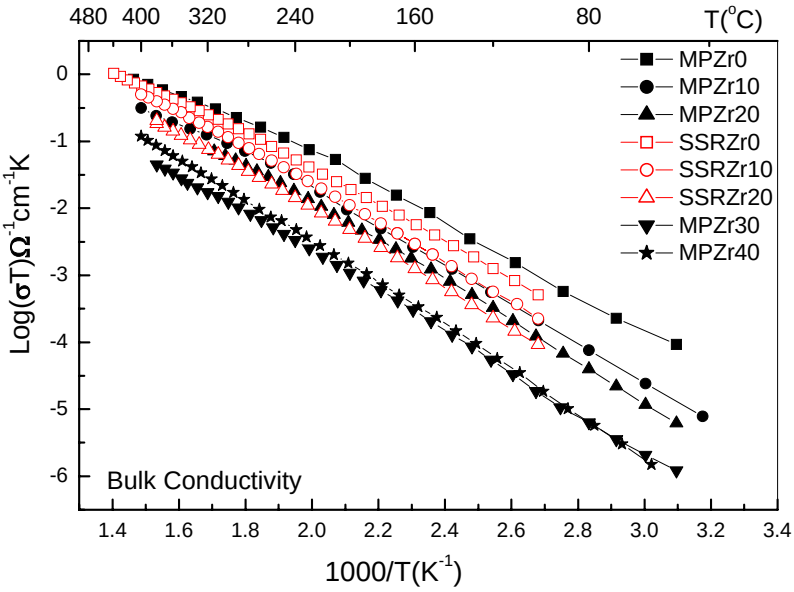

Fig. 7-10 Bulk conductivity of $BaCe_{0.9-x}Zr_xGd_{0.1}O_3$ (x=0-0.4, MP samples; x=0-0.2, SSR samples) under flowing, H_2O saturated Ar

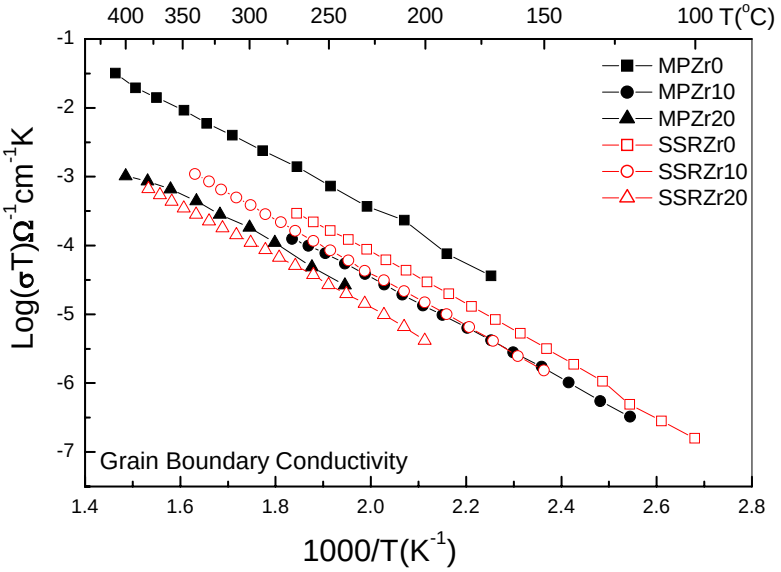

Fig. 7-11 Normalized grain boundary conductivity of $BaCe_{0.9-x}Zr_xGd_{0.1}O_3$ (x=0-0.2, MP samples; x=0-0.2, SSR samples) under flowing, H_2O saturated Ar

The reason why the conductivity is dependent on Zr content is still unclear. Here a possible explanation is proposed in terms of activation energy. One experimental observation is that the activation energy increases with increasing Zr content, Table 7-3. As we discussed in Chapter 1, in the proton hopping process, the proton transfer step is found to be rate determining. The energy barrier for proton transfer thereby significantly contributes to the activation energy[99]. XRD analysis has shown that the increasing Zr content led to the lattice shrinkage which could in turn yield higher energy barrier for proton hopping due to the introduction of structural distortion. As for the MP samples, a homogeneous phase results in an easier way for proton diffusion, which leads to lower activation energy, as we observed from experiments. The homogenous phase indicates a more uniform energy landscape, devoid of both deep and shallow traps that would likely exist in a chemically inhomogeneous material. Therefore the MP samples yield better conductivity than the SSR samples.

7.4 Conclusion

A modified Pechini process was adopted to process the single-phase perovskite $BaCe_{0.9-x}Zr_xGd_{0.1}O_3$ (x=0-0.4) of good chemical homogeneity, as a comparison to the traditional solid state reaction process. High density pellets were achieved at the temperatures 200°C lower than the traditional process. The substitution of Zr led to a decrease in cell volume and an enhanced structural stability against reactions with CO_2, especially when the Zr content was above x=0.3. $BaCe_{0.9-x}Zr_xGd_{0.1}O_3$ showed pronounced proton conduction within the bulk and along the grain boundaries. Both bulk and grain boundary conductivity decrease with the increasing Zr content, while samples

synthesized by MP process exhibit higher conductivity than those synthesized by SSR route.

Chapter 8 Future Work

8.1 Introduction

In the previous chapters the defect chemistry and proton conductivity of doped barium cerate have been investigated in detail and conclusions have been drawn. Based on these conclusions, our research expands to the investigation of new systems with both high protonic conductivity and chemical stability, in particular, doped $BaZrO_3$.

Traditionally $BaZrO_3$ was used as good capacitor material due to its high electrical resistance. As discussed in Chapter 7, Zr substitution evidently increased the chemical stability of doped $BaCeO_3$ in CO_2-rich atmosphere but decreased proton conductivity, as expected. However, recent studies indicate that doped $BaZrO_3$ itself is a promising proton conductor with even higher bulk conductivity than that of doped $BaCeO_3$[45,100]. This raises several questions that have not been answered, such as why $BaZrO_3$ was considered as a "bad" ionic conductor in most of the past studies, why Zr substituted $BaCeO_3$ exhibits worse conductivity than $BaCeO_3$ itself and what is the behavior of the $Ba(Ce,Zr)O_3$ solid solution in a completed composition range, etc. The results of some preliminary studies to address a few of these questions are presented here.

8.2 Experimental

The experimental details were described in the previous chapters therefore only a brief description is given here.

Three batches of samples were prepared: $BaZr_{0.85}Y_{0.15}O_3$, $Ba(Zr,Y)O_3$ and $BaCe_{0.85-x}Zr_xY_{0.15}O_3$ (x=0-0.85). All of the samples were synthesized by the modified

Pechini route which was described in detail in the previous chapters. The derived char was calcined at 1300°C for 10 h for phase formation.

Solid state reaction method was used in a "twice ball milling" process. $BaCO_3$, ZrO_2 and Y_2O_3 were mixed and ball milled for two days, followed by calcinations at 1300°C for 16h. The calcined powder was ball milled again using Φ3 ZYO balls for 48 h.

X-ray powder diffraction measurements were collected in reflection mode at room temperature with a Phillips X'pert diffractometer using CuKα radiation. Nickel powder (99.99%) served as an internal standard for peak position determination. The lattice parameters were refined using the Rietica Rietveld program.

Calcined $BaZr_{0.85}Y_{0.15}O_3$ powder was treated in flowing water-saturated argon atmosphere at 500°C for 20 h, followed by thermal gravimetric analysis and mass spectroscopy.

FTIR spectroscopy was carried out on a Nicolet Magna 860 FTIR spectrometer in flowing nitrogen. The transport properties of sintered pellets were measured by AC impedance spectroscopy over a frequency range from 20 Hz to 1 MHz on an HP 4284A LCR meter.

8.3 Studies of $BaZr_{0.85}Y_{0.15}O_{3-\delta}$

8.3.1 Structural Characterization

The XRD powder diffraction pattern of calcined $BaZr_{0.85}Y_{0.15}O_3$ is shown in Fig. 8-1. A single cubic phase is formed under the calcination condition. Subsequently, the lattice parameter was derived as a=4.208(2) Å, using Ni as the internal standard.

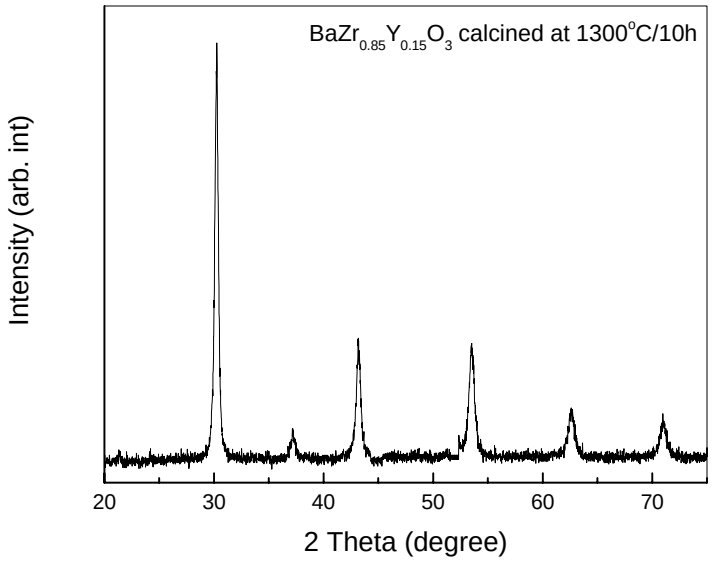

Fig. 8-1 XRD pattern of $BaZr_{0.85}Y_{0.15}O_3$ synthesized by MP, calcined at 1300°C for 10 h

8.3.2 H_2O Incorporation Analysis

The defect chemical reactions expected in Y doped $BaZrO_3$ are similar to those of the doped barium cerate, which are described as

$$2Zr_{Zr}^{x} + O_o^{x} + Y_2O_3 \rightarrow 2\ Y'_{Zr} + V^{\bullet\bullet}_o + 2ZrO_2 \qquad (8\text{-}1)$$

$$H_2O\ (gas) + V^{\bullet\bullet}_o + O_o^{x} \rightarrow 2OH_o^{\bullet} \qquad (8\text{-}2)$$

The FTIR spectroscopy of H_2O saturated $BaZr_{0.85}Y_{0.15}O_3$ powders is shown in Fig. 8-2, where the absorption bands at approximately 1500 and 3400 cm^{-1} indicate a trace of H_2O. However, it is not conclusive that H_2O is incorporated into the perovskite structure, considering the existence of surface water. Thermal gravimetric analysis conjunct with mass spectroscopy is then employed to distinguish bulk water from surface water.

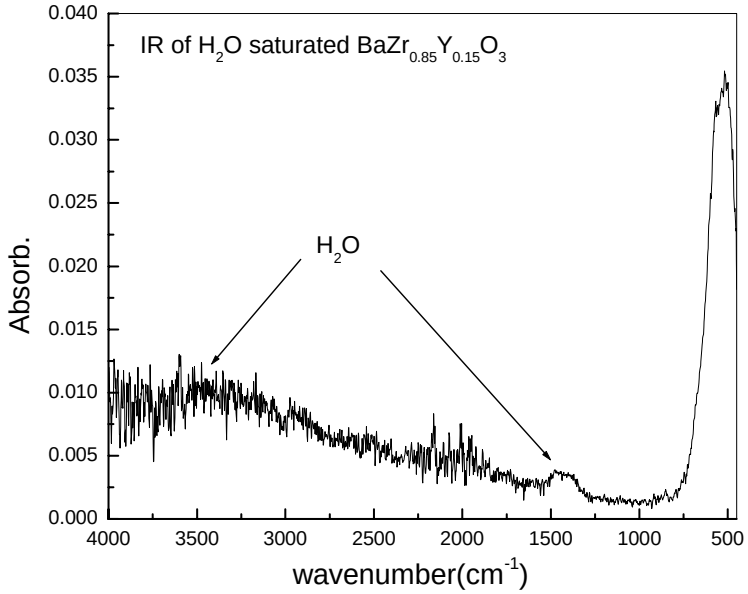

Fig. 8-2 FTIR spectroscopy of water saturated $BaZr_{0.85}Y_{0.15}O_3$

The results of the thermal analysis of H_2O-saturated $BaZr_{0.85}Y_{0.15}O_3$ are presented in Fig. 8-3 along with the H_2O signal detected by mass spectroscopy. The continuous weight loss actually took place in two steps. The first step completed below 250°C followed by the second one peaking at 520°C. Both weight loss events are due to water because the mass spectroscopy didn't show any trace of CO or CO_2. Similar to that of doped $BaCeO_3$, the first weight loss step is assigned to the evaporation of surface water and the second to the loss of water from the bulk of the perovskite structure.

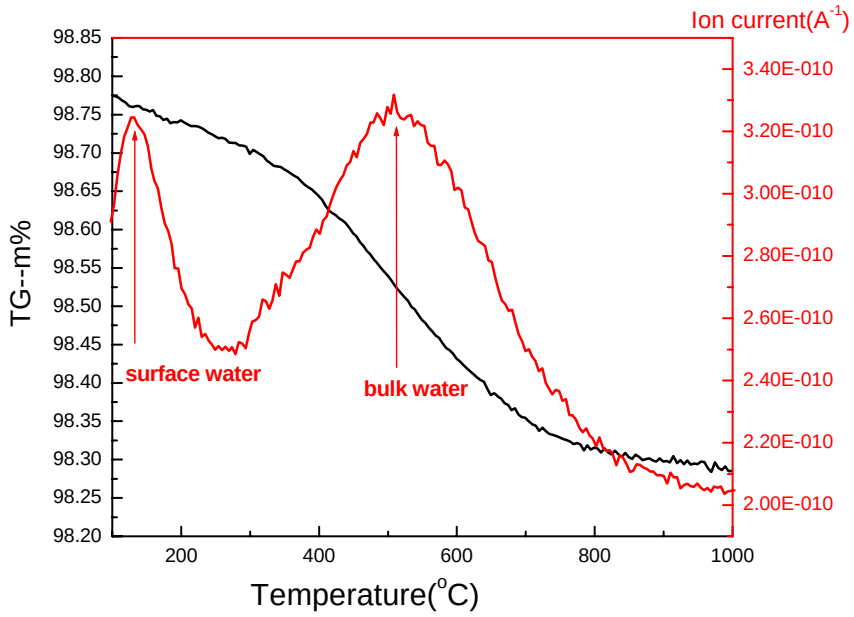

Fig. 8-3 TG-mass spectroscopy analysis of water saturated $BaZr_{0.85}Y_{0.15}O_3$

8.3.3 Sintering Property of $BaZr_{0.85}Y_{0.15}O_3$

It has been confirmed from the previous section that the oxygen vacancies in $BaZr_{0.85}Y_{0.15}O_3$ are active and capable of incorporating water into the structure. That is, protonic conductivity is expected in wet/H_2-rich atmosphere. However, the bad sintering property of barium zirconate evidently hinders the study on its transport properties.

From the literature, extremely high temperature (> 1750°C) is required to sinter $BaZrO_3$ in order to obtain dense pellets which are essential to further experiments such as fuel cell testing[100,101]. Due to experimental limitation, the maximum sintering temperature available was 1600°C. A lot of effort was carried out to lower the sintering temperature, including optimizing synthesis route, long time ball milling, atmosphere protecting sintering, prolonged sintering time, etc. To date, only long time ball milling is confirmed to be an important parameter that decreases the sintering temperature by increasing the

surface area, and probably, the surface activity of the powders. It may also introduce impurities which enhance grain boundary mobility and thereby densification.

The morphology of the cross section of sintered $BaZr_{0.85}Y_{0.15}O_3$ is shown in Fig. 8-4 with relative density of 70% and 90%, respectively. The first pellet was obtained by as-calcined powders and the second one was obtained by twice ball milled powder. BET surface area measurement was carried out on both powders. The as-calcined powder exhibits surface area 5.31 m^2/g while the double ball milled one exhibits a much high surface area 23.39 m^2/g. Both pellets were sintered at 1500°C for 10 h.

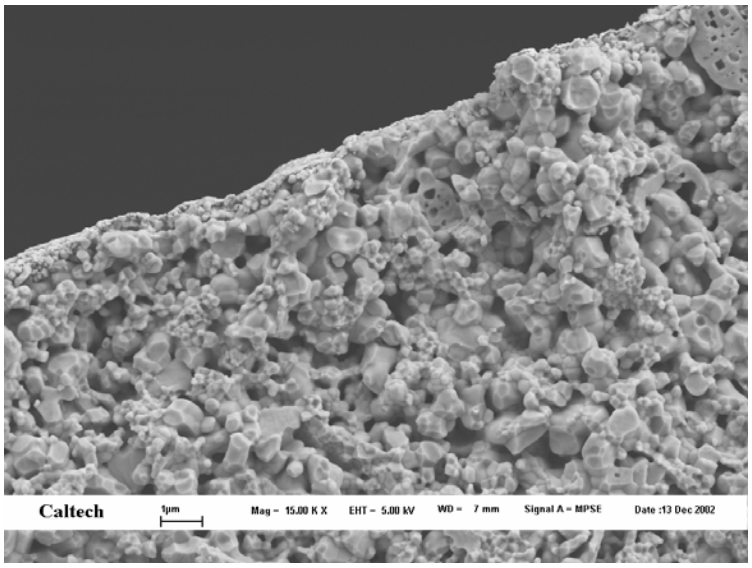

Fig. 8-4(a) SEM image of the cross section morphology of sintered $BaZr_{0.85}Y_{0.15}O_3$ with low surface area (5.31 m^2/g)

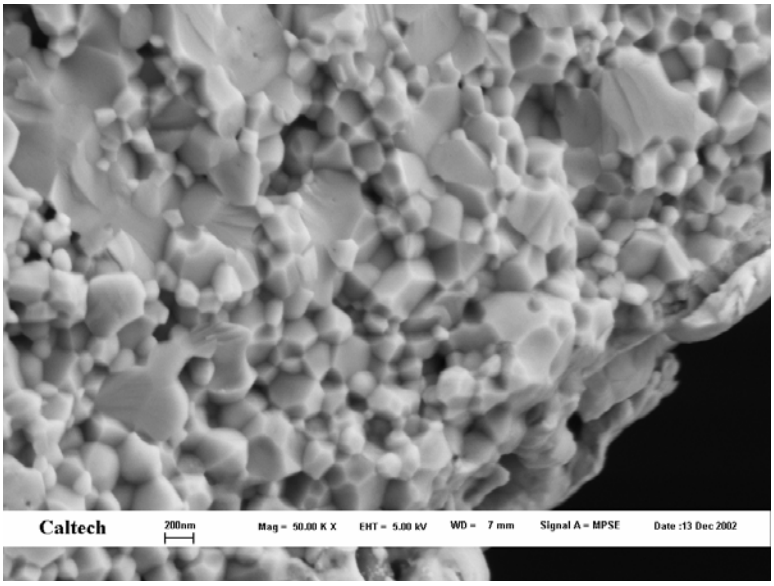

Fig 8-4(b) SEM image of the cross section morphology of sintered $BaZr_{0.85}Y_{0.15}O_3$ with high surface area (23.39 m^2/g)

Fig. 8-4(a) clearly shows that the pellet is porous and the grains are not well developed, as can be shown by the clusters of small particles attached to each other. The grain size is quite irregular, with the largest less than 1μm. Fig. 8-4(b) shows close packed regular grains which build a dense pellet. However, the average grain size is below 200 nm, with a large percent of the grains much smaller than that. Compared with dense $BaCeO_3$ pellet with an average grain size of several microns, under this condition the grains are not well developed, neither.

In order to understand the grain growth mechanism and improve the sinteribility of barium zirconate, more study has to be carried out in this area in the future.

8.3.4 Conductivity of $BaZr_{0.85}Y_{0.15}O_3$

The conductivity of $BaZr_{0.85}Y_{0.15}O_3$ was carried out on both the porous and the dense pellets. However, the impedance data of the dense pellet were scattered and unable to be analyzed. Due to the shortage of sintered dense samples, only the porous pellet was studied in detail.

The impedance data are plotted in Fig. 8-5 for various temperatures.

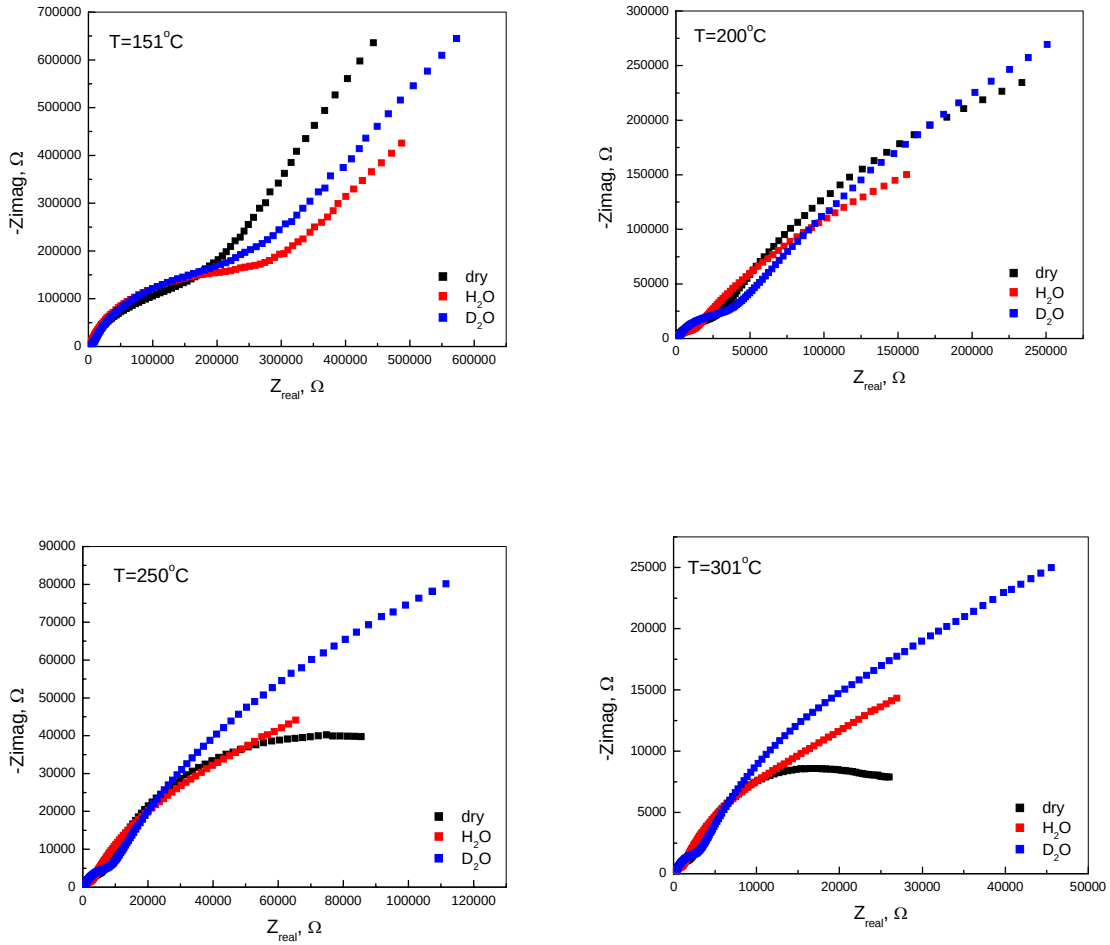

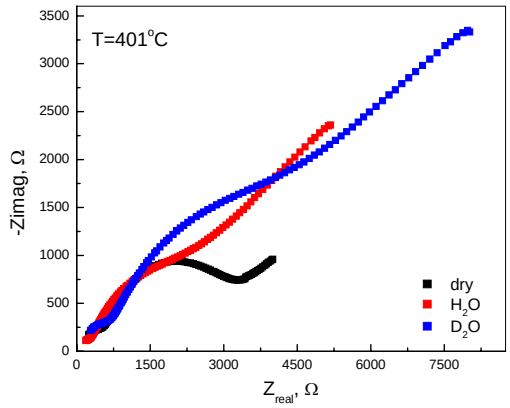

Fig. 8-5 Impedance data of $BaZr_{0.85}Y_{0.15}O_3$ at selected temperatures (T= 151, 200, 250, 301, 401°C)

It is evident that the bulk resistance decreases sharply as temperature increases. Above 250°C the bulk characteristic frequency is so high that only the grain boundary circle is visible. The bulk and total conductivity are shown in Fig. 8-6.

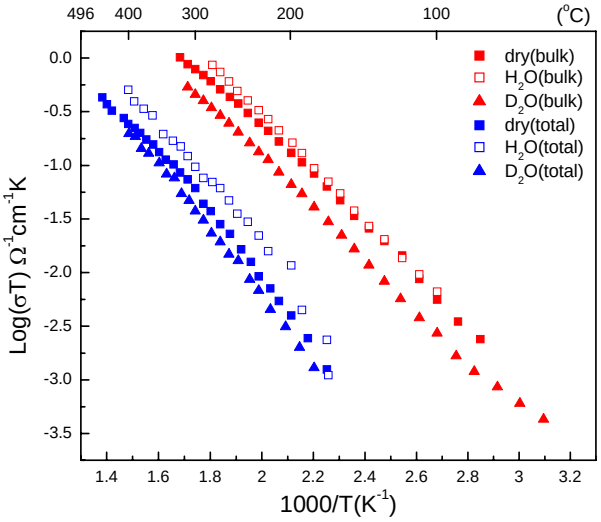

Fig. 8-6 Bulk and total conductivity of $BaZr_{0.85}Y_{0.15}O_3$ in various atmosphere (dry N_2, water saturated N_2 and D_2O saturated N_2)

Compared with doped barium cerate, the bulk conductivity of barium zirconate is 0.5 to 1 magnitude higher while the total conductivity is much lower. One of the important factors that contribute to this difference is the grain boundary resistance, which is show in Fig. 8-7.

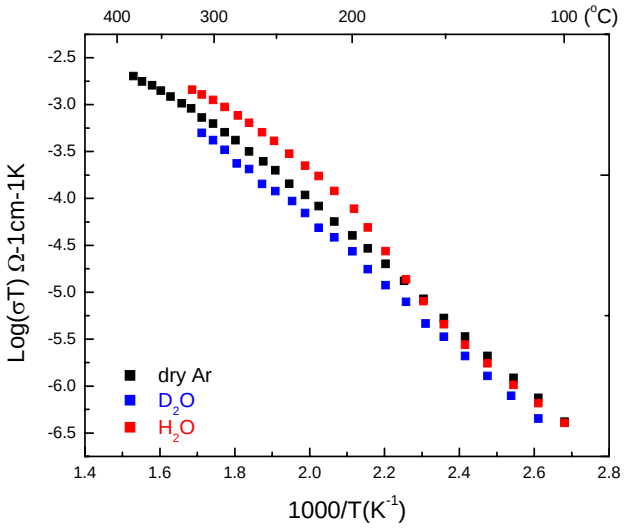

Fig. 8-7 Specific grain boundary conductivity of $BaZr_{0.85}Y_{0.15}O_3$ in various atmosphere (dray N_2, water saturated N_2 and D_2O saturated N_2)

The specific grain boundary resistance of barium zirconate is extremely high, compared with barium cerate, which lowers the total conductivity and to a big extent hinders the application of this material as an ionic conductor.

However, these results are not conclusive yet due to the limit numbers of samples that have been measured. The grain boundary behavior and the kinetics of grain growth are complicated and need further investigation in detail.

8.4 Studies of $Ba(Zr_{1-x},Y_x)O_3$ System

As the study on $BaZr_{0.85}Y_{0.15}O_3$ has yielded promising results, the dopant optimization has been raised as a critical question. In order to obtain the best conductivity, there are two parameters that have to be optimized: the dopant species and the dopant concentration. As for the species, Y is the element right next to Zr on the periodic table, which ensures a small lattice distortion. The ionic radius of Y^{3+} is much smaller than that of Ba^{2+} which minimizes the site partition problem. Based on the above consideration Y is an appropriate dopant at this stage.

The selection of dopant concentration is more complicated in this case. Experiments and atomistic calculation on barium cerate indicate specific dopant concentration at which point the protonic conductivity peaks. From the defect chemistry point of view, there is no defect in a perfect undoped material and no protonic conductivity will be observed. When a crystal is doped, oxygen vacancies are introduced and thereafter the protonic conductivity. The amount of active oxygen vacancies is proportional to the concentration of the dopant. However, at a certain point when the dopant concentration is so high that the defect-dopant association and defect clustering are taking over the hopping protons, the conductivity starts to drop. Thus there is an optimized dopant concentration which is related to the dopant species, the parent crystal structure, the temperature range and the working atmosphere. In this case those parameters are fixed in order to derive the optimized dopant concentration in a timely manner.

8.4.1 Structural Characterization

The XRD powder diffraction pattern of calcined $BaZr_{1-x}Y_xO_3$ (x=0.2-0.5) is shown in Fig. 8-8. A single perovskite phase is formed under the calcination condition for every composition that has been measured.

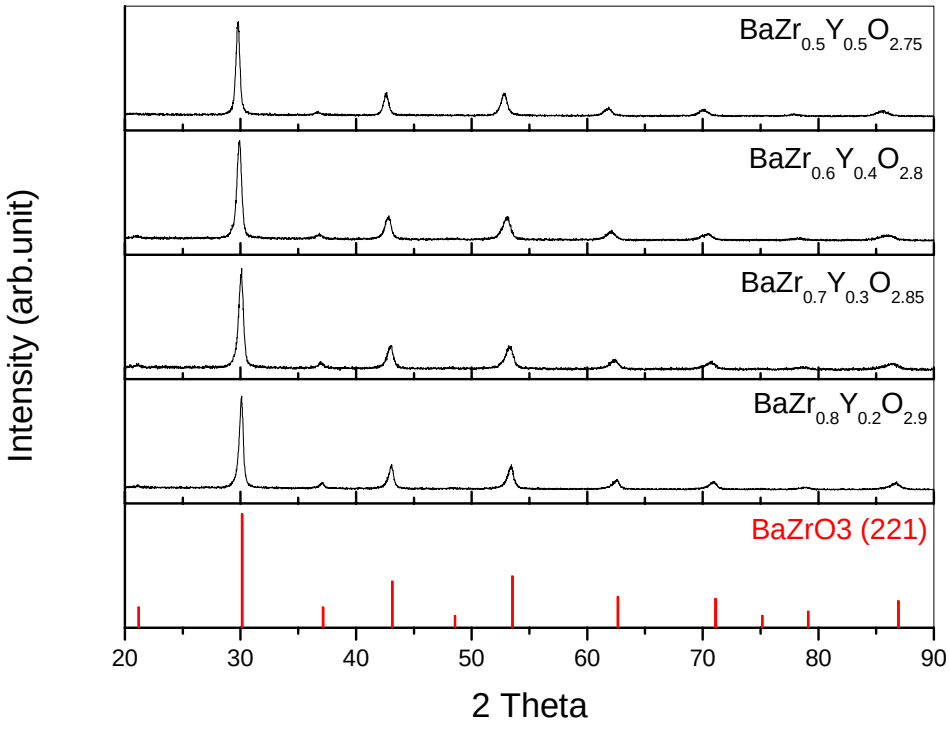

Fig. 8-8 XRD pattern of calcined $BaZr_{1-x}Y_xO_3$ (x=0.2-0.5)

From this figure, as the dopant concentration gets higher, the peaks shifted to lower 2θ, which is expected due to the ion size difference between Y^{3+}(0.892 Å) and Zr^{4+}(0.72 Å). The lattice parameter refinement is shown in Fig. 8-9 which an almost linear increase of the lattice parameter as a function of the yttrium concentration x.

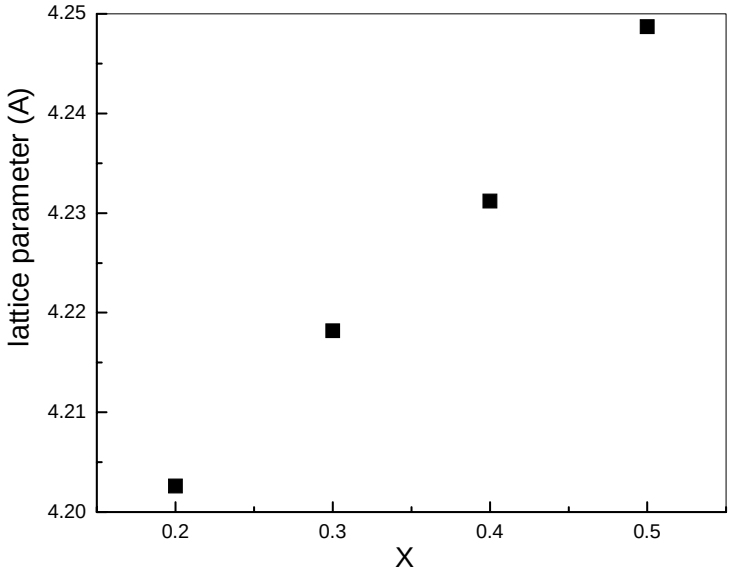

Fig. 8-9 Lattice parameter refinement of calcined $BaZr_{1-x}Y_xO_3$ (x=0.2-0.5)

8.4.2 Preliminary Results on $BaZr_{0.5}Y_{0.5}O_{2.25}$

To date only $BaZr_{0.5}Y_{0.5}O_{2.25}$ was investigated on the sintering and transport properties. The cross section morphology of a sintered $BaZr_{0.5}Y_{0.5}O_{2.25}$ pellet was checked by SEM, which is shown in Fig. 8-10. The image illustrates a porous matrix made of fine and homogeneous grains, similar to that of the $BaZr_{0.85}Y_{0.15}O_3$ sintered at 1500°C. Thus the sintering property remains an unsolved problem in the $Ba(Zr_{1-x},Y_x)O_3$ series, despite the possibility that yttrium helps the sintering process. Different models have been proposed to explain the sintering difficulty in barium zirconate, including the impurities "pinning" the grain boundary from further growth, the extremely low grain boundary energy, the kinetic study, etc[97,102]. Of all the explanations, the grain boundary behavior is the first priority we have to understand in the future work.

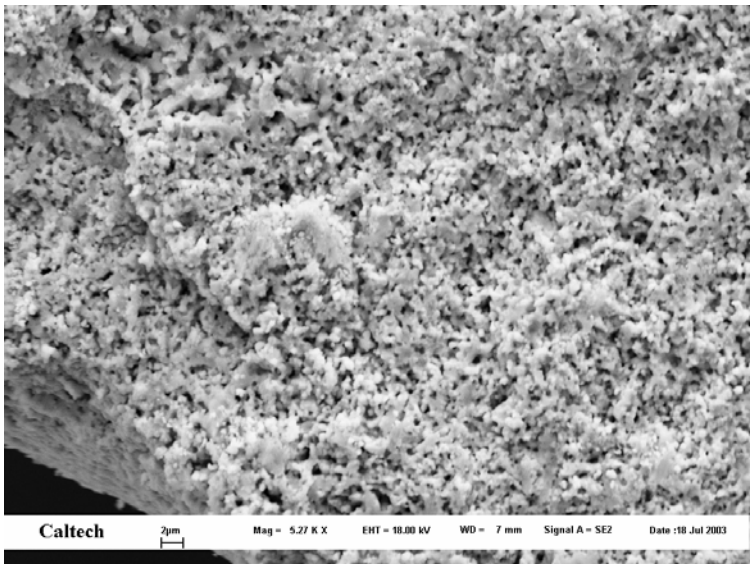

Fig. 8-10 SEM image of the cross section morphology of sintered $BaZr_{0.5}Y_{0.5}O_{2.25}$

The bulk transport property of $BaZr_{0.5}Y_{0.5}O_{2.25}$ measured with a porous pellet is shown in Fig 8-11. From this figure the isotope effect is evident thus the protonic conductivity is dominating under the operating environment. However, at the same temperature the bulk conductivity of $BaZr_{0.5}Y_{0.5}O_{2.25}$ is more than one magnitude lower than that of $BaZr_{0.85}Y_{0.15}O_3$. As we proposed earlier, the defects association could be a big contribution to the bad conductivity. Nevertheless, further investigation is needed to better understand this problem.

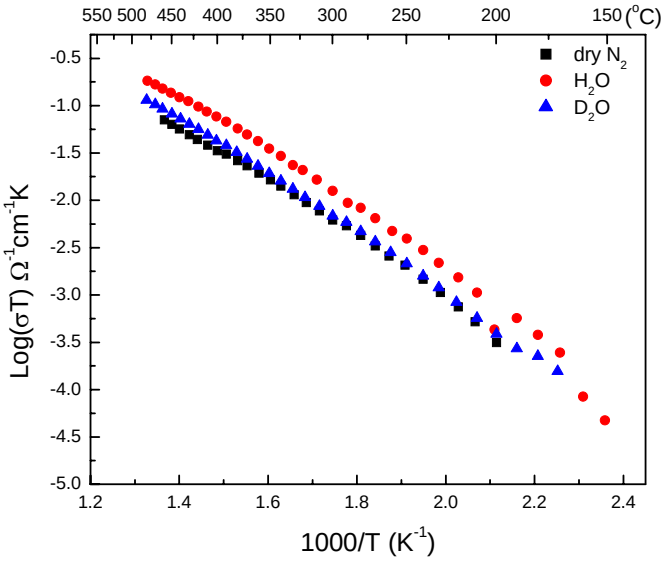

Fig. 8-11 Bulk conductivity of $BaZr_{0.5}Y_{0.5}O_{2.25}$ under various atmospheres

8.5 Preliminary Results on $Ba(Ce,Zr)Y_{0.15}O_3$ Solid Solution

In Chapter 7 we discussed Zr substituted $BaCeO_3$ and how Zr stabilized barium cerate in CO_2 rich atmosphere. In that chapter we have the conclusion that the protonic conductivity of the $Ba(Ce_{0.9-x},Zr_x)Gd_{0.1}O_3$ (x=0-0.4) solid solution decreases monotonically as x increases. However, recent study on $BaZr_{0.85}Y_{0.15}O_3$ illustrated high bulk conductivity which comes up with a question: If both doped $BaCeO_3$ and $BaZrO_3$ exhibit high protonic conductivity, why their solid solution shows poorer conductivity than either of the end material? Since we've only checked the samples close to the Ce end, is it possible that the conductivity behavior would be different close to the Zr end? Is there a critical composition at which point the opposite trends joint? To answer these questions, $BaCe_{0.85-x}Zr_xY_{0.15}O_3$ (x= 0.1-0.7) was synthesized and studied.

The XRD powder diffraction pattern of calcined $BaCe_{0.85-x}Zr_xY_{0.15}O_3$ (x= 0.1-0.7) is shown in Fig 8-12. For every composition in this series, a single perovskite phase is formed under the calcination condition.

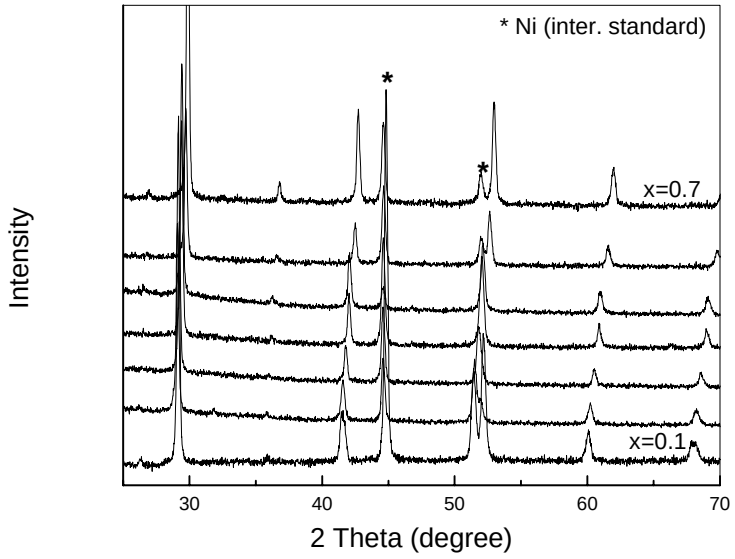

Fig. 8-12 XRD pattern of calcined $BaCe_{0.85-x}Zr_xY_{0.15}O_3$ (x= 0.1-0.7)

Using Ni powder as internal standard, the refined lattice parameter is shown in Fig 8-13. The cell volume shrinks almost linearly as the concentration of Zr increases, which is expected based on the ionic radius of Zr^{4+} and Ce^{4+}.

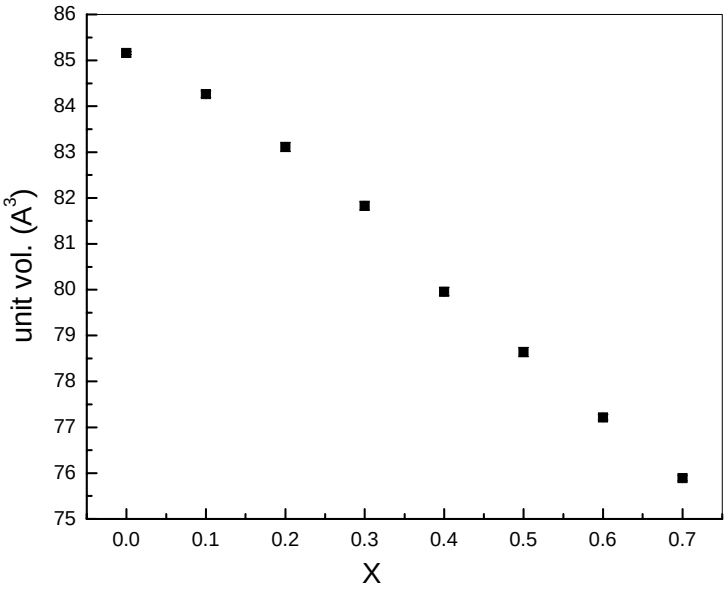

Fig. 8-13 Cell volume of $BaCe_{0.85-x}Zr_xY_{0.15}O_3$ (x= 0.1-0.7)

The structural characterization indicates that a complete series of $BaCe_{0.85-x}Zr_xY_{0.15}O_3$ is obtainable. The next stage will be the chemical stability measurement and most important, the transport property investigation.

Bibliography

1. Navrotsky, A.; Weidner, D. J. *Geophysical Monograph 45* **1987**
2. Byer, R. *IEEE Journal of Selected Topics in Quantum Electronics* **2000**, 6(6), 911
3. Fainman, Y; Ma, J; Lee, S. *Materials Science Reports* **1993**, 9(2-3), 53
4. Moret, M.; Devillers, M.; Worhoff, K.; Larsen, P. *J. Appl. Phys.* **2002**, 92(1), 468
5. Jona, F.; Shirane, G.; Pepinsky, R. *Physical Review* **1955**, 97(6), 1584
6. Weber, M.; Bass, M.; Demars, G. *J. Appl. Phys.* **1971**, 42(1), 301
7. Rao, K.; Yoon, K. *J. Mater. Sci*. **2003**, 38(3), 391
8. Dimos, D.; Mueller, C. *Annual Review of Materials Science* **1998**, 28, 397
9. Shaw, T.; Trolier-McKinstry, S.; McIntyre, P. *Annual Review of Materials Science* **2000**, 30, 263
10. DeTeresa, J.; Ibarra, M.; Algarabel, P.; Ritter, C.; Marquina, C.; Blasco, J.; Garcia, J.; delMoral, A.; Arnold, Z. *Nature* **1997**, 386(6622), 256
11. Gilleo, M. *J. Chem. Phys.* **1956**, 24(6), 1239
12. Kishi, H.; Mizuno, Y.; Chazono, H. *Japanese Journal of Applied Physics Part 1-Regular Papers Short Notes and Review Papers* **2003**, 42(1), 1
13. Huang, K.; Feng, M.; Goodenough, J.; Milliken, C. *J. Electrochem. Soc.* **1997**, 144(10), 3620
14. Iwahara, H.; Uchida, H.; Ono, K.; Ogaki, K. *J. Electrochem. Soc.* **1988**, 135(2), 529
15. Iwahara, H.; Uchida, H.; Kondo, J. *Journal of Applied Electrochemistry* **1983**, 13(3), 365
16. Mizusaki, J.; Tabuchi, J.; Matsuura, T.; Yamauchi, S.; Fueki, K. *J. Electrochem. Soc.* **1989**, 136(7), 2082
17. Fukui, T.; Ohara, S.; Kawatsu, S. *J. Power Sources* **1998**, 71(1-2), 164
18. Mukundan, R.; Davies, P.; Worrell, W. *J. Electrochem. Soc.* **2001**, 148(1), A82-A86
19. Ihringer, J.; Maichle, J.; Prandl, W.; Hewat, A.; Wroblewski, T. *Zeitschrift Fur Physik B-Condensed Matter* **1991**, 82(2), 171
20. Lin, L. *Materials Science and Engineering R-Reports* **2000**, 29(6), 153

21. Sampathkumar, T.; Srinivasan, S.; Nagarajan, T.; Balachandran, U. *Applied Superconductivity* **1994**, 2(1), 29

22. Spinicci, R.; Tofanari, A.; Delmastro, A.; Mazza, D.; Ronchetti, S. *Mater. Chem. Phys.* **2002**, 76(1), 20

23. Forni, L.; Rossetti, I. *Applied Catalysis B-Environmental* **2002**, 38(1), 29

24. Knight, K. S. *Solid State Ionics* **1994**, 74, 109

25. Hoffmann, A. *Zeitschrift fuer Physikalische Chemie, Abteilung B: Chemie der Elementarprozesse, Aufbau der Materie* **1935**, 28(65-77)

26. Jacobson, A. J.; Tofield, B. C.; Fender, B. E. F. *Acta Crystallographica B* **1972**, 28, 956

27. Iwahara, H.; Uchida, H.; Morimoto, K. *J. Electrochem. Soc.* **1990**, 137(2), 462

28. Islam M.S. *J. Mater. Chem.* **2000**, 10, 1027

29. Colomban, P. *Proton Conductors: Solids, membranes and gels-materials and devices*, Cambridge University press **1992**

30. Baikov, Yu. M.; Shalkova, E. K. *J. Solid State Chem.* **1992**, 97, 224

31. Bonanos, N. *Solid State Ionics* **1992**, 53-56, 967

32. Norby, T. *Solid State Ionics* **1999**, 125, 1

33. Kroger, F.; Vink, V. *Solid State Physics* **1956**, 3, 307

34. Glockner, R.; Islam, M. S.; Norby, T. *Solid State Ionics* **1999**, 122(1-4), 145

35. Makovec, D.; Samardžija, Z.; Kolar, D. *J. Am. Ceram. Soc.* **1997**, 80(12), 3145

36. Haile, S. M.; Staneff, G.; Ryu, K. H. *J. Mat. Sci.* **2001**, 36, 1149

37. Davies, R. A.; Islam, M. S.; Gale, J. D. *Solid State Ionics* **1999**, 126, 323

38. Islam, M. S. *Solid State Ionics* **2002**, 154(75-85 Part B Sp. Iss.), 75

39. Islam, M. S.; Cherry, M. *Solid State Ionics* **1997**, 97(1-4), 33

40. Kreuer, K. D.; MÜnch, W.; Ise, M.; He, T.; Fuchs, A.; Traub, U.; Maier, J. *Ber.Bunsenges. Phys.Chem.* **1997**, 101(9), 1344

41. Karmonik, C. ; Udovic, T. J.; Paul, R. L.; Rush, J. J.; Lind, K.; Hempelmann, R. *Solid State Ionics* **1998**, 109, 207

42. Goodenough, J. B. *Solid State Microbatteries, chapter Designing a Solid Electrolytes III. Proton Conduction and Composites*, Plenum Press, New York, **1990**

43. Kreuer, K.; Dippel, Th.; Hainovsky, N.; Maier, J. *Ber. Bunsenges. Phys. Chem.* **1992**, 96(11), 1736

44. Kreuer, K. D. *Chem. Mater.* **1996**, 8, 610

45. Kreuer, K. D. *Annu.Rev.Mater.Res.* **2003**, 33, 333

46. Chisholm, C. *Superprotonic Phase Transitions in Solid Acids:Parameters affecting the presence and stability of superprotonic transitions in the MHnXO4 family of compounds (X=S, Se, P, As; M=Li, Na, K, NH4, Rb, Cs)* **2003**

47. Kreuer, K. D. *Solid State Ionics* **2000**, 136-137, 149

48. Davies, R. A.; Islam, M. S.; Chadwick, A. V.; Rush, G. E. *Solid State Ionics* **2000**, 130, 115

49. Scherban, T.; Baikov, Yu. M.; Shalkova, E. K. *Solid State Ionics* **1993**, 66, 159

50. Nowick, A.; Vaysleyb, A. *Solid State Ionics* **1997**, 97(1-4), 17

51. Liu, J.; Nowick, A. S. *Solid State Ionics* **1992**, 50(1-2), 131

52. Nowick, A. S.; Du, Y. *Solid State Ionics* **1995**, 77, 137

53. Hibino, T.; Mizutani, K.; Iwahara, H. *J. Electrochem. Soc.* **1993**, 140(9), 2588

54. Liang, K.; Nowick, A. S. *Solid State Ionics* **1993**, 61(1-3), 77

55. Kek, D.; Bonanos, N. *Solid State Ionics* **1999**, 125(1-4), 345

56. N.Q. Minh and T. Takahashi *Science and Technology of Ceramic Fuel Cells*, Elsevier, **1995**

57. Arestova, N. V.; Gorelov, V. P. *Russian Journal of Electrochemistry* **1994**, 30(8), 988

58. Frade, J. *Solid State Ionics* **1995**, 78, 87

59. Bonanos, N.; Elllis, B.; Knight, K. S.; Mahnood, M. N. *Solid State Ionics* **1989**, 35, 179

60. Gopalan, S.; Virkar, A. *J. Electrochem. Soc.* **1993**, 140(4), 1060

61. Scholten, M. J.; Schoonman, J.; Miltenburg, J. C. v.; Oonk, H. A. J. *Solid State*

Ionics **1993**, 61, 83

62. Navrotsky, A. *Perovskite: A structure of great interest to geophysics and materials science* **1987**, Geophysical Monograph 45, 67

63. Agarwal, V.; Liu, M. *J. Mater. Sci.* **1997**, 32, 619

64. IUCR Powder Diffraction 22 **1997**, 21

65. Pouchou, J.-L.; Pichoir, F. *Electro Probe Quantitation*, edited by K. Heinrich and D. Newbut (Plenum Press, 1991), 31-75

66. Armstrong, J. T. *Microbeam Anal.* **1995**, 4, 177

67. Brunauer, S. *Physical Adsorption* **1945**

68. Macdonald, R. J. *Impedance Spectroscopy* **1987**

69. Buchanan, R. C. *Ceramic Materials for Electronics* **1986**

70. Haile, S. M.; West, D. L.; Campbell, J. *J.Mater.Res.* **1998**, 13(6), 1576

71. Shannon, R. D. *Acta Crysta.* **1976**, A32 (5), 751

72. Mogensen, M. ; Lybye, D.; Bonanos, N.; Hendriksen, P. V.; Poulsen, F. W. *Electrochemical Society Proceedings* **2002**, 2001-28, 15

73. Shima, D.; Haile, S. M. *Solid State Ionics* **1997**, 97, 443

74. Teo, B. K. *EXAFS: Basic Principles and Data Analysis* **1986**

75. Webb, S. M. *http://www-ssrl.slac.stanford.edu/~swebb/sixpack.htm*

76. Rehr, J. J.; Zabinsky, S. I.; Albers *Phys. Rev. Lett* **1992**, 69(23), 3397

77. Valant, M.; Suvorov, D. *Eur. J. Solid State Inorg. Chem.* **1996**, 33(11), 1161

78. Nakayama, M. ; Ikuta, H.; Uchimoto, Y.; Wakihara, M.; Terada, Y.; Miyanaga, T.; Watanabe, I. *Journal of Physical Chemistry B* **2003**, 107(39), 10715

79. Knight, K. S.; Bonanos, N. *J. Mater. Chem* **1994**, 4, 899

80. Charrier-Cougoulic, I.; Pagnier, T.; Lucazeau, G. *J. Solid State Chem.* **1999**, 142, 220

81. Buscaglia, M. T.; Buscaglia, V.; Viviani, M. *J. Am. Ceram. Soc.* **2001**, 84(2), 376

82. Gale, J. *J. Chem. Soc., Faraday Trans.* **1997**, 93(4), 629

83. Catlow, C., in: A.K. Cheetham, P.Day (Eds.), *Solid State Chemistry: Techniques*, Clarendon Press, Oxford, **1987**, Chapter 7

84. Khan, M.; Islam, M.; Bates, D. *Journal of Physical Chemistry B* **1998**, 102(17), 3099

85. Lewis, G.; Catlow, C. *Journal of Physics C-Solid State Physics* **1985**, 18(6), 1149

86. Balducci, G.; Islam, M.; Kapar, J.; Fornasiero, P.; Graziani, M. *Chem. Mater.* **2000**, 12(3), 677

87. Freeman, C.; Catlow, C. *J. Solid State Chem.* **1990**, 85(1), 65

88. Dick, B.; Overhauser, A. *Physical Review* **1958**, 112(1), 90

89. Catlow, C.; Ackermann, L.; Bell, R.; Cora, F.; Gay, D.; Nygren, M.; Pereira, J.; Sastre, G.; Slater, B.; Sinclair, P. *Faraday Discussions* **1997**, 106, 1

90. Yamada, A.; Chiang, Y. M. *J. Am. Ceram. Soc.* **1995**, 78(4), 909

91. Brzozowski, E.; Castro, M. S. *Journal of Materials Science: Materials in Electronics* **2003**, 14, 471

92. Kreuer, K. D.; SchÖnherr, E.; Maier, J. *Solid State Ionics* **1994**, 70-71(1-4), 278

93. Kreuer, K. D.; SchÖnherr, E.; Maier, J. *Proc. 14th RisŘ Intern. Sypm. on Materials Science* **1993**

94. Stevenson, D. A.; Jiang, N.; Buchanan, R. M.; Henn, F. E. G. *Solid State Ionics* **1993**, 62, 279

95. Kruth Angela; Irvine, J. T. S. *Solid State Ionics* **2003**, 162-163, 83

96. Ryu, K. H.; Haile, S. M. *Solid State Ionics* **1999**, 125, 355

97. Maschio, S.; Bachiorrini, A.; Lucchini, E.; Bruckner, S. *J. Eur. Ceram. Soc.* **2004**, 24(8), 2241

98. CRC handbook of Chemistry and Physics, 84th edition, by CRC Press, **2004**

99. Munch, W.; Kreuer, K.; Seifert, G.; Maier, J. *Solid State Ionics* **2000 Sp. Iss. SI Nov**, 136, 183

100. Bohn, H. G.; Schober, T. *J. Am. Ceram. Soc.* **2000**, 83(4), 768

101. Katahira, K.; Kohchi, Y.; Shimura, T.; Iwahara, H. *Solid State Ionics* **2000**, 138, 91

102. Ubaldini, A.; Buscaglia, V.; Uliana, C.; Costa, G.; Ferretti, M. *J. Am. Ceram. Soc.* **2003**, 86(1), 19